

FABRICATION, PERFORMANCE AND THERMOELECTRIC  
PROPERTIES OF MONOLITHIC  $\beta$ -Zn<sub>4</sub>Sb<sub>3</sub>/ZnO  
THERMOELECTRIC GENERATOR MODULES



A Thesis Submitted in Partial Fulfillment of the Requirements for the  
Degree of Doctor of Philosophy in Physics  
Suranaree University of Technology  
Academic Year 2023

การประดิษฐ์ สภาพการทำงาน และคุณสมบัติทางเทอร์โมอิเล็กทริกของ  
อุปกรณ์โมดูลกำเนิดไฟฟ้า โมโนลิทิก ปีต้า-ซิงก์แอนติโมนายด์/ซิงค์ออกไซด์



นายทัชกฤษ แจ่มปรีชา

วิทยานิพนธ์นี้เป็นส่วนหนึ่งของการศึกษาตามหลักสูตรปริญญาวิทยาศาสตรดุษฎีบัณฑิต  
สาขาวิชาฟิสิกส์  
มหาวิทยาลัยเทคโนโลยีสุรนารี  
ปีการศึกษา 2566

FABRICATION, PERFORMANCE AND THERMOELECTRIC PROPERTIES OF  
MONOLITHIC  $\beta$ -Zn<sub>4</sub>Sb<sub>3</sub>/ZnO THERMOELECTRIC GENERATOR MODULES

Suranaree University of Technology has approved this thesis submitted in  
partial fulfillment of the requirements for the Degree of Doctor of Philosophy.

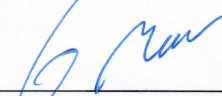
Thesis Examining Committee



(Prof. Dr. Supree Pinitsoontorn)  
Chairperson



(Prof. Dr. Santi Maensiri)  
Member (Thesis Advisor)



(Assoc. Prof. Dr. Worawat Meevasana)  
Member



(Dr. Narong Chanlek)  
Member



(Asst. Prof. Dr. Wittawat Saenrang)  
Member



(Assoc. Prof. Dr. Yupaporn Ruksakulpiwat)  
Vice Rector for Academic Affairs  
and Quality Assurance



(Prof. Dr. Santi Maensiri)  
Dean of Institute of Science

ทักษกฤษ แจ่มปรีชา : การประดิษฐ์ สภาพการทำงาน และคุณสมบัติทางเทอร์โมอิเล็กทริกของ  
อุปกรณ์โมดูลกำเนิดไฟฟ้า โมโนลิทิก ปีต้า-ซิงก์แอนติโมนายด์/ซิงค์ออกไซด์ (FABRICATION,  
PERFORMANCE AND THERMOELECTRIC PROPERTIES OF MONOLITHIC  $\beta$ -  
Zn<sub>4</sub>Sb<sub>3</sub>/ZnO THERMOELECTRIC GENERATOR MODULES)

อาจารย์ที่ปรึกษา : ศาสตราจารย์ ดร.สันติ แม้นศิริ, 117 หน้า.

คำสำคัญ: โทเมอร์อิเล็กทริก, โมโนลิทิก, โมดูลกำเนิดไฟฟ้าเทอร์โมอิเล็กทริก, ปีต้า-ซิงก์แอนติโมนายด์

งานวิจัยนี้ได้ศึกษาคุณสมบัติทางเทอร์โมอิเล็กทริกของวัสดุเทอร์โมอิเล็กทริกปีต้า-ซิงก์แอนติโมนายด์ ( $\beta$ -Zn<sub>4</sub>Sb<sub>3</sub>) รวมถึงได้ทำการสร้างโมดูลกำเนิดไฟฟ้าแบบโมโนลิทิก ปีต้า-ซิงก์แอนติโมนายด์ ( $\beta$ -Zn<sub>4</sub>Sb<sub>3</sub>)/ซิงค์ออกไซด์ (ZnO) จากวัสดุ  $\beta$ -Zn<sub>4</sub>Sb<sub>3</sub> ที่สังเคราะห์ขึ้นมาเอง อีกทั้งได้ทำการทดสอบสภาพการทำงานของโมดูลที่วัดโดยใช้เครื่องวัด IV และพาวเวอร์เอาต์พุตที่พัฒนาขึ้นมาเอง ซึ่งกระบวนการสังเคราะห์ การวิเคราะห์ การประดิษฐ์และการประเมินผลการทำงานของวัสดุปีต้า-ซิงก์แอนติโมนายด์และโมดูลกำเนิดไฟฟ้าเทอร์โมอิเล็กทริก ได้อธิบายโดยลำดับดังนี้

วัสดุ  $\beta$ -Zn<sub>4</sub>Sb<sub>3</sub> ถูกสังเคราะห์ขึ้นโดยการสังเคราะห์แบบปฏิกิริยาในสถานะของแข็ง “จากวัสดุตั้งต้นคือผงสังกะสีและผงพลวงในอัตราส่วน 4:3 และเพิ่มผงสังกะสีส่วนเกินเพื่อชดเชยในส่วนที่จะพร่องไปเนื่องจากการระเหิดของผงสังกะสีอันเกิดขึ้นโดยธรรมชาติที่สถานะอุณหภูมิสูง ค่าการชดเชยที่ดีที่สุดคือ 12 at.% Zn หลังจากนั้นสารผสมตั้งต้นจะถูกนำไปเผาที่ 400 °C เป็นเวลา 3 ชั่วโมง ภายใต้ระบบแก๊สอาร์กอนเพื่อป้องกันไม่ให้เกิดโครงสร้างทางออกไซด์ในสารสังเคราะห์ หลังจากทำการสังเคราะห์เสร็จสิ้นแล้ว วัสดุ  $\beta$ -Zn<sub>4</sub>Sb<sub>3</sub> ที่สังเคราะห์ขึ้นถูกนำไปตรวจสอบโครงสร้างทางผลึกโดยเทคนิคการเลี้ยวเบนของรังสีเอกซ์ จากการตรวจสอบพบว่าวัสดุ  $\beta$ -Zn<sub>4</sub>Sb<sub>3</sub> ที่สังเคราะห์ขึ้นนั้นมีรูปแบบการเลี้ยวเบนของรังสีเอกซ์สอดคล้องกับฐานข้อมูลและโมเดลผลึก  $\beta$ -Zn<sub>4</sub>Sb<sub>3</sub> ของ Mozharivskiy และมีความบริสุทธิ์ค่อนข้างสูงแต่ก็มีโครงสร้างของ ZnSb, Zn, Sb เจือปนอยู่เล็กน้อย เพราะอุณหภูมิที่ใช้ในการเผามีการกวัดแกว่งเนื่องจากการพาความร้อนของแก๊สอาร์กอนที่ไหลผ่านระบบตลอดเวลา นอกจากนี้ วัสดุ  $\beta$ -Zn<sub>4</sub>Sb<sub>3</sub> ที่สังเคราะห์ขึ้นยังถูกนำไปตรวจสอบด้วยเทคนิคการดูดกลืนรังสีเอกซ์ที่ขอบเขตการดูดกลืนระดับพลังงานใกล้เคียงกับระดับพลังงานไอออไนเซชันของอิเล็กตรอนในชั้นพลังงานระดับลึกในโครงสร้างของอะตอมธาตุหลัก ผลการตรวจสอบพบว่าวัสดุ  $\beta$ -Zn<sub>4</sub>Sb<sub>3</sub> ที่สังเคราะห์ขึ้นมานั้นมีการดูดกลืนพลังงานของไอออไนเซชันของอิเล็กตรอนในชั้นพลังงานระดับ (Normalized XANES) K ของอะตอมธาตุ Zn มีการดูดกลืนพลังงานหลักที่ 9,659 eV โดยยืนยันการดูดกลืนพลังงานหลักด้วยกราฟผลต่างการดูดกลืนค่าพลังงาน (Derivation of normalized XANES) ส่วนผล Normalized XANES ของชั้นพลังงานระดับ L3 L2 และ L1 ของอะตอมธาตุ Sb มีการดูดกลืนพลังงานหลักที่ 4,132 eV, 4,380 eV และ 4,698 eV ตามลำดับโดยยืนยันการดูดกลืนพลังงานหลักด้วยกราฟผลต่างการดูดกลืนค่าพลังงาน จากผลการตรวจสอบการดูดกลืนค่าพลังงานจากรังสีเอกซ์สามารถวิเคราะห์ได้ว่าสถานะไอออไนเซชันของอิเล็กตรอนในชั้นพลังงานระดับลึกของระดับพลังงาน K ของอะตอมธาตุ Zn และ ระดับพลังงาน L1, L2 และ L3 ของอะตอมธาตุ Sb มีสถานะ

ออกซิเดชันเป็น  $Zn^0$  และ  $Sb^0$  หลังการตรวจสอบโครงสร้างทางผลึกวัสดุ  $\beta-Zn_4Sb_3$  ที่สังเคราะห์ขึ้น ได้ถูกนำไปอัดเม็ดที่ความดัน 700 MPa และเผาหลอมผลึกที่อุณหภูมิ 500 °C เป็นเวลา 6 ชั่วโมง ภายใต้ระบบแก๊สอาร์กอนเพื่อป้องกันไม่ให้เกิดโครงสร้างทางออกไซด์ที่ผิวของเม็ดเซรามิก หลังจากทำการเผาหลอมผลึกเสร็จแล้วเม็ดเซรามิก  $\beta-Zn_4Sb_3$  ได้ถูกนำไปทดสอบวัดคุณสมบัติทางเทอร์โมอิเล็กทริก ผลการทดสอบพบว่าเม็ดเซรามิก  $\beta-Zn_4Sb_3$  มีค่าสัมประสิทธิ์ซีเบคที่สูงอย่างเด่นชัดที่ 255  $\mu V/^\circ C$  ที่อุณหภูมิทดสอบ 320 °C อีกทั้งยังมีค่าความต้านทานไฟฟ้าที่ต่ำและเสถียรที่  $8 \times 10^{-5} \Omega \cdot m$  ระหว่างช่วงอุณหภูมิทดสอบ 250–400 °C ค่าสัมประสิทธิ์ซีเบคที่สูงและค่าความต้านทานไฟฟ้าที่ต่ำ บ่งบอกถึงการเป็นวัสดุเทอร์โมอิเล็กทริกที่ดีตามนิยามของสัมประสิทธิ์พิทเทอร์ออฟเมอร์ริท (ZT) ในขณะที่ค่าเพาเวอร์แฟคเตอร์ที่บ่งบอกถึงสภาพการทำงานที่ดีตามกำลังไฟฟ้ามีค่าสูงที่  $\sim 0.56 \text{ mW/m}^\circ C^2$  ที่อุณหภูมิทดสอบ 220–240 °C จากผลการทดสอบคุณสมบัติทางเทอร์โมอิเล็กทริกของเม็ดเซรามิก  $\beta-Zn_4Sb_3$  นั้นมีคุณสมบัติที่ดีพอสำหรับการประดิษฐ์อุปกรณ์โมดูลกำเนิดไฟฟ้าเทอร์โมอิเล็กทริก

อุปกรณ์โมดูลกำเนิดไฟฟ้าแบบโมโนลิก  $\beta-Zn_4Sb_3/ZnO$  ถูกสร้างขึ้นตามกระบวนการดังนี้ เริ่มต้นนำผง  $\beta-Zn_4Sb_3$  และ ZnO มาทำการอัดแบบเบาสลับกันโดยแม่พิมพ์โมลดีที่เหลี่ยมขนาด  $1 \times 1 \text{ cm}$  ที่ความดัน 100 MPa จากนั้นนำไปทำการอัดรวมเม็ดหลายชั้นด้วยความดัน 700 MPa เป็นเวลา 15 นาที นำเม็ด  $\beta-Zn_4Sb_3/ZnO$  ที่ได้ไปเผาหลอมผลึกที่อุณหภูมิ 500 °C เป็นเวลา 6 ชั่วโมง ภายใต้ระบบแก๊สอาร์กอน จากนั้นนำเม็ดเซรามิก  $\beta-Zn_4Sb_3/ZnO$  ทำการเชื่อมขั้วบวกและขั้วลบ อุปกรณ์โมดูลกำเนิดไฟฟ้าแบบโมโนลิก  $\beta-Zn_4Sb_3/ZnO$  ถูกทำขึ้นสำเร็จแล้ว จากนั้นนำโมดูลที่ได้ไปทำการทดสอบวัด IV และพาวเวอร์เอาต์พุต ด้วยอุปกรณ์ควบคุมอุณหภูมิร้อน/เย็นที่พัฒนาขึ้นเองโดยกำหนดให้อุณหภูมิการทำงาน ( $T_h$ ) 100 °C, 200 °C และ 300 °C กับเกรเดียนต์ของอุณหภูมิ ( $\Delta T$ ) 50 °C และ 100 °C จากการทดสอบพบว่ากราฟ IV มีลักษณะเป็นเส้นตรงแบบขาลงซึ่งตรงตามผลการทดสอบที่ถูกรายงานไว้ในวารสารวิชาการ โดยค่าความต่างศักย์เริ่มต้นหรือแรงดันไฟฟ้าวงจรเปิด (Open-circuit voltage ;  $V_{oc}$ ) มีค่าเพิ่มขึ้นเมื่ออุณหภูมิการทำงานและเกรเดียนต์ของอุณหภูมิเพิ่มขึ้นโดยเงื่อนไขที่ทำให้ได้ค่า  $V_{oc}$  สูงที่สุดที่ 73.1 mV และค่าพาวเวอร์เอาต์พุตสูงสุดที่ประมาณ 550  $\mu W$  ที่อุณหภูมิการทำงานที่  $T_h=300$  °C และ  $\Delta T=100$  °C ตามลำดับ อย่างไรก็ตามการทำงานที่อุณหภูมิการทำงาน  $T_h=200$  °C กับ  $\Delta T=50$  °C และ  $\Delta T=100$  °C ของโมดูลนั้นเหมาะสมกว่าเพราะกราฟพาวเวอร์เอาต์พุต curves ที่กว้างและมีลักษณะคล้ายคลึงกันซึ่งสามารถอธิบายได้ด้วยค่าเพาเวอร์แฟคเตอร์ที่บ่งบอกถึงการทำงานที่ดีของโมดูล

สาขาวิชาฟิสิกส์  
ปีการศึกษา 2566

ลายมือชื่อนักศึกษา \_\_\_\_\_  
ลายมือชื่ออาจารย์ที่ปรึกษา \_\_\_\_\_

TACHGISS JAMPREECHA : FABRICATION, PERFORMANCE AND THERMOELECTRIC PROPERTIES OF MONOLITHIC  $\beta$ -Zn<sub>4</sub>Sb<sub>3</sub>/ZnO THERMOELECTRIC GENERATOR MODULES. THESIS ADVISOR : PROF. SANTI MAENSIRI, D. Phil. 117 PP.

Keyword: THERMOELECTRIC, MOLOLITHIC, THERMOELECTRIC GENERATOR MODULE (TEGs), ZINC ANTIMONIDE

In this research, the processes synthesis and thermoelectric properties of thermoelectric materials of zinc antimony alloy beta phase ( $\beta$ -Zn<sub>4</sub>Sb<sub>3</sub>) powders were studied before the  $\beta$ -Zn<sub>4</sub>Sb<sub>3</sub> powder before using these powders to fabricate monolithic  $\beta$ -Zn<sub>4</sub>Sb<sub>3</sub>/ZnO thermoelectric generator module (TEG). The performance of the monolithic  $\beta$ -Zn<sub>4</sub>Sb<sub>3</sub>/ZnO TEG modules were evaluated using self-made heating/cooling system with IV measurement capabilities. The characterization of processes, structural analysis, fabrication processes and performance evaluation were described in a detailed, step by step.

Initially,  $\beta$ -Zn<sub>4</sub>Sb<sub>3</sub> powders were synthesized through solid state reaction process. Zn and Sb powder were combined in a stoichiometric ratio 4:3, with additional Zn added to compensate for evaporation during high temperature calcination. The optimal amount of added Zn was 12 at.% Zn. The precursor mixture of Zn-Sb powders was calcined at 450 °C for 3 hours under Ar gas flow. The synthesized  $\beta$ -Zn<sub>4</sub>Sb<sub>3</sub> powders were analyzed using X-ray diffraction (XRD) technique. The XRD pattern results showed dominant crystalline structure pure phase of  $\beta$ -Zn<sub>4</sub>Sb<sub>3</sub> and correspondingly Mozharivskyj's model. However, slight diffraction pattern of secondary phase of ZnSb, Zn, and Sb, were also observed due to temperature stability limitations during calcination under Ar gas flow. Additionally, the synthesized  $\beta$ -Zn<sub>4</sub>Sb<sub>3</sub> powders were also investigated ionization energy of exciting core electrons at Zn K-edge and Sb L-edges using normalized X-ray absorption near edge spectroscopy (XANES) and derivative of normalized XANES. The normalized XANES spectrum result of Zn K-edge revealed main absorption edge at 9,659 eV. The main absorption edge of Zn K-edge was confirmed by derivation of normalized XANES spectrum result. For Sb L<sub>3</sub>, L<sub>2</sub> and L<sub>1</sub>-edges, the main absorption edges were observed at 4,132 eV, 4,380 eV and 4,698 eV, respectively, also confirmed by the derivative. The normalized XANES spectra and derivation of normalized XANES spectra results of Zn K-edge and Sb L-edges, indicate that the ionization energy of exciting core electrons corresponds to the oxidation state of Zn<sup>0</sup> and Sb<sup>0</sup>. The synthesized  $\beta$ -Zn<sub>4</sub>Sb<sub>3</sub> powders were pressed into ceramic pellets using circular compression mold. The powders were pressed at 700 MPa. Then the pressed  $\beta$ -Zn<sub>4</sub>Sb<sub>3</sub> pellets were sintered under Ar gas flow at

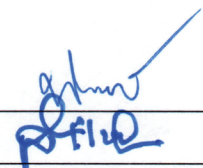
500 °C, and held for 6 hours. Afterwards, thermoelectric properties of the ceramic pellets were investigated. The measurement of the ceramic  $\beta$ -Zn<sub>4</sub>Sb<sub>3</sub> pellets revealed a notable Seebeck coefficient of approximately 255  $\mu\text{V}/^\circ\text{C}$  at 320 °C. Moreover, the electrical resistivity of the ceramic pellets remained consistently poor across the temperature range of 250–400 °C, with a value about  $8 \times 10^{-5} \Omega \cdot \text{m}$ . The high Seebeck coefficient and poor electrical resistivity suggest that the sintered  $\beta$ -Zn<sub>4</sub>Sb<sub>3</sub> pellets have excellent thermoelectric properties, as indicated by the figure of merit (ZT). Additionally, the maximum power factor of the ceramic pellets about 0.56  $\text{mW}/\text{m}^\circ\text{C}^2$  was observed at the optimal performance temperature range of 220–240 °C. Fortunately, the good thermoelectric properties of the synthesized  $\beta$ -Zn<sub>4</sub>Sb<sub>3</sub> powders are preferable for fabrication of monolithic TEG modules.

The monolithic  $\beta$ -Zn<sub>4</sub>Sb<sub>3</sub>/ZnO TEGs were fabricated using cyclical compression process. The synthesized  $\beta$ -Zn<sub>4</sub>Sb<sub>3</sub> powders were first filled into a square compression mold size 1x1 cm, and softly pressed at 100 MPa for a while. Next, the commercial ZnO powders also were filled into the same compression mold, and softly pressed. The soft compression was performed cyclically. Multi-stack of  $\beta$ -Zn<sub>4</sub>Sb<sub>3</sub>/ZnO pellets were firmly hard pressed at 700 MPa for 15 minutes. The pressed multi-stacks pellets were sintered under Ar gas flow at 500 °C for 6 hours. The  $\beta$ -Zn<sub>4</sub>Sb<sub>3</sub> components of the multi-stacks pellet was connected in series with positive and negative terminal. The monolithic  $\beta$ -Zn<sub>4</sub>Sb<sub>3</sub>/ZnO TEGs were evaluated IV-curves and electrical output power curves using custom-built heating/cooling system with IV measurement capabilities. The measurement temperatures were conducted at operating temperature ( $T_h$ ) of 100 °C, 200 °C and 300 °C, with gradient temperature ( $\Delta T$ ) of 50 °C and 100 °C. The results revealed an increase in open-circuit voltage ( $V_{oc}$ ) with higher  $T_h$  and  $\Delta T$ . The highest maximum electrical power output of 550  $\mu\text{W}$ , and the highest  $V_{oc}$  of 73.1 mV were achieved at  $T_h=300$  °C with  $\Delta T=100$  °C. However, the optimal operating conditions for the monolithic  $\beta$ -Zn<sub>4</sub>Sb<sub>3</sub>/ZnO TEG was found to be  $T_h=200$  °C with  $\Delta T=50$  °C and  $\Delta T=100$  °C, as these conditions demonstrate a wide and prominent electrical power output curves, indicating good performance of the module.

School of Physics  
Academic Year 2023

Student's Signature \_\_\_\_\_

Advisor's Signature \_\_\_\_\_



## ACKNOWLEDGEMENTS

I would like to express my heartfelt gratitude to everyone who supported, advised, and contributed to my research thesis, providing me with invaluable opportunities and experiences in the field of physics and materials science research. Special gratitude to my thesis advisor, Prof. Dr. Santi Maensiri, for the guidance in honing my research skills and for providing numerous opportunities to refine my presentation abilities in national and international conferences.

I extend my sincere appreciation to the esteemed members of the 'Advanced Materials Physics Laboratory' research group for their invaluable assistance and insightful suggestions throughout my Ph.D. research.

I am also deeply grateful to my friends, colleagues, and the graduate student community of SUT and KKU for their constant support and helpful suggestions.

Lastly, I would like to express my profound gratitude to my parents Mr. Wuttisak Jampreecha, Mrs. Sumalee Jampreecha and my brother, Mr. Wisanu Jampreecha for their unwavering support and encouragement throughout my Ph.D. study journey.

Tachgiss Jampreecha

มหาวิทยาลัยเทคโนโลยีสุรนารี

# CONTENTS

	Page
ABSTRACT IN THAI .....	I
ABSTRACT IN ENGLISH .....	III
ACKNOWLEDGEMENTS .....	V
CONTENTS .....	VI
LIST OF FIGURES .....	VIII
LIST OF TABLES .....	XIII
<b>CHAPTER</b>	
<b>I INTRODUCTION.....</b>	<b>1</b>
1.1 Background and motivation .....	1
1.2 Objectives of the research.....	3
1.3 Scope and limitation.....	3
1.4 Location of the research.....	4
1.5 Outline of thesis.....	4
<b>II LITERATURE REVIEW.....</b>	<b>5</b>
2.1 Thermoelectricity.....	5
2.1.1 Introduction .....	5
2.1.2 Theoretical background .....	5
2.1.3 Effects in a magnetic Field .....	18
2.1.4 Transport effects.....	20
2.1.5 Thermoelectric refrigerators.....	21
2.1.6 Thermoelectric generators .....	22
2.2 Thermoelectric materials .....	23
2.2.1 Thermoelectric materials.....	23
2.2.2 Process synthesis.....	30
2.2.3 Beta zinc antimonide $\beta$ -Zn <sub>4</sub> Sb <sub>3</sub> .....	36
2.3 Thermoelectric generator modules.....	46
<b>III EXPERIMENTAL PROCEDURE .....</b>	<b>53</b>
3.1 Synthesis of $\beta$ -Zn <sub>4</sub> Sb <sub>3</sub> powders.....	53
3.2 Fabrication of sintered $\beta$ -Zn <sub>4</sub> Sb <sub>3</sub> pellets.....	55
3.3 Fabrication of test cells monolithic $\beta$ -Zn <sub>4</sub> Sb <sub>3</sub> /ZnO TEG module .....	58

## CONTENTS (Continued)

	Page
3.4 Fabrication of monolithic multi-stack $\beta$ -Zn <sub>4</sub> Sb <sub>3</sub> /ZnO TEG module.....	60
3.5 Materials characterization .....	61
3.5.1 X-ray diffraction.....	61
3.5.2 X-ray absorption spectroscopy.....	62
3.6 Thermoelectric properties .....	64
3.7 Module evaluation .....	65
<b>IV RESULTS AND DISCUSSION .....</b>	<b>67</b>
4.1 X-ray diffraction .....	67
4.2 X-ray absorption spectroscopy.....	75
4.3 Thermoelectric properties .....	80
4.4 Module analysis and evaluation.....	83
<b>V CONCLUSION AND SUGGESTION.....</b>	<b>93</b>
5.1 Structure and characterization .....	94
5.2 Thermoelectric properties .....	94
5.3 Module analysis and evaluation.....	95
5.4 Suggestion.....	95
REFERENCES .....	95
APPENDICES.....	106
APPENDIX A PUBLICATION AND PRESENTATION .....	106
APPENDIX B FIGURE AND TABLE .....	107
CURRICULUM VITAE.....	117

## LIST OF FIGURES

Figure	Page
1 Illustration of Seebeck effect, adapted from Saini <i>et al.</i> , 2021 .....	6
2 Illustration of Peltier effect, adapted from Saini <i>et al.</i> , 2021.....	7
3 Illustration to demonstrate Thomson effect (Morrison and Dejene, 2020).....	8
4 The thermogalvanomagnetic effects with different directions of involved para meters (Goldsmid, 2010). .....	19
5 Illustration of model a couple p–n pair refrigerator (Goldsmid, 2010).....	21
6 Illustration of model a couple p–n generator (Goldsmid, 2010) .....	23
7 Illumination of n–type and p–type of thermoelectric materials behaviour (Nabilasamiron, 2012). .....	24
8 Summary of ZT as a functional temperature of p–type and n–type of the rmo– electric materials, a) p–type thermoelectric materials and b) n–type thermoelectric materials (Rull–Bravo <i>et al.</i> , 2015).....	26
9 Schematic of sol–gel method step by step (Bokov <i>et al.</i> , 2021). .....	30
10 Schematic diagram illustrating the hot pressing technique (Moustafa et al., 2011). .....	31
11 DC magnetron sputtering and. Pulsed DC magnetron sputtering (Vaccoat, 2024).....	32
12 Illustration of Spark plasma sintering technique (Max Planck Institutes). .....	33
13 Illustration of quenching process after melting process.....	34
14 Mechanical alloying with flat and crack bulk sample (Kumar <i>et al.</i> , 2022). .....	35
15 Schematic representation of solid–state reaction method (Sodhiya <i>et al.</i> , 2021).....	36
16 (a) Crystalline structure model of Zn <sub>39</sub> Sb <sub>30</sub> and (b) Crystalline structure model of Zn <sub>13</sub> Sb <sub>10</sub> (Zou <i>et al.</i> , 2015). .....	37
17 Crystalline structure model of Zn <sub>6</sub> Sb <sub>5</sub> (Mayer <i>et al.</i> , 1978). .....	37
18 Calculated X–ray diffraction pattern yields of Zn <sub>39</sub> Sb <sub>30</sub> model by using Boru’s CIF– 7040405 (Borup <i>et al.</i> , 2016). .....	40
19 Calculated X–ray diffraction pattern yields of Zn <sub>6</sub> Sb <sub>5</sub> model by using Jeffrey Snyder’s CIF–cm0515505_si_001(Snyder <i>et al.</i> , 2004).....	40
20 Calculated X–ray diffraction pattern yields of Zn <sub>13</sub> Sb <sub>10</sub> model by using Yurij’s CIF– 4001474 (Mozharivskij <i>et al.</i> , 2006). .....	41

## LIST OF FIGURES (Continued)

Figure	Page
21 XRD yields of ZnSd (top) and Zn <sub>4</sub> Sb <sub>3</sub> (bottom) were prepares by quenching method (Böttger <i>et al.</i> , 2011). .....	42
22 XRD pattern of $\beta$ -Zn <sub>4</sub> Sb <sub>3</sub> with 0.6 at. % Zn rich via different sintered tempe ratures in vacuum (Lee and Lin, 2018). .....	43
23 XRD pattern of milled $\beta$ -Zn <sub>4</sub> Sb <sub>3</sub> with different at. % Zn rich (Lee and Lin, 2018). .....	44
24 SEM images of $\beta$ -Zn <sub>4</sub> Sb <sub>3</sub> powder; (a) Before mechanical alloying method and (b) After mechanical alloying method (Ur <i>et al.</i> , 2003). .....	44
25 SEM images of hot-pressed $\beta$ -Zn <sub>4</sub> Sb <sub>3</sub> ceramic at temperatures of 373 K, 473 K, 573 K and 673 K with pressure 0.98 GPa (Lee and Lin, 2018). .....	45
26 SEM images of hot-pressed $\beta$ -Zn <sub>4</sub> Sb <sub>3</sub> ceramic with pressing pressures of 100 MPa (a) and 200 MPa (b) at 673 K (Ahn <i>et al.</i> , 2011). .....	45
27 Seebeck coefficient, thermal conductivity and electrical conductivity of hot-pressed $\beta$ -Zn <sub>4</sub> Sb <sub>3</sub> ceramic pellets via different temperatures and pressure (Ahn <i>et al.</i> , 2011). .....	46
28 Schematic of a dual leg TEG module and dual leg series TEG device with isotropic properties (Crawford, 2014). .....	47
29 Schematic of sing leg TEG module with isotropic properties (Crawford, 2014). .....	48
30 Schematic of serpentine and tilted-multilayer TTE module with anisotropic thermoelectric properties (Goldsmid, 2017). .....	48
31 (a) Photograph of misaligned make assembly equipment for sputtering Bi/Bi <sub>0.5</sub> Sb <sub>1.5</sub> Te <sub>3</sub> TTE device, (b) Illustration of layer by layer stacking of Bi/Bi <sub>0.5</sub> Sb <sub>1.5</sub> Te <sub>3</sub> (Mu <i>et al.</i> , 2019). .....	49
32 Tilted ceramic block TTE device prepared by La <sub>1.97</sub> Sr <sub>0.03</sub> CuO <sub>4</sub> with silver paste connector (Dreßler <i>et al.</i> , 2015). .....	50
33 Schematic of dual leg, unileg and transverse series monolithic TEG device (Dreßler <i>et al.</i> , 2015). .....	51
34 Illustration of charge positions of all monolithic TEGs model. ....	51
35 Monolithic Ag <sub>2</sub> S <sub>0.2</sub> Se <sub>0.8</sub> / Ag <sub>2</sub> S /Bi <sub>0.5</sub> Sb <sub>1.5</sub> Te <sub>3</sub> TEG modules. ....	52

## LIST OF FIGURES (Continued)

Figure	Page
36	Process synthesis of $\beta$ -Zn <sub>4</sub> Sb <sub>3</sub> powders: a) Premixed powders with zirconia balls were filled into a PP bottle, b) The filled PP bottle was rotated using roller milling machine, c) The mixture powders were calcined under Ar gas flowing, and d) Synthesized $\beta$ -Zn <sub>4</sub> Sb <sub>3</sub> powders..... 54
37	The $\beta$ -Zn <sub>4</sub> Sb <sub>3</sub> bulk pellets after were pressed at 500 and 700 MPa, respectively..... 56
38	The sintered $\beta$ -Zn <sub>4</sub> Sb <sub>3</sub> pellets after were sintered at 500 °C, 550 °C, 575 °C and 600 °C for 6 hours..... 57
39	The cyclical compression process for preparing $\beta$ -Zn <sub>4</sub> Sb <sub>3</sub> /ZnO pellets. .... 59
40	The test cells of monolithic $\beta$ -Zn <sub>4</sub> Sb <sub>3</sub> /ZnO TEGs versus weight size of $\beta$ -Zn <sub>4</sub> Sb <sub>3</sub> pellets part. .... 59
41	Fabrication processes of monolithic $\beta$ -Zn <sub>4</sub> Sb <sub>3</sub> /ZnO TEGs: a) compressed multi-stacks $\beta$ -Zn <sub>4</sub> Sb <sub>3</sub> /ZnO pellet, b) sintered multi-stacks $\beta$ -Zn <sub>4</sub> Sb <sub>3</sub> /ZnO pellet, c) connected electrical wire with zigzags connection of monolithic $\beta$ -Zn <sub>4</sub> Sb <sub>3</sub> /ZnO TEGs, and d) monolithic $\beta$ -Zn <sub>4</sub> Sb <sub>3</sub> TEGs was plastered with cement filler. .... 60
42	Shows x-ray incident and diffraction, according to Bragg's law ( <a href="http://www.didaktik.physik.uni-muenchen.de/elektronenbahnen/en/index.php">www.didaktik.physik.uni-muenchen.de/elektronenbahnen/en/index.php</a> )..... 62
43	Shows X-ray diffraction machine, D8-Bruker, SUT..... 62
44	Illustration of a x-ray absorption energies of K edge, L edges and M edges (Chem.libretexts, 2000). .... 63
45	Illustration of x-ray absorption transmission mode (Mit.edu, 2004). .... 64
46	Illustration of Seebeck coefficient and electrical resistivity (Linseis, 2024). .... 64
47	LINSEIS LSR-3 Seebeck type resistivity measurement system ..... 65
48	The self-made heating/cooling system with IV measurement capabilities. .... 66
49	X-ray diffraction patterns of the synthesized $\beta$ -Zn <sub>4</sub> Sb <sub>3</sub> powders under conditions of calcination temperature non-calcined, 300 °C, 400 °C and 500 °C without excess of Zn..... 68
50	The comparison XRD pattern of the synthesized $\beta$ -Zn <sub>4</sub> Sb <sub>3</sub> powders under varying excessed Zn condition via calcination temperature 400 °C and held for 3 hours..... 69

## LIST OF FIGURES (Continued)

Figure	Page
51 XRD pattern of varying holding time via excessing Zn of 10 at.% Zn and calcination temperature 400 °C. ....	70
52 The comparison XRD pattern of the synthesized $\beta$ -Zn <sub>4</sub> Sb <sub>3</sub> powders under varying calcination temperature at 350 °C, 400 °C and 450 °C via adding 10 at.% Zn and calcination holding time for 3 hour. ....	71
53 Comparison XRD pattern of the synthesized $\beta$ -Zn <sub>4</sub> Sb <sub>3</sub> powders under excessing Zn for 10, 11, 12, 13 and 14 at.% Zn and calcination at 450 °C for 3 hours. ....	72
54 Comparison XRD pattern of the synthesized $\beta$ -Zn <sub>4</sub> Sb <sub>3</sub> powders under excessing Zn for 10, 11, 12, 13 and 14 at.% Zn and calcination at 400 °C for 3 hours. ....	73
55 Comparison XRD pattern of the synthesized $\beta$ -Zn <sub>4</sub> Sb <sub>3</sub> powders under excessing Zn for 10, 11, 12, 13 and 14 at.% Zn and calcination at 425 °C for 3 hours. ....	74
56 Comparison of synthesis series of excessing Zn for 10, 11, 12, 13, 14 and 15 at.% Zn and calcination at 400 °C, 425 °C, 450 °C for 3 hours of. ....	75
57 Normalized XANES of Zn K-edge of the high pure synthesized $\beta$ -Zn <sub>4</sub> Sb <sub>3</sub> powder. ....	76
58 Derivative normalized XANES of Zn K-edge of the high pure synthesized $\beta$ -Zn <sub>4</sub> Sb <sub>3</sub> powder. ....	77
59 Normalized XANES of Sb L3, L2 and L1-edge of the high pure synthesized $\beta$ -Zn <sub>4</sub> Sb <sub>3</sub> powder. ....	78
60 Derivative normalized XANES of Sb L3, L2 and L1-edge of the high pure synthesized $\beta$ -Zn <sub>4</sub> Sb <sub>3</sub> powder. ....	79
61 Seebeck coefficient of the sintered $\beta$ -Zn <sub>4</sub> Sb <sub>3</sub> pellets versus varying temperature. ....	81
62 Electrical resistivity of the sintered $\beta$ -Zn <sub>4</sub> Sb <sub>3</sub> pellets versus varying temperature. ....	82
63 Electrical power factor of the sintered $\beta$ -Zn <sub>4</sub> Sb <sub>3</sub> pellets versus varying temperature. ....	83
64 IV-curve of the test cells of monolithic $\beta$ -Zn <sub>4</sub> Sb <sub>3</sub> /ZnO TEGs under condition of weight 1.0 g versus different operating Th and $\Delta T$ . ....	83

## LIST OF FIGURES (Continued)

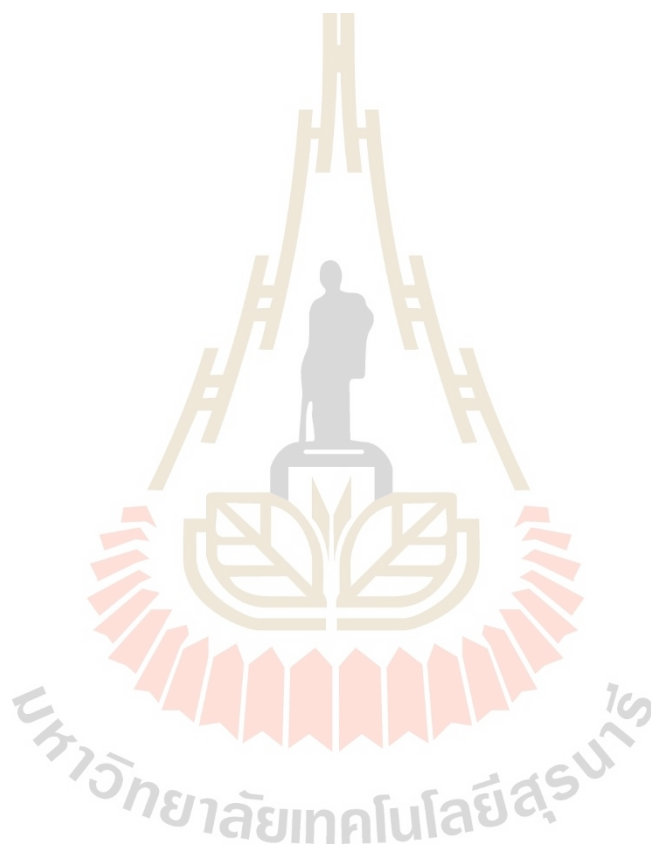
Figure	Page
65	87
Electrical power output curves of the test cells of monolithic $\beta$ -Zn <sub>4</sub> Sb <sub>3</sub> /ZnO TEG module under condition of weight 1.0 g versus different operating $T_h$ and $\Delta T$ .....	
66	89
IV characteristics of the monolithic multi-stack $\beta$ -Zn <sub>4</sub> Sb <sub>3</sub> /ZnO TEGs versus varying operation hot side temperature and temperature gradients $\Delta T$ .....	
67	91
Electrical power output curves of the monolithic multi-stack $\beta$ -Zn <sub>4</sub> Sb <sub>3</sub> /ZnO TEGs versus varying operation hot side temperature and temperature gradients $\Delta T$ .....	
68	107
IV-curve of the test cells of monolithic $\beta$ -Zn <sub>4</sub> Sb <sub>3</sub> /ZnO TEGs under condition of weight 0.2 g versus different operating $T_h$ and $\Delta T$ .....	
69	108
IV-curve of the test cells of monolithic $\beta$ -Zn <sub>4</sub> Sb <sub>3</sub> /ZnO TEGs under condition of weight 0.5 g versus different operating $T_h$ and $\Delta T$ .....	
70	109
IV-curve of the test cells of monolithic $\beta$ -Zn <sub>4</sub> Sb <sub>3</sub> /ZnO TEGs under condition of weight 2.0 g versus different operating $T_h$ and $\Delta T$ .....	
71	110
IV-curve of the test cells of monolithic $\beta$ -Zn <sub>4</sub> Sb <sub>3</sub> /ZnO TEGs under condition of weight 4.0 g versus different operating $T_h$ and $\Delta T$ .....	
72	111
Electrical power output curves of the test cells of monolithic $\beta$ -Zn <sub>4</sub> Sb <sub>3</sub> /ZnO TEG module under condition of weight 0.2 g versus different operating $T_h$ and $\Delta T$ .....	
73	112
Electrical power output curves of the test cells of monolithic $\beta$ -Zn <sub>4</sub> Sb <sub>3</sub> /ZnO TEG module under condition of weight 0.5 g versus different operating $T_h$ and $\Delta T$ .....	
74	113
Electrical power output curves of the test cells of monolithic $\beta$ -Zn <sub>4</sub> Sb <sub>3</sub> /ZnO TEG module under condition of weight 2.0 g versus different operating $T_h$ and $\Delta T$ .....	
75	114
Electrical power output curves of the test cells of monolithic $\beta$ -Zn <sub>4</sub> Sb <sub>3</sub> /ZnO TEG module under condition of weight 4.0 g versus different operating $T_h$ and $\Delta T$ .....	

## LIST OF TABLES

Table	Page
1 List of thermoelectric materials versus operating temperatures, power factor, synthesis method and ZT. ....	27
2 Comparison of structure model $\beta$ -Zn <sub>4</sub> Sb <sub>3</sub> with intermediate step to interstitial model (Snyder <i>et al.</i> , 2004). ....	39
3 Series conditions of process synthesis of $\beta$ -Zn <sub>4</sub> Sb <sub>3</sub> powders versus excess Zn, calcination temperature and calcination holding time.....	55
4 Pressure in compression process with calculation density of pressed $\beta$ -Zn <sub>4</sub> Sb <sub>3</sub> pellets. ....	56
5 List of open-circuit voltage ( $V_{op}$ ) and short circuit current ( $I_{sc}$ ) versus varying operating condition temperature of the test cells of monolithic couple $\beta$ -Zn <sub>4</sub> Sb <sub>3</sub> /ZnO TEGs with condition of 0.5 g, 1.0 g, 2.0 g and 4.0 g.....	85
6 Comparison of maximum electrical power output of test cell of monolithic $\beta$ -Zn <sub>4</sub> Sb <sub>3</sub> /ZnO TEG module under condition of weight 1.0 g for different conditions of $T_h$ and $\Delta T$ . ....	88
7 List of open-circuit voltage ( $V_{op}$ ) and short circuit current ( $I_{sc}$ ) versus varying operating condition temperature of the monolithic multi-stack $\beta$ -Zn <sub>4</sub> Sb <sub>3</sub> /ZnO TEGs. ....	89
8 Results of the maximum electrical power output for different conditions of hot-side temperature and $\Delta T$ of the monolithic $\beta$ -Zn <sub>4</sub> Sb <sub>3</sub> /ZnO TEGs. ....	90
9 Comparison of the maximum electrical power output versus variant mono lithic TEG modules of this work and literature reports.....	92
10 Comparison of maximum electrical power output of test cell of monolithic $\beta$ -Zn <sub>4</sub> Sb <sub>3</sub> /ZnO TEG module under condition of weight 0.2 g for different conditions of $T_h$ and $\Delta T$ . ....	115
11 Comparison of maximum electrical power output of test cell of monolithic $\beta$ -Zn <sub>4</sub> Sb <sub>3</sub> /ZnO TEG module under condition of weight 0.5 g for different conditions of $T_h$ and $\Delta T$ . ....	115
12 Comparison of maximum electrical power output of test cell of monolithic $\beta$ -Zn <sub>4</sub> Sb <sub>3</sub> /ZnO TEG module under condition of weight 2.0 g for different conditions of $T_h$ and $\Delta T$ . ....	116

## LIST OF TABLES (Continued)

Table		Page
13	Comparison of maximum electrical power output of test cell of monolithic $\beta$ -Zn <sub>4</sub> Sb <sub>3</sub> /ZnO TEG module under condition of weight 4.0 g for different conditions of T <sub>h</sub> and $\Delta$ T .....	116



# CHAPTER I

## INTRODUCTION

### 1.1 Background and motivation

The global demand for energy usage is rising significantly, which the electricity consumption is a major problem. Additionally, the crisis of using energy from crude oil, natural gas and nuclear power contributes to global warming, and emits radioactive pollutants that harm the environment. Therefore, it is crucial to explore and utilize alternative energy sources such as hydropower, wind energy, solar energy and geothermal energy. Research and innovation are essential for converting these alternative energies into electricity. For example, such as converting solar energy can be converted into electricity using solar cell devices, while hydropower and wind energy can be converted into electricity using dynamo, and Thermoelectric generators can generate electricity from natural heat sources and solar thermal energy.

Thermoelectric generator (TEG) modules are components used in electronic devices to directly convert heat to electrical current, serving as an electrical power source for the electronic devices. The heat to electricity conversion is known as the “Thermoelectric effect”, first discovered by Thomas Johann Seebeck (Goldsmid, 2010). Normally, conventional TEGs, or longitudinal TEGs are typically constructed using a dual-leg model, which incorporates a couple of thermoelectric materials P-type and N-type. This dual-leg model allow for parallel flow of electric and heat transport with isotropic properties (Crawford, 2014). In contrast, a single leg model uses only one type of thermoelectric materials, either P-type or N-type. Both TEG model require alternative materials for electrical insulation materials for separating TEG cells and electrical conduction materials, i.e., ZO, SiO<sub>2</sub>, Ag, Ag<sub>2</sub>S-alloy (Lai *et al.*, 2022). To evaluate the efficiency of the initial thermoelectric materials use in fabricating TEGs, the dimensionless parameter known as the “the figure of merit (ZT is commonly employed. This parameter is given by the equation of  $ZT = \frac{\alpha^2 \sigma T}{\kappa}$  where ZT, T,  $\alpha$ ,  $\kappa$  and  $\sigma$  are dimensionless figure of merit, operating temperature (K), Seebeck coefficient (V/K), thermal conductivity (W/Km) and electrical conductivity (S/m or  $\Omega^{-1}m^{-1}$ ), respectively. This equation was defined and conceptualized by Edmund Altenkirch

(Saini *et al.*, 2021). Due to most industrial waste heat is released at temperatures of about 200–400°C (Minea, 2007). It presents a valuable opportunity as a recyclable energy source. This waste heat can generate electrical power through the use of high-temperature TEGs. A literature survey of thermoelectric materials suitable for these temperatures includes  $\beta$ -Zn<sub>4</sub>Sb<sub>3</sub>, NaPb<sub>20</sub>SbTe<sub>22</sub> (salt), PbTe, PbTe–PbS, AgSbTe<sub>2</sub>–GeTe (TAGS), Ba<sub>0.08</sub>La<sub>0.05</sub>Yb<sub>0.04</sub>Co<sub>4</sub>Sb<sub>12</sub> (skutterudite) and AgPb<sub>18</sub>SbTe<sub>20</sub> (LAST) (Caillat *et al.*, 1997; Poudeu *et al.*, 2006; Biswas *et al.*, 2012; Levin *et al.*, 2012; Shi *et al.*, 2011; Hsu *et al.*, 2004; Rull-Bravo *et al.*, 2015). Among these materials,  $\beta$ -Zn<sub>4</sub>Sb<sub>3</sub> is considered the most effective due to its high ZT at value at waste heat temperatures, inexpensive materials, and uncomplicated crystalline structure. Originally, Zn<sub>4</sub>Sb<sub>3</sub> has three polymorphs:  $\alpha$ -Zn<sub>4</sub>Sb<sub>3</sub>,  $\beta$ -Zn<sub>4</sub>Sb<sub>3</sub> and  $\gamma$ -Zn<sub>4</sub>Sb<sub>3</sub>, each with unique thermoelectric properties (Seebeck, 1895; Mönkemeyer, 1905; Beer and Cochran, 1952; Mayer *et al.*, 1978). However, the  $\beta$ -Zn<sub>4</sub>Sb<sub>3</sub> polymorph in space group R $\bar{3}c$  is the most efficient, exhibiting a significant Seebeck coefficient at operating temperature about 200–400 °C, with a maximum figure of merit (ZT) of approximately 1.3 (Caillat *et al.*, 1997).

The monolithic architecture of TEG modules offers an all-in-one structural design that simplifies fabrication processes. A monolithic Ag<sub>2</sub>S<sub>0.2</sub>Se<sub>0.8</sub>/Ag<sub>2</sub>S/Bi<sub>0.5</sub>Sb<sub>1.5</sub>Te<sub>3</sub> TEG module and fabrication process were reported by Huajun L. and research team. This dual leg series TEG module comprises three alloys materials: Ag<sub>2</sub>S<sub>0.2</sub>Se<sub>0.8</sub>, Bi<sub>0.5</sub>Sb<sub>1.5</sub>Te<sub>3</sub>, Ag<sub>2</sub>S as n-type, p-type and insulator materials respectively (Lai *et al.*, 2022; Dreßler *et al.*, 2015). However, this TEG module is limited to low-temperature applications due to the properties of Ag<sub>2</sub>S<sub>0.2</sub>Se<sub>0.8</sub> and Bi<sub>0.5</sub>Sb<sub>1.5</sub>Te<sub>3</sub> (Mansouri *et al.*, 2021; Singh *et al.*, 2020). Additionally, the Ag<sub>2</sub>S components are prepared separately to create Ag<sub>2</sub>S spacer layers, which adds complexity to the fabrication process.

This report presents the fabrication of single-leg series monolithic  $\beta$ -Zn<sub>4</sub>Sb<sub>3</sub>/ZnO TEG modules, designed for easier manufacturing processes and the recycling of industrial waste heat. The design incorporates a modified zigzag electrical connection circuit. In this configuration,  $\beta$ -Zn<sub>4</sub>Sb<sub>3</sub> is used as the p-type thermoelectric materials, while ZnO serves as the insulator materials (Jantrasee *et al.*, 2016). The  $\beta$ -Zn<sub>4</sub>Sb<sub>3</sub> powers were synthesized by solid-state reaction and calcination under Ar gas flow. The prepared powders were characterized and then used to produce sintered  $\beta$ -Zn<sub>4</sub>Sb<sub>3</sub> pellets. Then, thermoelectric properties of the sintered  $\beta$ -Zn<sub>4</sub>Sb<sub>3</sub> pellets were evaluated. The performance efficiency of the monolithic  $\beta$ -Zn<sub>4</sub>Sb<sub>3</sub>/ZnO TEG modules was assessed based on their electrical power output. This was calculated using the

equation of  $P_{\text{out}} = NI^2R_L = N \left[ \frac{S(T_h - T_c)}{R_g + R_L} \right]^2 R_L$  where  $P_{\text{out}}$ ,  $N$ ,  $S$ ,  $T_h$ ,  $T_c$ ,  $I$ ,  $R_g$  and  $R_L$  are

electrical power output, number of TEG cells, Seebeck coefficient, temperature of the hot side, temperature of the cold side, electrical current, thermal resistance and load resistance (Goldsmid, 2010), respectively.

## 1.2 Objectives of the research

1.2.1 To synthesize zinc antimony alloy beta phase ( $\beta\text{-Zn}_4\text{Sb}_3$ ) powders using solid state reaction and calcination under Ar gas flow.

1.2.2 To characterize the synthesized  $\beta\text{-Zn}_4\text{Sb}_3$  powders using advanced X-ray measurement techniques (XRD-D8), X-ray absorption near-edge structure (XANES) spectra, and derivative of normalized XANES techniques.

1.2.3 To study and analyze thermoelectric properties of the synthesized  $\beta\text{-Zn}_4\text{Sb}_3$  powders (Seebeck coefficient, electrical resistivity and power factor) using Linseis LSR-3 equipment.

1.2.4 To fabricate monolithic  $\beta\text{-Zn}_4\text{Sb}_3/\text{ZnO}$  thermoelectric generator (TEG) modules.

1.2.5 To develop custom-built heating/cooling system with IV measurement capabilities for evaluating the performance of the fabricated monolithic  $\beta\text{-Zn}_4\text{Sb}_3/\text{ZnO}$  TEG modules.

1.2.6 To evaluate IV characteristics and electrical power output of the monolithic  $\beta\text{-Zn}_4\text{Sb}_3/\text{ZnO}$  TEG modules.

1.2.7 To analyze the performance of the monolithic  $\beta\text{-Zn}_4\text{Sb}_3/\text{ZnO}$  TEG modules by varying operating temperature.

## 1.3 Scope and limitation

1.3.1 The research focuses on synthesis zinc antimony alloy beta phase ( $\beta\text{-Zn}_4\text{Sb}_3$ ) powders using solid state reaction and calcination under Ar gas flow. It also includes fabricating monolithic  $\beta\text{-Zn}_4\text{Sb}_3/\text{ZnO}$  thermoelectric generator modules base on the synthesized  $\beta\text{-Zn}_4\text{Sb}_3$  powders and developing custom-built heating/cooling system with IV measurement capabilities to evaluate its performance.

1.3.2 The crystalline structure phase and ionization energy of core electrons in the synthesized  $\beta\text{-Zn}_4\text{Sb}_3$  powders were analyzed using a literatures review and compared with standard data and model.

1.3.3 Thermoelectric properties of sintered  $\beta$ -Zn<sub>4</sub>Sb<sub>3</sub> pellets and the performance of the monolithic  $\beta$ -Zn<sub>4</sub>Sb<sub>3</sub>/ZnO TEG modules were investigated and evaluated.

## 1.4 Location of the research

1.4.1 Advanced Materials Physics Laboratory (AMP), School of Physics, Institute of Science, Suranaree University of Technology, Nakhon Ratchasima, Thailand.

1.4.2 Facility Building 10 (F10), Suranaree University of Technology, Nakhon Ratchasima, Thailand.

1.4.3 Synchrotron Light Research Institute (BL 5.2), Nakhon Ratchasima, Thailand.

1.4.4 Department of Physics, Faculty of Science, Khon Kaen University, Khon Kaen, Thailand.

## 1.5 Outline of thesis

This thesis consists of five chapters. The first chapter introduces the background and motivation for this research. Chapter II represents literatures reports, providing information on zinc antimony materials, the theory of thermoelectric effect and relevant equations, process synthesis, characterization techniques, fabrication methods for thermoelectric generator modules, and development of a custom-built heating/cooling system with IV measurement capabilities. It also covers the investigation and evaluation of thermoelectric properties and the performance of thermoelectric generator modules respectively. Chapter III describes the preparation of  $\beta$ -Zn<sub>4</sub>Sb<sub>3</sub> powders and sintered  $\beta$ -Zn<sub>4</sub>Sb<sub>3</sub> pellets, characterization techniques, investigation methods, and the fabrication of monolithic  $\beta$ -Zn<sub>4</sub>Sb<sub>3</sub>/ZnO thermoelectric generator modules, including custom-built heating/cooling system with IV measurement capabilities. Chapter IV presents experimental results and discussions. Finally, Chapter V summarized the conclusion and offers suggestion.

## CHAPTER II

### LITERATURE REVIEW

#### 2.1 Thermoelectricity

##### 2.1.1 Introduction

Thermoelectric technology, a renewable energy, has been used to directly convert heat into electricity current since 19th century. The first discovery of the thermal effect was found by Thomas Johann Seebeck in 1821. This phenomenon exposed that an electromotive current could be generated by heating a junction between different metals, this phenomenon is known as “Seebeck effect” (Goldsmid, 2010). A few years later, Jean Charles Athanase Peltier’s experiment demonstrated that heating and cooling could be induced by applying electrical current through metallic thermocouples. This phenomenon became known as the “Peltier effect” (Crawford, 2014). In 1855, W. Thomson (Lord Kelvin) described correlation between Seebeck effect and Peltier effect, which become known as “Kelvin relation” (applied with Onsager relation). Furthermore, W. Thomson also defined “Thomson effect” by applying thermodynamic theory to describe reversible heating and cooling along with the flow of electrical current and temperature gradient. Then, Edmund Altenkirch was the first one who derived the maximal efficiency of thermoelectric generator using constant properties of heat supply and output power per unit time. Edmund Altenkirch also provided the first correct calculation of thermoelectric power generator and defined concept of “figure of merit” which indicates that optimal thermoelectric materials should expressed a high Seebeck coefficient, high electrical conductivity and low thermal conductivity. Later in 1949, Abram Fedorovich Ioffe developed the modern dimensionless parameter of “figure of merit (ZT)” which approximates constant thermoelectric properties to indicating performance of thermoelectric materials (Saini *et al.*, 2021). Nowadays, thermoelectric properties have been developed in semiconductor materials (p-type and n-type), alloy materials, and oxide materials for use in electrical devices and industrials engines.

##### 2.1.2 Theoretical background

As well known, Thomas Johann Seebeck was the first one who found

the phenomenon of electromotive current occurring at the junctions of two different conductor metals (A–B junctions). This phenomenon occurred when the junctions were subjected to a temperature difference, with one end being heated and the other cooled. The phenomena, known as “Seebeck effect” (Goldsmid, 2010). The Seebeck effect is illustrated in Figure 1. The mathematical parameters of the Seebeck effect relations describe temperature gradient across the junctions (A–B junctions) ( $\Delta T$  or  $T_H - T_C$ ), the potential difference between the end of the junctions ( $\Delta V$ ), and a parameter called “Seebeck coefficient” ( $\alpha$ ). The Seebeck effect relations is represented by the equation below.

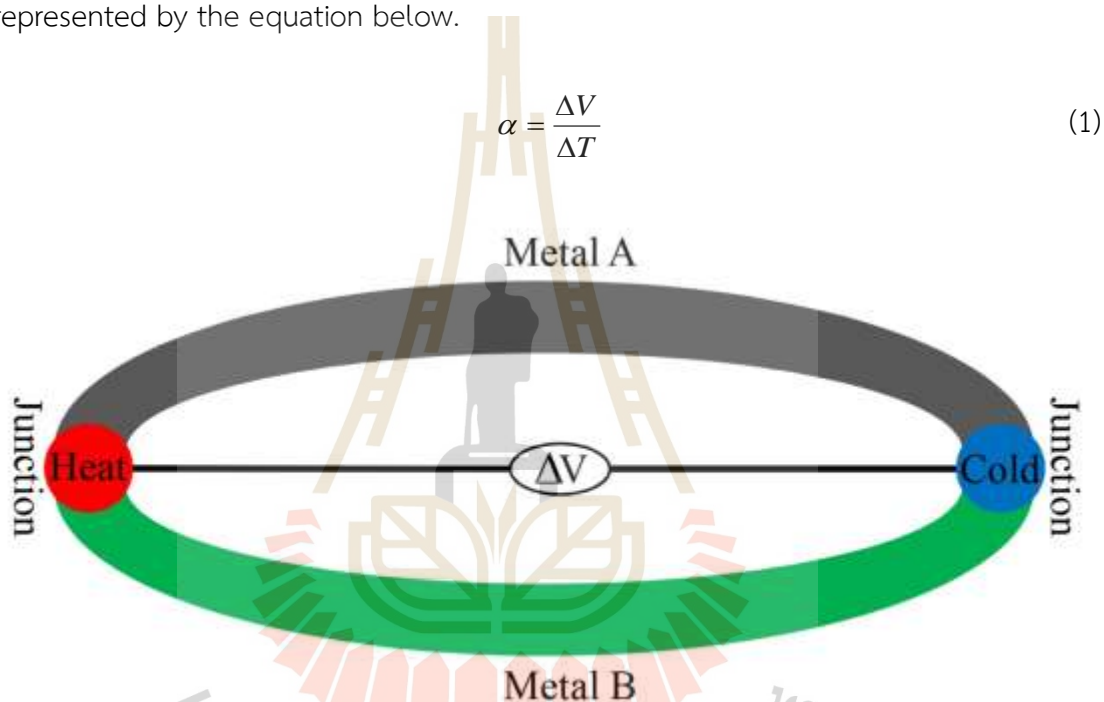


Figure 1 Illustration of Seebeck effect, adapted from Saini *et al.*, 2021 .

Jean Charles Athanase Peltier’s experiment demonstrated a slight change in temperature in a thermocouple when an electrical current was passed through it. The effect is associated with the heat transfer that occurs when electrical current was applied to the conductor metals junctions (A–B junctions), causing heating at one junction and cooling at the other. This phenomenon, known as the "Peltier effect," is illustrated in Figure 2. The mathematical parameters of Peltier effect relations describe release/absorption rate at the junctions ( $Q$ ), electrical current supply ( $I$ ) and a parameter named “Peltier coefficient” ( $\Pi$ ). Peltier coefficient relations is represented by equation (2).

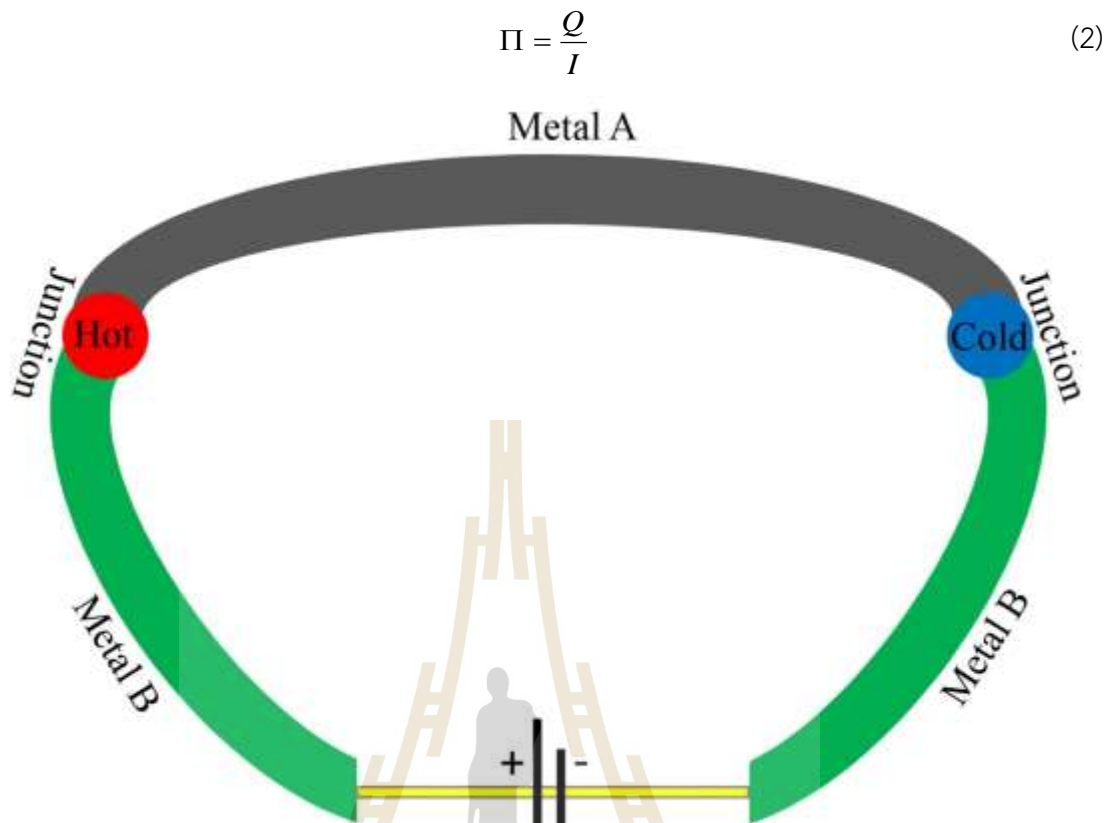


Figure 2 Illustration of Peltier effect, adapted from Saini *et al.*, 2021.

W. Thomson, also known as Lord Kelvin, established a connection between relation of the Seebeck coefficient and the Peltier coefficient using thermodynamic theory, a correlation known as the “Kelvin relation”, as shown in equation below.

$$\Pi = \alpha T \quad (3)$$

Moreover, W. Thomson defined the “Thomson effect”, which explains the rate of heat absorption and release in a conductor materials ( $\dot{Q} = -\kappa \Delta^2 T$ ) as a function of temperature gradient ( $\Delta T$ ) and electrical current density ( $J$ ). The Thomson effect is illustrated in Figure 3. The mathematical expression of Thomson effect is derived in the equation below (Saini *et al.*, 2021).

$$\dot{Q} = \frac{J^2}{\sigma} - J \left( \frac{T \partial \alpha}{\partial T} \right) \Delta T \quad (4)$$

Here, the term  $\frac{T \partial \alpha}{\partial T}$  defined as “Thomson coefficient”  $\mu$ . Consequently, the Thomson coefficient can be derived as shown in equation (5).

$$\mu = \frac{T \partial \alpha}{\partial T} \quad (5)$$

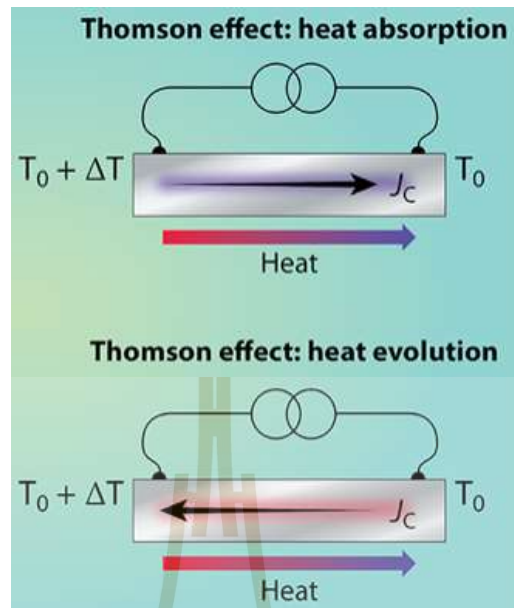


**Figure 3** Illustration to demonstrate Thomson effect (Morrison and Dejene, 2020).

The key coupled transport equations of electrons and heat, based on thermodynamic theory, were derived using the Boltzmann transport equation, diffusion approximations, the Fermi–Dirac distribution, Ohm’s law, Fourier law, and Onsager’s reciprocal relations. This derivation process of the couple transport equations follows the methodology outlined in the book of “Nanoscale energy transport and conversion” by Gang Chen (Chen, 2005). The transport equation originates from the generalization of the continuity equation. When applied with the conservation of mass, this is referred to as “convection–diffusion equation” ( $\frac{\partial c}{\partial t} + \nabla \cdot j = S$ ) such as Boltzmann transport equation. Then Boltzmann transport equation is used to describe changes in microscopy quantities, such as electrons and heat, within a thermodynamic system. The Boltzmann transport equation is shown in equation below (6) (Crawford, 2014).

$$\frac{\partial f}{\partial t} + v \cdot \nabla_r f + F \cdot \Delta_p f = \frac{\partial f}{\partial t} \Big|_{\text{collid}} + s(r, p, t) \quad (6)$$

Where;

$f$  is a scalar quantity in the control volume.

$\frac{\partial f}{\partial t}$  is the time dependent variant term of quantity  $f$  in the control volume.

$\frac{\partial f}{\partial t}|_{collid}$  is the time dependent collision term when  $f$  is a quantity of particles

$v \cdot \nabla_r f + F \cdot \Delta_p f$  is net balance quantity that enters or exits and the control volume.

$r$  is real space.

$p$  is momentum space.

$F$  is force that influential in changing momentum space.

$s(r, p, t)$  is source term that represent amount of scalar quantity increase and decrease.

Due to the unidentified or absent source of the scalar quantity “ $s(r, p, t) = 0$ ” and the relaxation time approximation ( $\tau$ ,  $\frac{1}{\tau} = \sum_i \frac{1}{\tau_i}$ ) is applied to obtain

$\frac{\partial f}{\partial t}|_{collid} = \frac{f - f_0}{\tau}$ , as shown in equation (7).

$$\frac{\partial f}{\partial t} + v \cdot \nabla_r f + F \cdot \Delta_p f = \frac{f - f_0}{\tau} \quad (7)$$

Where;

$f_0$  is a symmetric in momentum with average velocity is zero (Indeed,  $f_0$  is a distribution function).

$\tau$  is the relaxation time approximation that is inverse of all scattering process of particles in the control volume as  $\frac{1}{\tau} = \sum_i \frac{1}{\tau_i}$ .

Then, the diffusion approximation is used to determine the appropriate distribution function for  $f$ . A deviation function  $g$  is defined by applying perturbation method for  $f$ . The function  $g$  is shown in equation (8).

$$g = f - f_0 \quad (8)$$

Then, substituted equation (8) in equation (7).

$$\frac{\partial f_0}{\partial t} + \frac{\partial g}{\partial t} + v \cdot \nabla_r f_0 + v \cdot \nabla_r g + F \cdot \Delta_p f_0 + F \cdot \Delta_p g = \frac{g}{\tau} \quad (9)$$

Due to the process stay in “steady state”, the variable  $f_0$  is unchanged in time,  $\frac{\partial g}{\partial t}$  and

$\nabla_r g$  too smaller than  $f$  and  $f_0$  (diffusion law). Therefore, the equation (9) is changed.

$$g = \tau(v \cdot \nabla_r f_0 + F \cdot \Delta_p f_0) \quad (10)$$

Substituted equation (10) in equation (8).

$$f = f_0 + \tau(v \cdot \nabla_r f_0 + F \cdot \Delta_p f_0) \quad (11)$$

The distribution function of  $f$  can be extended using Fermi–Dirac distribution, which applied to fermions/particles with half–integer spin, including electrons. The Fermi–Dirac distribution is demonstrated equation (12).

$$f_0 = \frac{1}{e^{\frac{(E-E_f)}{k_B T}} + 1} \quad (12)$$

For electrons, the energy of state  $E$  is defined as  $E = E_c + E_f$  where  $E_c$  is the conduction energy and  $E_f$  is Femi level energy (the absolute different energy above the conduction energy). Then, to define the force acting which interacted on the flow of electrons in the presence of an electric field, Ohm’s law and the Wiedemann–Franz law are applied.

$$F = -e\bar{E} \quad (13)$$

$$-e\bar{E} = e\nabla\Phi \quad (14)$$

Where;

$F$  is force which interacted on electrons

$e$  is electrons charge

$\bar{E}$  is electric field ( $\bar{E} = \frac{\partial V_{external}}{\partial r}$ )

$\Phi$  is electrical potential

Then, the energy of electron conduction energy and Femi–level energy are derived in equation (15) and (16).

$$E = E_c + E_f \quad (15)$$

$$E = E_c + \frac{1}{2} m^* (v_x^2 + v_y^2 + v_z^2) \quad (16)$$

Where;

$m^*$  is electrons mass.

$v_x, v_y, v_z$  is electrons velocity on xyz axes.

When consider the electrons and heat transport direction along  $x$ –axis, consequently  $E$  and  $T$  dependents on  $x$ –axis. Thus, gradient of Fermi–Dirac distribution along  $x$ –axis ( $\nabla_r f_0$ ) are derived in equation (24).

$$\frac{\partial f_0}{\partial x} = \frac{\partial f_0}{\partial E} \frac{\partial E}{\partial x} + \frac{\partial f_0}{\partial E} \frac{\partial E}{\partial T} \frac{\partial T}{\partial x} \quad (17)$$

Defining;

$$y = \frac{1}{e^{\frac{E-E_f}{kT}} + 1} \quad (18)$$

$$\frac{\partial f_0}{\partial T} = \frac{\partial f_0}{\partial y} \left( -\frac{E - E_f}{kT^2} \right) \quad (19)$$

$$\frac{\partial f_0}{\partial E} = \frac{\partial f_0}{\partial y} \left( \frac{1}{kT} \right) \quad (20)$$

$$\frac{\partial f_0}{\partial E_f} = \frac{\partial f_0}{\partial y} \left( -\frac{1}{kT} \right) \quad (21)$$

$$\frac{\partial E}{\partial T} = \frac{E - E_f}{T} \quad (22)$$

$$\frac{\partial f_0}{\partial E} = -\frac{\partial f_0}{\partial E_f} \quad (23)$$

Thus;

$$\frac{\partial f_0}{\partial x} = -\frac{\partial f_0}{\partial E} \frac{\partial E_f}{\partial x} + \frac{E - E_f}{T} \frac{\partial f_0}{\partial E} \frac{\partial T}{\partial x} \quad (24)$$

The current density of the electron is calculated by summing all the charges, velocities and distribution of electron states as shown in equation (25)

$$J_e = \frac{1}{V} \sum_{k_x} \sum_{k_y} \sum_{k_z} (-e) v_x f \quad (25)$$

Where;

$V$  is volume per all of state electrons  $V = \frac{1}{L^3}$ .

$J_e$  is current density or current flux of electrons.

$k$  is direction axes of electrons wave.

The summation equation is transformed into its integral form, following Fourier's law, using spherical coordinates, as shown in equation (27).

$$J_e = -\frac{1}{(L)^3} \int_{k_x=-\infty}^{\infty} \int_{k_y=-\infty}^{\infty} \int_{k_z=-\infty}^{\infty} e v_x f \frac{dk_x}{L} \frac{dk_y}{L} \frac{dk_z}{L} \quad (26)$$

$$J_e = - \int_{k_x=-\infty}^{\infty} \int_{k_y=-\infty}^{\infty} \int_{k_z=-\infty}^{\infty} e v_x f \frac{1}{(2\pi)^3} dk_x dk_y dk_z \quad (27)$$

Defining;

$$dk_x dk_y dk_z = k^2 \sin \theta d\theta d\phi dk \quad (28)$$

$$V_1 = \left( \frac{2\pi}{L} \right)^3 \quad (29)$$

$$dN = \frac{4\pi k^2 dk}{V_1} = \frac{V k^2 dk}{2\pi} \quad (30)$$

$$dN = \frac{4\pi k^2 dk}{V_1} = \frac{Vk^2 dk}{2\pi^2} \quad (31)$$

$$D(E) = \frac{dN}{VdE} = \frac{k^2 dk}{2\pi^2 dE} \quad (32)$$

Thus;

$$D(E)dE = \frac{k^2 dk}{2\pi^2} \quad (33)$$

$$\frac{D(E)}{4\pi} dE = \frac{k^2 dk}{(2\pi)^3} \quad (34)$$

Where;

$\theta, \varphi$  is spherical coordinate vertical and horizontal angles.

$dN$  is different of number states ( $N$ ) between spherical shield of  $k$  and  $k + dk$  per unit volume of a state.

$D(E)$  is density state of electrons.

From equation (28) and (34), the equation (27) can be written as equation (35).

$$J_e = -\int_0^\infty \int_0^{2\pi} \int_0^\pi e(v \cos \theta) f \frac{D(E)}{4\pi} \sin \theta d\theta d\varphi dE \quad (35)$$

Then substituted equation (11) ( $f$  term) and (24) ( $F$  term) to equation (35).

$$J_e = -\int_0^\infty \int_0^{2\pi} \int_0^\pi e(v \cos \theta) \left( f_0 + \tau \left( v \cos \theta \frac{\partial f_0}{\partial x} + e\bar{E} \frac{dE}{dp} \frac{df_0}{dE} \right) \right) \frac{D(E)}{4\pi} \sin \theta d\theta d\varphi dE \quad (36)$$

From equation (15) and defining  $dp = m dv$ .

$$J_e = -\int_0^\infty \int_0^{2\pi} \int_0^\pi e(v \cos \theta) \left( f_0 + \tau v \cos \theta \left( \frac{\partial f_0}{\partial x} + e\bar{E} \frac{df_0}{dE} \right) \right) \frac{D(E)}{4\pi} \sin \theta d\theta d\varphi dE \quad (37)$$

$$J_e = -e \int_0^\infty \int_0^{2\pi} \int_0^\pi \left\{ v \cos \theta \sin \theta f_0 + \tau v^2 \cos^2 \theta \sin \theta \left( \frac{\partial f_0}{\partial x} + e\bar{E} \frac{df_0}{dE} \right) \right\} \frac{D(E)}{4\pi} d\theta d\varphi dE \quad (38)$$

Then, integrated  $\theta$  term.

$$J_e = -e \int_0^\infty \int_0^{2\pi} \left\{ v f_0 \left( -\frac{\cos^2 \theta}{2} \right) \Big|_0^\pi + \tau v^2 \left( \frac{\partial f_0}{\partial x} + e\bar{E} \frac{df_0}{dE} \right) \left( -\frac{\cos^3 \theta}{3} \right) \Big|_0^\pi \right\} \frac{D(E)}{4\pi} d\varphi dE \quad (39)$$

$$J_e = -\frac{e}{6\pi} \int_0^\infty \int_0^{2\pi} \tau v^2 \left( \frac{\partial f_0}{\partial x} + e\bar{E} \frac{df_0}{dE} \right) D(E) d\varphi dE \quad (40)$$

Then, integrated  $\varphi$  term.

$$J_e = -\frac{e}{6\pi} \int_0^\infty \tau v^2 \left( \frac{\partial f_0}{\partial x} + e\bar{E} \frac{df_0}{dE} \right) D(E) (\varphi) \Big|_0^{2\pi} dE \quad (40)$$

$$J_e = -\frac{e}{3} \int_0^\infty \tau v^2 \left( \frac{\partial f_0}{\partial x} + e\bar{E} \frac{df_0}{dE} \right) D(E) dE \quad (41)$$

Then, substituted equation (24) in the equation (41).

$$J_e = -\frac{e}{3} \int_0^{\infty} \tau v^2 \left( -\frac{\partial f_0}{\partial E} \frac{\partial E_f}{\partial x} + \frac{E - E_f}{T} \frac{\partial f_0}{\partial E} \frac{\partial T}{\partial x} + e\bar{E} \frac{df_0}{dE} \right) D(E) dE \quad (42)$$

$$J_e = -\frac{e}{3} \int_0^{\infty} \tau v^2 \left( -\frac{\partial f_0}{\partial E} \frac{\partial E_f}{\partial x} + \frac{E - E_f}{T} \frac{\partial f_0}{\partial E} \frac{\partial T}{\partial x} + e\bar{E} \frac{df_0}{dE} \right) D(E) dE \quad (43)$$

Separated the equation (43) to couple term of temperature gradient and potential gradient as equation (44).

$$J_e = \frac{e}{3} \int_0^{\infty} \tau v^2 \frac{\partial f_0}{\partial E} D(E) dE \left( \frac{\partial E_f}{\partial x} - e\bar{E} \right) + \frac{e}{3T} \int_0^{\infty} \tau v^2 (E - E_f) \frac{\partial f_0}{\partial E} D(E) dE \left( -\frac{\partial T}{\partial x} \right) \quad (44)$$

Due to electrochemical potential is defined as equation (45).

$$\Phi = \frac{E_f}{q} - V_{external} = -\left( \frac{E_f}{e} - V_{external} \right) \quad (45)$$

The current density of the electron can rewrite as equation (47).

$$J_e = \frac{e^2}{3} \int_0^{\infty} \tau v^2 \frac{\partial f_0}{\partial E} D(E) dE \left( -\frac{\partial \Phi}{\partial x} \right) + \frac{e}{3T} \int_0^{\infty} \tau v^2 (E - E_f) \frac{\partial f_0}{\partial E} D(E) dE \frac{\partial T}{\partial x} \quad (46)$$

$$J_e = L_{11} \left( -\frac{\partial \Phi}{\partial x} \right) + L_{12} \left( -\frac{\partial T}{\partial x} \right) \quad (47)$$

Defining;

$$L_{11} = \frac{e^2}{3} \int_0^{\infty} \tau v^2 \frac{\partial f_0}{\partial E} D(E) dE \quad (48)$$

$$L_{12} = \frac{e}{3T} \int_0^{\infty} \tau v^2 (E - E_f) \frac{\partial f_0}{\partial E} D(E) dE \quad (49)$$

Defining;

$$\sigma = L_{11} = \frac{e^2}{3} \int_0^{\infty} \tau v^2 \frac{\partial f_0}{\partial E} D(E) dE \quad (50)$$

Where;

$\sigma$  is electrical conductivity.

The Seebeck coefficient is evaluated using equation (47) when the system is in a steady state as  $J_e = 0$  (open circuit condition).

$$0 = L_{11} \left( -\frac{\partial \Phi}{\partial x} \right) + L_{12} \left( -\frac{\partial T}{\partial x} \right) \quad (51)$$

$$\alpha = -\frac{\partial \Phi / \partial x}{\partial T / \partial x} = \frac{L_{12}}{L_{11}} \quad (52)$$

The electron current transport equation can be rewritten to incorporate electrical conductivity and Seebeck coefficient along equation (47), (50) and (52) as equation (53).

$$J_e = \sigma \left( -\frac{\partial \Phi}{\partial x} \right) - \alpha \sigma \frac{\partial T}{\partial x} \quad (53)$$

For  $r$  space;

$$J_e = \sigma(-\Delta\Phi) - \alpha\sigma\Delta T \quad (54)$$

Based on equations (50) and (52), the equation can be used to predict electrical conductivity and Seebeck coefficient of thermoelectric materials.

The equation described electron flow along Boltzmann transport equation and the Fermi-Dirac distribution. Similarly, heat flow is derived using the same process as for the electron current density. The heat flow is derived from the first law of thermodynamic, as shown in equation (55).

$$dU = dQ + E_f dn \quad (55)$$

$$dQ = dU - E_f dn \quad (56)$$

$$dJ_Q = dJ_U - dJ_n \quad (57)$$

Where;

$U$  is energy of system

$Q$  is heat of system

$n$  is number of particles

$J_Q$  is heat flux

$J_U$  is energy flux

$J_n$  is particles flux

The energy density can be calculated by integrating of all energy  $E$  along x-axis direction, as shown in equation (58).

$$J_U = \int_{-\infty}^{\infty} \int_{-\infty}^{\infty} \int_{-\infty}^{\infty} E v_x f dv_x dv_y dv_z \quad (58)$$

The particle density can be calculated by integrating of all energy  $E_f$  along x-axis direction, as shown in equation equation (59).

$$J_n = \int_{-\infty}^{\infty} \int_{-\infty}^{\infty} \int_{-\infty}^{\infty} E_f v_x f dv_x dv_y dv_z \quad (59)$$

Thus, the heat density consists of energy and particle density integration is shown in equation (60).

$$J_Q = \int_{-\infty}^{\infty} \int_{-\infty}^{\infty} \int_{-\infty}^{\infty} (E - E_f) v_x f dv_x dv_y dv_z \quad (60)$$

The heat density for thermoelectric system is determined by the electron carrier, the distribution function  $J$  and Fermi–Dirac distribution. Consequently, equation (60) is derived using equation (11) to (46). The heat density  $J_Q$  is expressed in equation (61).

$$J_Q = L_{21} \left( -\frac{\partial \Phi}{\partial x} \right) + L_{22} \left( -\frac{\partial T}{\partial x} \right) \quad (61)$$

Defining;

$$L_{21} = \frac{e}{3} \int_0^{\infty} v^2 (E - E_f) \frac{\partial f_0}{\partial E} D(E) dE \quad (62)$$

$$L_{22} = -\frac{e}{3T} \int_0^{\infty} v^2 (E - E_f)^2 \frac{\partial f_0}{\partial E} D(E) dE \quad (63)$$

The relation between  $L_{12}$  and  $L_{22}$  connection originally described by Lars Onsager, known as the “Onsager relations”.

$$L_{21} = TL_{12} \quad (64)$$

When the chemical potential term is eliminated, the current density and heat density equation reveal the correlation of heat flow, as shown in equation (65).

$$J_Q = \frac{L_{21}}{L_{12}} J_e + \left( L_{22} - \frac{L_{12}L_{21}}{L_{11}} \right) \left( -\frac{\partial T}{\partial x} \right) \quad (65)$$

Defining;

$$\Pi = \frac{L_{21}}{L_{11}} \quad (66)$$

$$k = \left( L_{22} - \frac{L_{12}L_{21}}{L_{11}} \right) \quad (67)$$

Where;

$\kappa$  is thermal conductivity.

The heat transport equation due to electron carrier can be rewritten to include thermal conductivity and the Peltier coefficient, as show in equation (65), (66) and (67), and is expressed in equation (68).

$$J_Q = \Pi J_e - \kappa \left( \frac{\partial T}{\partial x} \right) \quad (68)$$

For  $r$  space;

$$J_e = \Pi J_e - \kappa \Delta T \quad (69)$$

Based on equation (66) and (67), the Peltier coefficient and thermal conductivity of thermoelectric materials can be calculated. The coupled transport processes of the thermoelectric effect and the associated coefficient parameters have been derived and defined. The efficiency of thermoelectric materials and devices was then

calculated to optimize the maximal performance of electrical generators and cooling systems. Thomson effect (4) was considered in determining the maximal performance of thermoelectric materials, using the Domenicali equation (Thomson relations  $\dot{Q} = -\kappa\Delta^2T$ ) (Rowe, 2018; Zlatic and Monnier, 2014).

$$\dot{Q} = -\kappa\Delta^2T = \frac{J^2}{\sigma} - J\left(\frac{T\partial\alpha}{\partial T}\right)\Delta T \quad (70)$$

It is assumed that heat transfer occurs along the x-axis, with the cold side of the materials at  $x_0 = 0$ ,  $T_0$  and the hot side end at  $x_1 = l$ ,  $T_1$ . As a result, the term of  $J\left(\frac{T\partial\alpha}{\partial T}\right)\Delta T$  is eliminated because  $\alpha$  don't change within a material. The equation (70) can be rewrite as equation (71).

$$-\kappa \frac{\partial^2 T}{\partial^2 x} = \frac{J^2}{\sigma} \quad (71)$$

$$-\int \kappa \frac{\partial^2 T}{\partial^2 x} \partial x = \int \frac{J^2}{\sigma} \partial x \quad (72)$$

$$-\kappa \frac{\partial T}{\partial x} = \frac{J^2}{\sigma} x + F \quad (73)$$

$$-\int \kappa \frac{\partial T}{\partial x} \partial x = \int \left( \frac{J^2}{\sigma} x + F \right) \partial x \quad (74)$$

$$-\kappa T(x) = \frac{J^2 x^2}{2\sigma} + Fx + G \quad (75)$$

At condition  $x_0 = 0$ ,  $T_0$ , the parameter G is shown in equation (76).

$$G = -\kappa T_0 \quad (76)$$

Thus;

$$-\kappa T(x) = \frac{J^2 x^2}{2\sigma} + Fx - \kappa T_0 \quad (77)$$

At condition  $x_1 = l$ ,  $T_1$ .the parameter F is shown in equation (78).

$$F = -\frac{J^2 l}{2\sigma} - \frac{\kappa}{l} (T_1 - T_0) \quad (78)$$

Thus;

$$-\kappa T(x) = \frac{J^2 x^2}{2\sigma} - \frac{J^2 lx}{2\sigma} - \frac{\kappa}{l} (T_1 - T_0)x - \kappa T_0 \quad (79)$$

Defining;

$$K = \frac{\kappa A}{l} \quad (80)$$

$$R = \frac{l}{\sigma A} \quad (81)$$

$$J = \frac{I}{A} \quad (82)$$

Where;

$F$  is thermal conductance

$G$  is electrical resistance

$K$  is thermos conductance

$R$  is electrical resistance

$A$  is surface area of the materials

$l$  is length of the materials

Substituted equation (80), (81) and (82) in equation (79);

$$T(x) = -\frac{I^2 R x^2}{2Kl^2} + \frac{I^2 R x}{2Kl} + \left(\frac{T_1 - T_0}{l}\right)x + T_0 \quad (83)$$

Then;

$$\frac{\partial T(x)}{\partial x} = \frac{RI^2}{2Kl} \left(1 - \frac{2x}{l}\right) + \frac{T_1 - T_0}{l} \quad (84)$$

Substituted equation (83) in equation (68) to get heat transport.

$$J = \Pi J - \kappa \Delta T \quad (85)$$

$$J_e = T \alpha J_e - \kappa \Delta T \quad (86)$$

At condition heat transfer along in x-axis,  $x_0 = 0$ ,  $T_0$ , the equation (86) is changed.

$$Q_0 = \alpha I T_0 - K(T_1 - T_0) - \frac{RI^2}{2} \quad (87)$$

Defining;

$$J_e = \frac{Q}{A} \quad (88)$$

The maximal heat transfer depended on current  $I$ , Then optimal current that yields maximal heat transfer is determined by taking the derivative of equation (87) with  $dI$ .

$$\frac{\partial Q_0}{\partial I} = \frac{\partial \left( \alpha I T_0 - K(T_1 - T_0) - \frac{RI^2}{2} \right)}{\partial I} \quad (89)$$

$$0 = \alpha T_0 - RI \quad (90)$$

$$I_{op} = \frac{\alpha T_0}{R} \quad (91)$$

Substituted  $I_{op}$  in equation (87).

$$Q_0 = \frac{\alpha^2 T_0^2}{2R} - K(T_1 - T_0) \quad (92)$$

Under this condition, the heat source will transfer until reach  $Q_0 = 0$ . The maximum possible different temperature  $(T_1 - T_0)$  at the other end of a materials is shown in equation (95).

$$(T_1 - T_0)_{\max} = \frac{\alpha^2}{2RK} T_0^2 \quad (93)$$

$$(T_1 - T_0)_{\max} = \frac{\alpha^2 \sigma}{2\kappa} T_0^2 \quad (94)$$

$$(T_1 - T_0)_{\max} = Z T_0^2 \quad (95)$$

Defining;

$$Z = \frac{\sigma \alpha^2}{\kappa} \quad (96)$$

Where;

$Z$  is the figure of merit.

The figure of merit is a widely used parameter to indicate the performance of thermoelectric materials.

### 2.1.3 Effects in a magnetic field

Normally, electrical charges are horizontal forced as move through in magnetic field. As a result, the properties of thermoelectric effects can change when a magnetic field is applied. The influence of magnetic field on thermoelectric effects is known as “Thermogalvanomagnetic effects”, which impact the performance of thermoelectric module. The thermogalvanomagnetic effects is illustrated in Figure 4. The variation in Seebeck coefficient when the magnetic field is reversed is referred to as the “Umkehr effect”. The Umkehr effect is deployed by equation (97).

$$\Pi(\mathbf{B}) = \mathbf{T} \alpha(-\mathbf{B}) \quad (97)$$

Where;

$\mathbf{B}$  is a magnetic field

When a magnetic field is applied to a system, an electric field will appear perpendicular to both electrical current and magnetic field. This phenomenon is known as “Hall effect”. However, the transverse voltage that arises in a magnetic field due to a longitudinal temperature gradient or heat flow is called “Nernst effect”. Unlike the Hall effect, the Nernst effect is independent of whether the charge carriers are positive or negative. The Nernst coefficient ( $N$ ) is defined by equation (98).

$$|N| = \frac{dV/dy}{B_z dT/dx} \quad (98)$$

Where;

N is Nernst coefficient.

$dV/dy$  is a derivative of transverse electric field.

x, y and z are Cartesian coordinate system.

Moreover, Ettingshausen refers to the generation of a transverse temperature gradient in the presence of a transverse magnetic field and a longitudinal electric current. The Ettingshausen coefficient ( $E_p$ ) is defined by equation (99).

$$E_p = \frac{dT/dy}{i_x B_z} \quad (99)$$

Where;

$E_p$  is Ettingshausen coefficient.

$dT/dy$  is a derivative of temperature.

The correlation between Ettingshausen effect and Nernst effect is represented in equation (100).

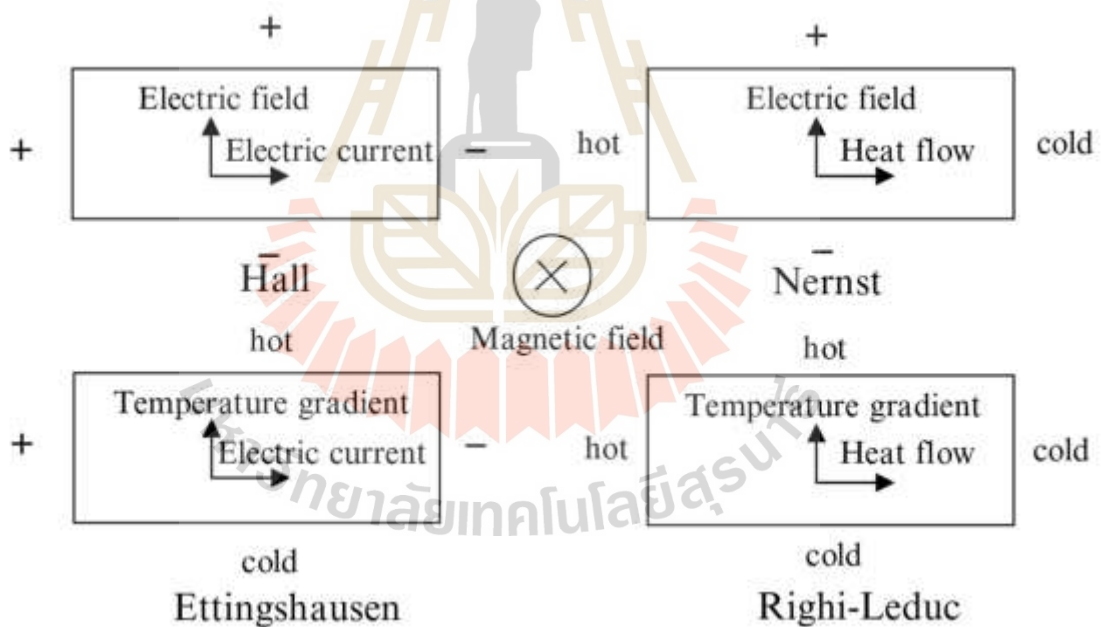


**Figure 4** The thermogalvanomagnetic effects with different directions of involved parameters (Goldsmid, 2010).

$$E_p \kappa = NT \quad (100)$$

The final thermogalvanomagnetic effects is “Righi-Leduc effect” which refers to transverse temperature gradient generated by perpendicular heat flow. The Righi-Leduc coefficient ( $R_s$ ) is defined by equation (101).

$$R_s = \frac{dT/dy}{B_z dT/dx} \quad (101)$$

Where;

$R_s$  is Righi–Leduc coefficient.

#### 2.1.4 Transport effects

The thermoelectric phenomena are reversible process according to thermodynamics principles, but thermoelectric parameters, such as electrical resistance and thermal conduction, are irreversible. However, reversibility can be expressed in terms of the derivatives of Seebeck coefficient, thermal conduction, and electrical resistances. The electrical current depend on electrical conductivity, electrical voltage and the ratios of length to cross-sectional area, as shown in equation (102).

$$I = \frac{\sigma VA}{L} \quad (102)$$

Where;

A is cross-sectional area.

L is length

V is applied voltage

Moreover, the thermal conductivity is defined by the equation (103).

$$q = \frac{\kappa \Delta T}{L} \quad (103)$$

Where;

q is rate of heat flow.

The thermoelectric coefficients, along with electrical and thermal conductivities, are considered key transport properties of a materials. These properties are typically temperature-dependent, and the variation temperature has a significant impact on thermoelectric generation.

### 2.1.5 Thermoelectric refrigerators

The performance of a refrigerators involves applying an external electrical voltage to the end of a thermoelectric couple subsequent occur heat source ( $T_h$ ) and cold source or heat pump ( $T_c$ ). A thermoelectric refrigerator consisting of p-n couple is demonstrated in Figure 5.

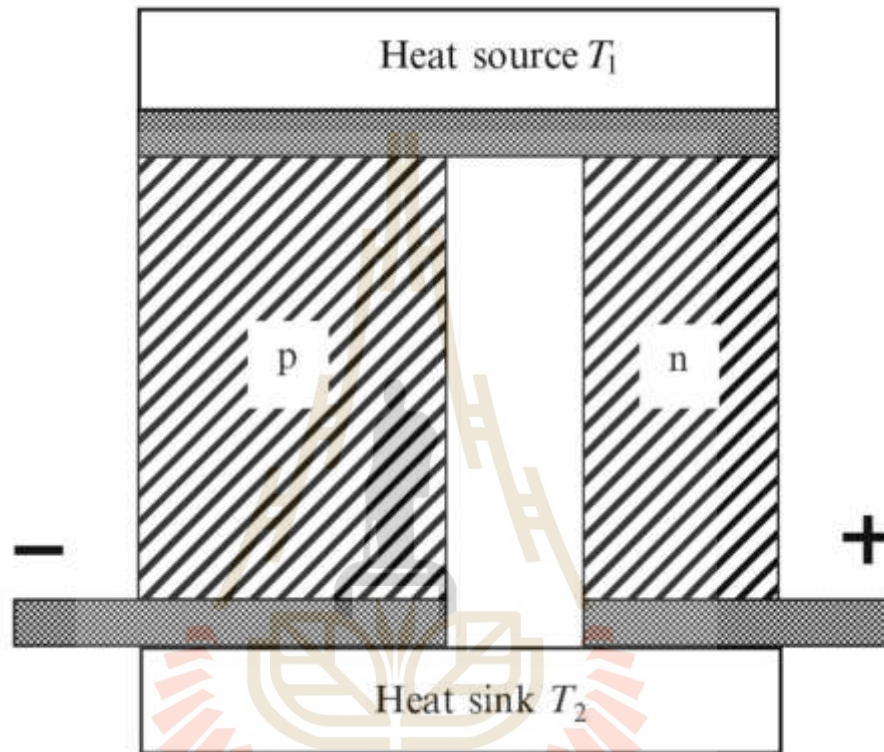


**Figure 5** Illustration of model a couple p-n pair refrigerator (Goldsmid, 2010).

When an electrical current is applied to thermoelectric refrigerator, or in the case of Peltier cooling, subsequent heat flow through the p-n couple  $(\alpha_p - \alpha_n)IT_h$ , which using Kelvin relation in equation (3) eliminate Peltier coefficient in equation (2). Heat conduction creates resistance to the heat pump as  $(T_h - T_c)(\kappa_p + \kappa_n)$ . The heat pump is also opposed by half of Joule heating, similar to a Carnot cycle as  $I^2(R_p + R_n)/2$ . The rate of the heat pump can be express in equation (104).

$$q = (\alpha_p - \alpha_n)IT_h - (T_h - T_c)(\kappa_p + \kappa_n) - \frac{I^2(R_p + R_n)}{2} \quad (104)$$

The rate of electrical power usage also expresses in equation (105).

$$P_{out} = (\alpha_p - \alpha_n)I(T_h - T_c) - I^2(R_p + R_n) \quad (105)$$

Where;

$P_{out}$  is electrical power.

Therefore, the performance of a refrigerator, measured as the coefficient of performance (COP), can be determined by dividing the heat flow described in equation (104) by electrical power usage give in equation (105). The COP is represented in equation (106).

$$\phi = \frac{(\alpha_p - \alpha_n)IT_h - (T_h - T_c)(\kappa_p + \kappa_n) - \frac{I^2(R_p + R_n)}{2}}{(\alpha_p - \alpha_n)I(T_h - T_c) - I^2(R_p + R_n)} \quad (106)$$

Where;

$\phi$  is coefficient of performance (COP).

### 2.1.6 Thermoelectric generators

Thermoelectric generators, based on Seebeck effect, are used to directly convert heat into electrical current. These thermoelectric generators operate using a model of a p-n couple generator, as shown in Figure 6. The couple p-n generator is connected to a load resistance  $R_L$ , generating electricity through the temperature difference between the two end of the generator. The generated electrical power is delivered to the load resistance, and the efficiency  $\eta$  is calculated as the ratio of the electrical output power to the rate of heat drawn. The heat drawn is flowing of heat due to thermal conduction along the p-n couple generator. Total rate of heat flow is expressed in equation (107).

$$q = (\alpha_p - \alpha_n)IT_h + (T_h - T_c)(\kappa_p + \kappa_n) \quad (107)$$

While the electromotive force (EMF) give electrical current following equation (108).

$$I = \frac{(\alpha_p - \alpha_n)(T_h - T_c)}{R_p + R_n + R_L} \quad (108)$$

Then, the electrical output power is;

$$P_{out} = I^2 R_L = \left[ \frac{(\alpha_p - \alpha_n)(T_h - T_c)}{R_p + R_n + R_L} \right]^2 R_L \quad (109)$$

The efficiency  $\eta$  is the ratio of electrical output power to the rate of heat drawn, equation (109) divide by equation (107).

$$\eta = \frac{\left[ \frac{(\alpha_p - \alpha_n)(T_h - T_c)}{R_p + R_n + R_L} \right]^2 R_L}{(\alpha_p - \alpha_n) I T_h + (T_h - T_c)(\kappa_p + \kappa_n)} \quad (110)$$

When;

$$M = \frac{R_L}{R_p + R_n} \quad (111)$$

Finally, the efficiency  $\eta$  can be deploy by equation (112).

$$\eta = \frac{(T_h - T_c)(M - 1)}{T_h \left( M + \frac{T_c}{T_h} \right)} \quad (112)$$

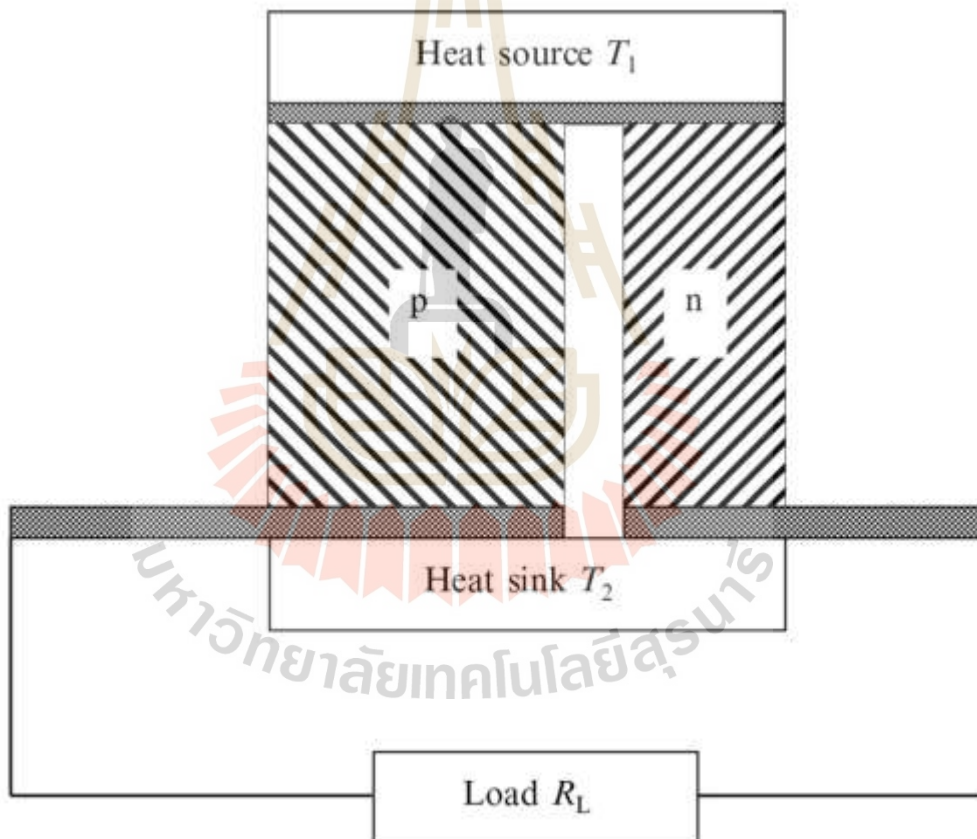


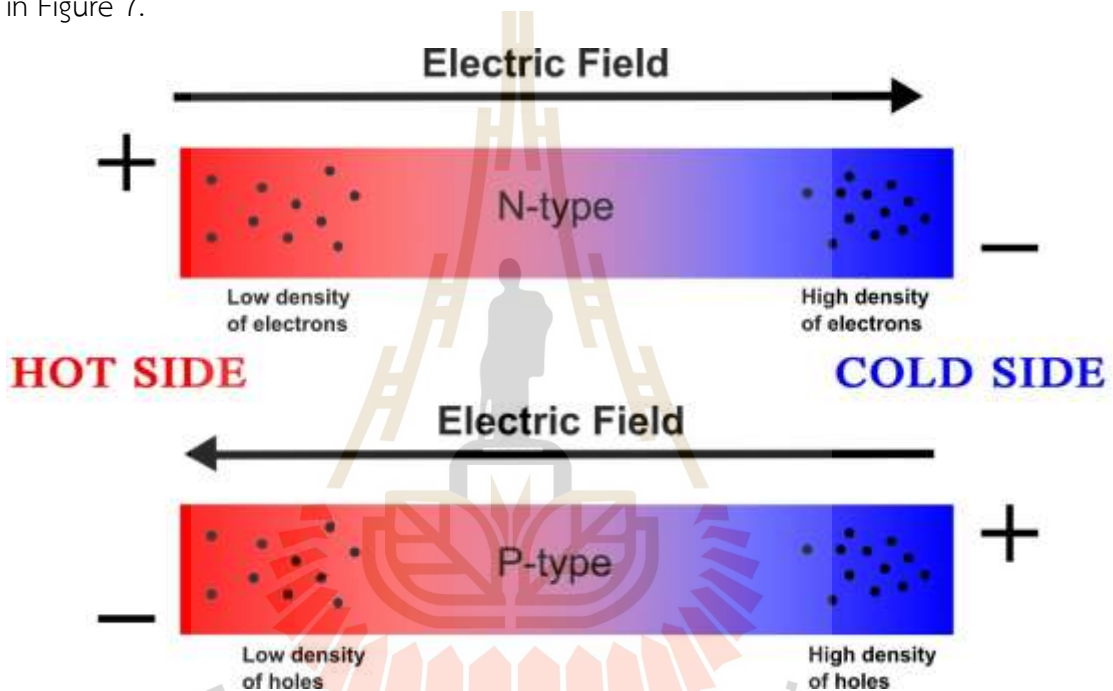
Figure 6 Illustration of model a couple p-n generator (Goldsmid, 2010).

## 2.2 Thermoelectric materials

### 2.2.1 Thermoelectric materials

Normally, thermoelectric materials are typically classified into n-type and p-type materials, based on its charge carrier and ability to generate heat and cold at

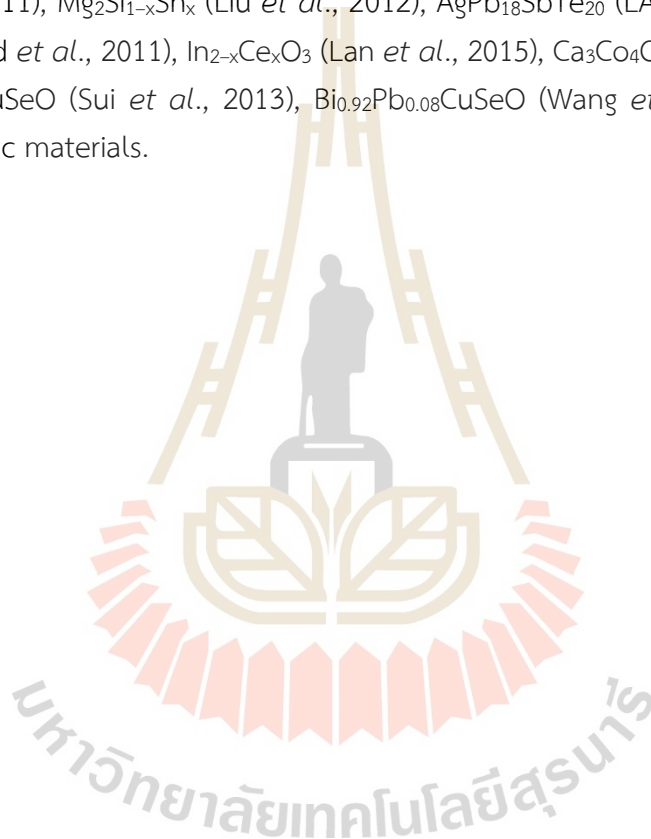
the couple end of the materials. For n-type thermoelectric materials, there is a temperature difference between the two ends, an electric field is induced, with the direction from the hot side (+) to the cold side (-) and subsequent in a high density of electron at cold side and a low density of electrons at hot side. Conversely, in p-type thermoelectric materials, the electric field is induced in the opposite direction, from the cold side (+) to the hot side (-) and subsequent in a high density of holes (low density of electron) at cold side and a low density of hole at hot side (high density of electrons). The behaviour of n-type and p-type of thermoelectric materials is shown in Figure 7.



**Figure 7** Illumination of n-type and p-type of thermoelectric materials behaviour (Nabilasamiron, 2012).

The optimal thermoelectric materials for converting heat into electrical current at various operating temperature are evaluated based on thermoelectric properties, such as Seebeck coefficient, thermal conductivity, electrical conductivity, as well as the dimensionless figure of merit ( $ZT$ ) described in equation (96). According to Marta Rull's report, a summary of the performance of p-type and n-type of thermoelectric materials across different operating temperatures is shown in Figure 8 (Rull-Bravo *et al.*, 2015). Moreover, Table 1 lists various thermoelectric materials, operating temperatures, power factor, synthesis method and  $ZT$ . The excellent thermoelectric materials, characterized by a high  $ZT$  ( $>1$ ) and great power factor, i. e.,  $\text{Bi}_x\text{Sb}_{2-x}\text{Te}_3$ ,  $\beta\text{-Zn}_4\text{Sb}_3$ ,  $\beta\text{-Cu}_4\text{Se}$ ,  $(\text{GeTe})_{0.85}(\text{ASbTe}_2)_{0.15}$ ,  $\text{Na-Pb-Sb-Te}$ ,  $\text{PbTe-rTe-Na}$ ,  $\text{Yb}_{14}\text{Mn}_{1-x}\text{Al}_x\text{Sb}_{11}$ ,

$\text{Bi}_2\text{Te}_{3-x}\text{Se}_x$ ,  $\text{Mg}_2\text{Si-Mg}_2\text{Sn}$ ,  $\text{AgPb}_m\text{SbTe}_{2+m}$ ,  $\text{PbTe-Ag}_2\text{Te-La}_{0.08}\text{La}_{0.05}\text{Yb}$ , P-doped  $\text{SiGe}$ ,  $\text{Bi}_{0.92}\text{Pb}_{0.08}\text{CuSeO}$ ,  $\text{Bi}_{0.875}\text{Ba}_{0.125}\text{CuSeO}$ ,  $\text{SnS}$ ,  $\text{SnSe}$  and  $\text{Ag}_2\text{Se}$ . However, in light of the global energy crisis and the motivation discussed in the chapter I to recycle industrial waste heat, the most suitable thermoelectric materials for temperatures corresponding to waste heat about 200–400 °C (Minea, 2007) include  $\beta\text{-Zn}_4\text{Sb}_3$  (Caillat *et al.*, 1997),  $\text{SnSe}$  (Gainza *et al.*, 2020),  $\text{Na-Pb-Sb-Te}$  (salt) (Poudeu *et al.*, 2006),  $\text{SnS}$  (Asfandiyar *et al.*, 2017),  $\text{PbTe-SrTe-Na}$  (Biswas *et al.*, 2012),  $(\text{GeTe})_{0.85}(\text{AgSbTe}_2)_{0.15} + 2\%\text{Dy}$  (Levin *et al.*, 2012) in p-type thermoelectric materials, and  $\text{Ba}_{0.08}\text{La}_{0.05}\text{Yb}_{0.04}\text{Co}_4\text{Sb}_{12}$  (skutterudite) (Shi *et al.*, 2011),  $\text{Mg}_2\text{Si}_{1-x}\text{Sn}_x$  (Liu *et al.*, 2012),  $\text{AgPb}_{18}\text{SbTe}_{20}$  (LAST) (Hsu *et al.*, 2004),  $\text{ZnAl}_2\text{O}_4$  (Jood *et al.*, 2011),  $\text{In}_{2-x}\text{Ce}_x\text{O}_3$  (Lan *et al.*, 2015),  $\text{Ca}_3\text{Co}_4\text{O}_9$  (Zhang *et al.*, 2020),  $\text{Bi}_{0.875}\text{Ba}_{0.125}\text{CuSeO}$  (Sui *et al.*, 2013),  $\text{Bi}_{0.92}\text{Pb}_{0.08}\text{CuSeO}$  (Wang *et al.*, 2016) in n-type thermoelectric materials.



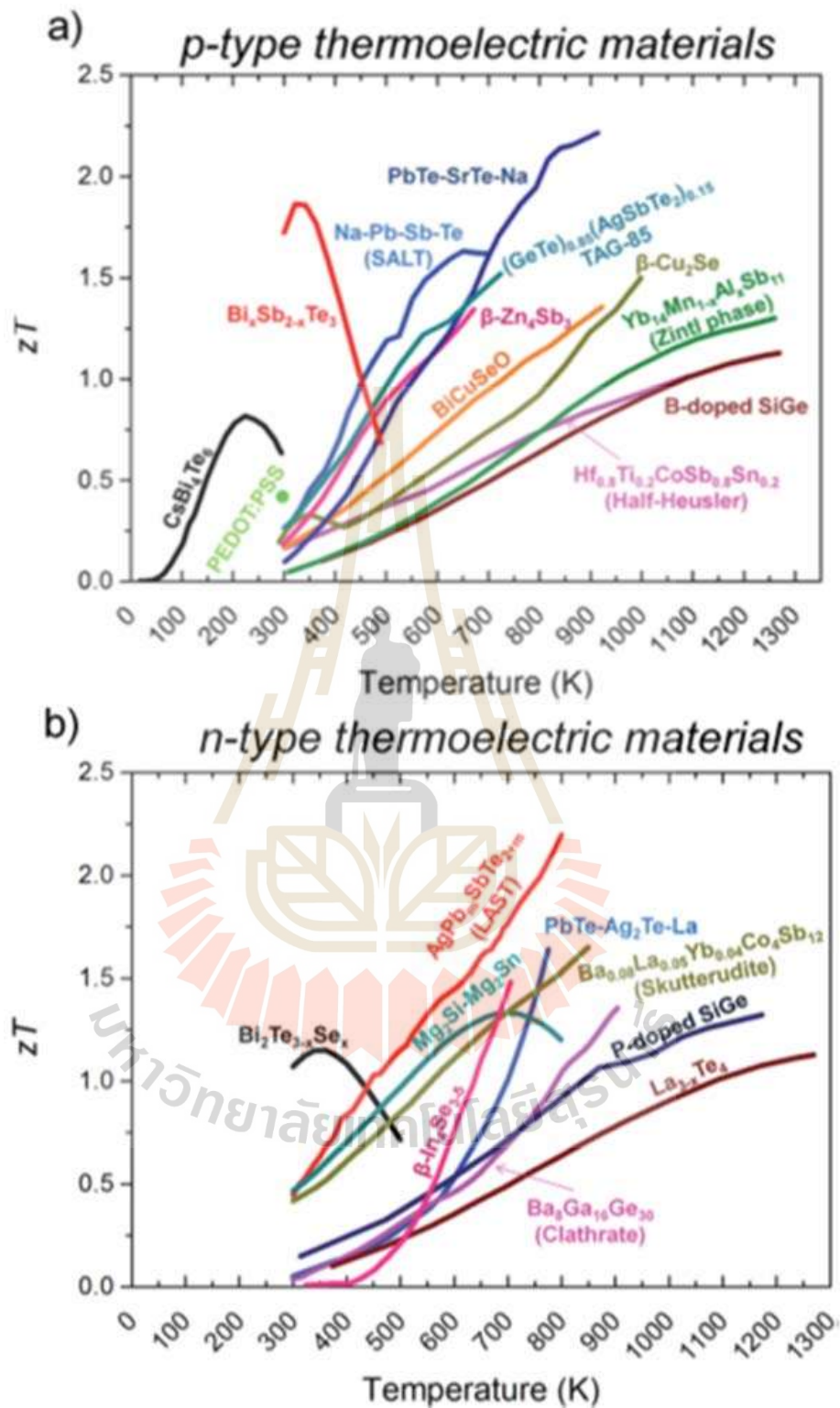


Figure 8 Summary of ZT as a functional temperature of p-type and n-type of thermoelectric materials, a) p-type thermoelectric materials and b) n-type thermoelectric materials (Rull-Bravo *et al.*, 2015).

**Table 1** List of thermoelectric materials versus operating temperatures, power factor, synthesis method and ZT.

Materials	ZT	Type	Temp.(K)	Power Factor ( $\mu\text{Wcm}^{-1}\text{K}^{-2}$ )	Synthesis Method	Reference
$\text{Ag}_2\text{Se}$	1.2	N	273	24.4	Magnetron sputtering	(Perez-Taborda <i>et al.</i> , 2018)
$\text{Ag}_2\text{Se}_{1.06}$	0.84	N	300	30.1	Spark plasma sintering	(Mi <i>et al.</i> , 2014)
$\text{Ag}_2\text{S}_{0.5}\text{Se}_{0.5}$	0.44	N	300	–	Spark plasma sintering	(Liang <i>et al.</i> , 2019)
$\text{Ag}_{1.9}\text{Sn}_{0.1}\text{Se}$	0.9	N	300	4.5	Wet chemical process	(Tee <i>et al.</i> , 2022)
$\text{Bi}_2\text{Te}_3$	0.4	P	300	–	–	(Zhang <i>et al.</i> , 2013)
$\text{Bi}_2\text{Te}_3$	0.7	P	400	–	Arc melting method	(Gharsallah <i>et al.</i> , 2016)
$\text{Zn}_4\text{Sb}_3$	0.81	P	600	–	Mechanical Alloying	(Lee and Lin, 2018)
$\text{Zn}_4\text{Sb}_3$	1.36	P	600	–	Hot pressing	(Kunioka <i>et al.</i> , 2018)
$\text{SnSe}$	1.57	P	300–700	–	Arc melting method	(Gainza <i>et al.</i> , 2020)
$\text{SnS}$	2.6	P	900	0.75	Mechanical Alloying	(Asfandiyar <i>et al.</i> , 2017)
$\text{ZnAl}_2\text{O}_4$	0.44	N	1000	0.18	Microwave-stimulated	(Jood <i>et al.</i> , 2011)
$\text{In}_{2-x}\text{Ce}_x\text{O}_3$	0.47	N	1200	2.5	Spark plasma sintering	(Lan <i>et al.</i> , 2015)

**Table 2** list of thermoelectric materials versus operating temperatures, power factor, synthesis method and ZT. (Continued)

Materials	ZT	Type	Temp.(K)	Power Factor ( $\mu\text{Wcm}^{-1}\text{K}^{-2}$ )	Synthesis Method	Reference
$\text{Ca}_3\text{Co}_4\text{O}_9$	0.40	P	900	–	Spark plasma sintering	(Zhang <i>et al.</i> , 2020)
$\text{Bi}_{0.875}\text{Ba}_{0.125}$ $\text{CuSeO}$	1.4	P	900	6.3	Solid state reaction route	(Sui <i>et al.</i> , 2013)
$\text{Bi}_{0.92}\text{Pb}_{0.08}\text{Cu}$ $\text{uSeO}$	1.1	P	800	7.3	Solid state reaction route	(Wang <i>et al.</i> , 2016)

Among the materials mentioned,  $\beta$ -Zn<sub>4</sub>Sb<sub>3</sub> stands out as an excellent thermoelectric material in the temperature range of 200 – 400 °C (473.15 – 673.15 K) due to its high ZT value, availability of inexpensive elemental sources, low toxicity, and simple crystalline structure. The thermoelectric materials of Zn–Sb system include ZnSb, Zn<sub>3</sub>Sb<sub>2</sub> and Zn<sub>4</sub>Sb<sub>3</sub>, each exhibiting unique thermoelectric properties. The study of the Zn-Sb system in thermoelectric itinerary began when T. J. Seebeck surveyed elements and alloy materials, include correlation of electrical production (potential voltage) and temperatures differences in various materials, including ZnSb alloy (Seebeck, 1895). Later, Zn<sub>3</sub>Sb<sub>2</sub> were reported an optimal ratio of Zn:Sb for maximizing Zn<sub>3</sub>Sb<sub>2</sub> crystalline (Mönkemeyer, 1905), and its thermoelectric properties were further explored (Beer and Cochran, 1952). The phase diagram and structural polymorphs of Zn<sub>4</sub>Sb<sub>3</sub> namely  $\alpha$ -Zn<sub>4</sub>Sb<sub>3</sub>,  $\beta$ -Zn<sub>4</sub>Sb<sub>3</sub> and  $\gamma$ -Zn<sub>4</sub>Sb<sub>3</sub>, were studied by Mayer K. W. in 1978 (Mayer *et al.*, 1978). The thermoelectric properties of  $\beta$ -Zn<sub>4</sub>Sb<sub>3</sub> have been investigated since the 19<sup>th</sup> century, as report by Tapiero M., Spitzer D., and Ugai Ya. (Tapiero *et al.*, 1985; Spitzer, 1970; Ugai *et al.*, 1963). Among the Zn–Sb system materials, the  $\beta$ -Zn<sub>4</sub>Sb<sub>3</sub> is particularly noteworthy for its excellent thermoelectric performance in the intermediate temperature range about 200–400 °C (473.15–673.15 K), achieving a maximum figure of merit ( ZT) approximately 1.3 (Caillat *et al.*, 1997).



### 2.2.2 Process synthesis

The thermoelectric materials were synthesized using various process depending on the structural materials involved. For example, oxide materials were prepared using the sol-gel method (a wet chemical process) (Tee *et al.*, 2022), alloy materials were synthesized via solid-state reaction, mechanical alloying, and quenching methods (Lee and Lin, 2018; Mirela *et al.*, 2015), thin films were created using magnetron sputtering (Perez-Taborda *et al.*, 2018), ceramic bulk materials were produced through hot pressing (Kunioka *et al.*, 2018).

#### Sol-gel method

Sol-gel method is a chemical process used to synthesis a wide range of oxide materials, including thermoelectric materials with oxide structure like  $\text{Ca}_3\text{Co}_4\text{O}_9$ ,  $\text{In}_{2-x}\text{Ce}_x\text{O}_3$  and  $\text{ZnAl}_2\text{O}_4$ . In this method, the initial materials are dissolved in a liquid solvent, and the solution is then heated and stirred to form a gel. Once the gel has dried, the resulting powders is calcined under optimal conditions specific to each material. This process successfully produces the desired materials. Figure 9 illustrates a schematic of sol-gel method.

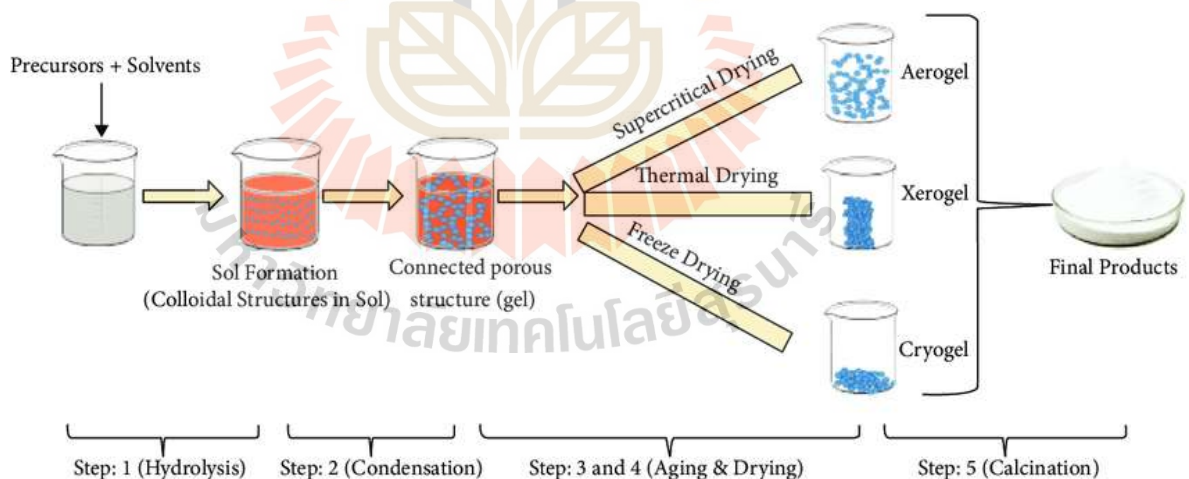
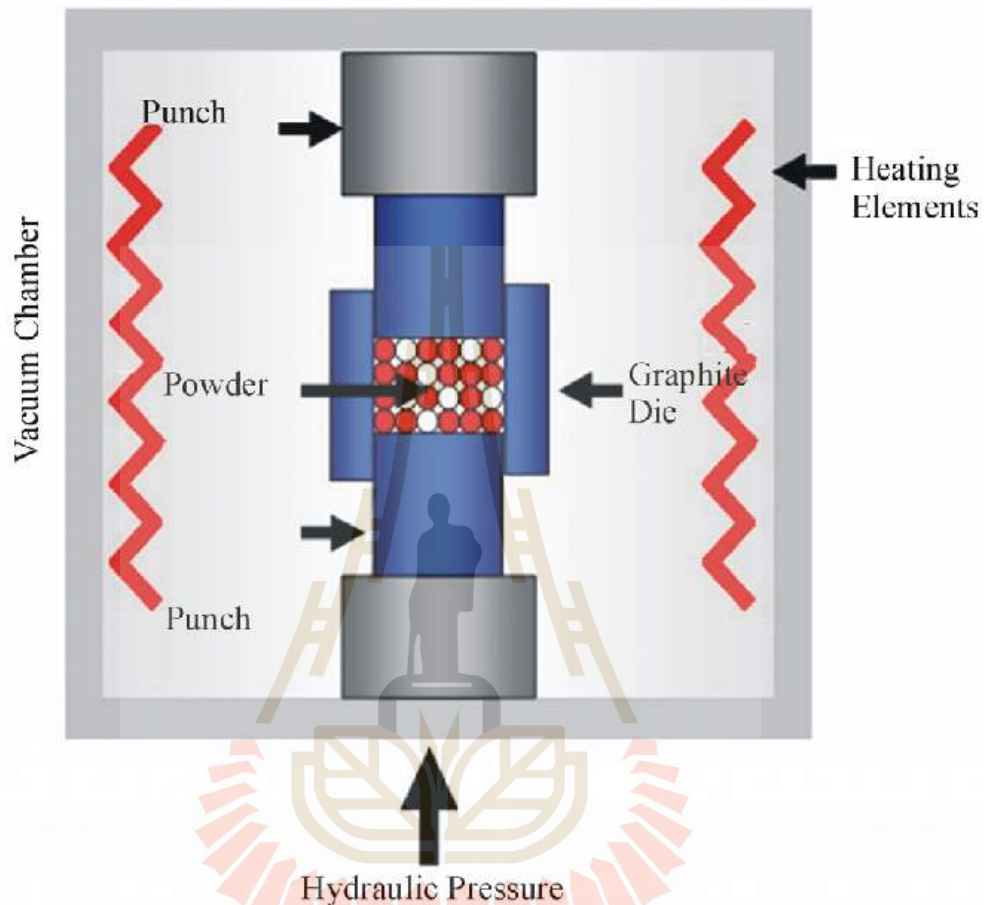


Figure 9 Schematic of sol-gel method step by step (Bokov *et al.*, 2021).

#### Hot pressing technique

Hot pressing technique combines synthesis and sintering into a single process. In this method, the starting materials are prepared in the optimal stoichiometric ratio before being placed into a graphite mold. The mold is then subjected to suitable pressure using a hydraulic system and heated to an optimal temperature, allowing

crystallites to form and the material to be sintered into a bulk pellet. Lately, the sintered ceramic pellet of the desired materials is done. A Schematic diagram illustrating of the hot pressing technique is shown in Figure 10.



**Figure 10** Schematic diagram illustrating the hot pressing technique (Moustafa *et al.*, 2011).

### Magnetron sputtering

Magnetron sputtering is widely used to fabricate film for coating substrate. This technique operates in a vacuum environment to facilitate plasma formation, utilizing gas ions such as Ar, N<sub>2</sub>, O<sub>2</sub>, He, or H<sub>2</sub>. In this process, a bulk materials (target) is subjected to high-energy ionized gas, which bombards the target materials, causing its atoms to be ejected. These ejected ions are then deposited onto the substrate, forming a thin film, guided by the electric field between the anode and cathode. Magnetron sputtering is typically categorized into DC magnetron sputtering and Pulse-DC magnetron sputtering, as illustrated in Figure 11.

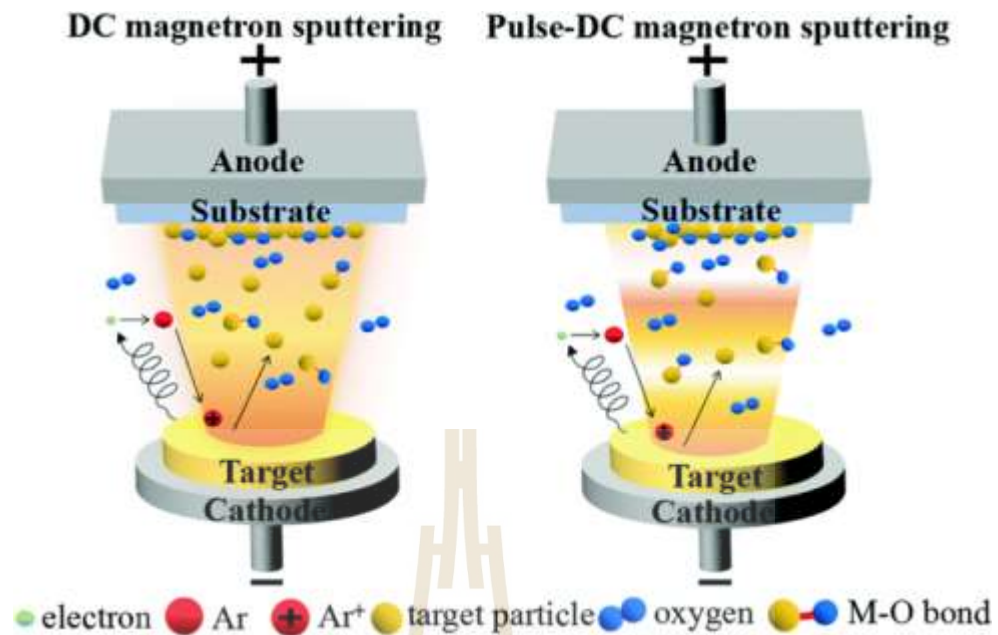


**Figure 11** DC magnetron sputtering and. Pulsed DC magnetron sputtering (Vaccoat, 2024).

### Spark plasma sintering

Spark plasma sintering (SPS) is similar to the hot pressing technique. However, instead of conventional heating, SPS directly heats the material powders using a pulsed direct electrical current at low voltage. An illustration of SPS technique is shown in Figure 12.

มหาวิทยาลัยเทคโนโลยีสุรนารี

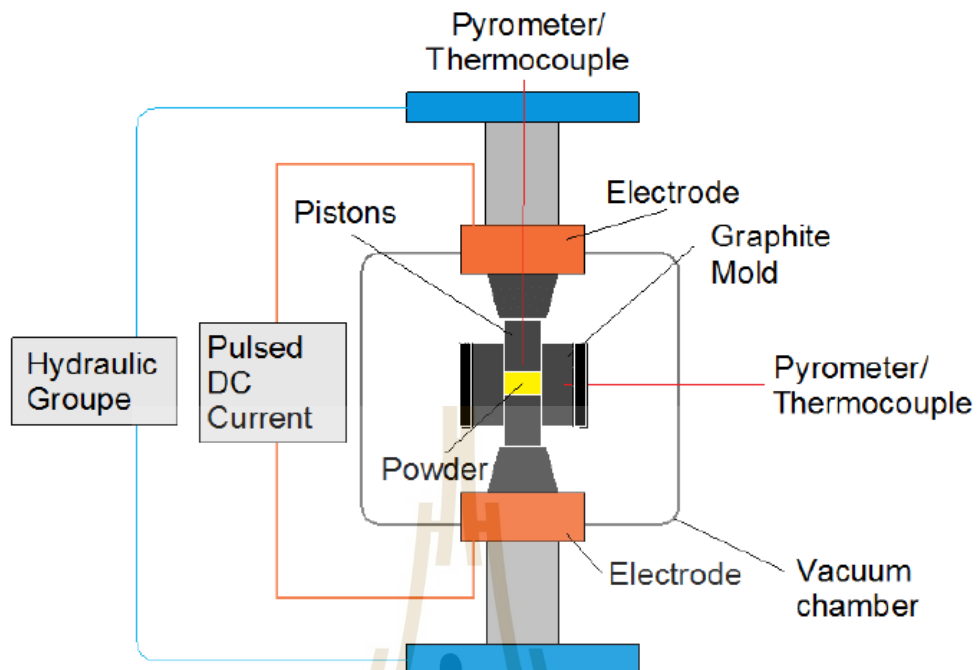
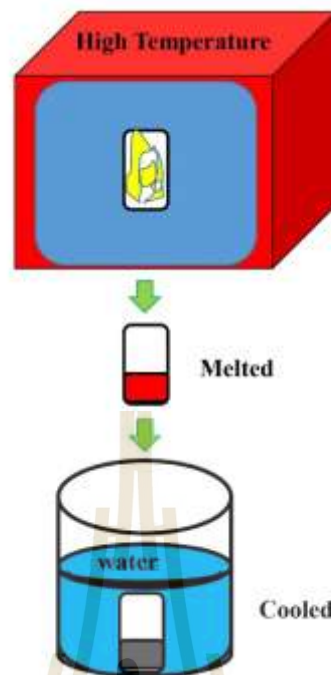


Figure 12 Illustration of Spark plasma sintering technique (Max Planck Institutes).

### Quenching process

The Quenching process involves rapidly cooling a material after melting or calcination. First, the precursor is sealed in a quartz tube and then subjected to melting or calcined at an optimal temperature. Afterward, the quartz tube is quickly submerged in water to cool the sample rapidly. This process prevents the recrystallization of polymorph phases during the cooling phase of calcination process. The general overview of the quenching process is illustrated in Figure 13.



**Figure 13** Illustration of quenching process after melting process.

### Mechanical alloying

Mechanical alloying (MA) is a key step in solid state reaction process, involving the cyclical welding, fracturing, and re-welding of powders particles in a ball mill or a high-energy ball mill chamber. Typically, the MA process is used to mix initial sample powders, flatten and crack bulk sample, and weld powders particles together. This technique is widely used in the preparation of alloy materials. An illustration of the mechanical alloying (MA) is shown in Figure 14.

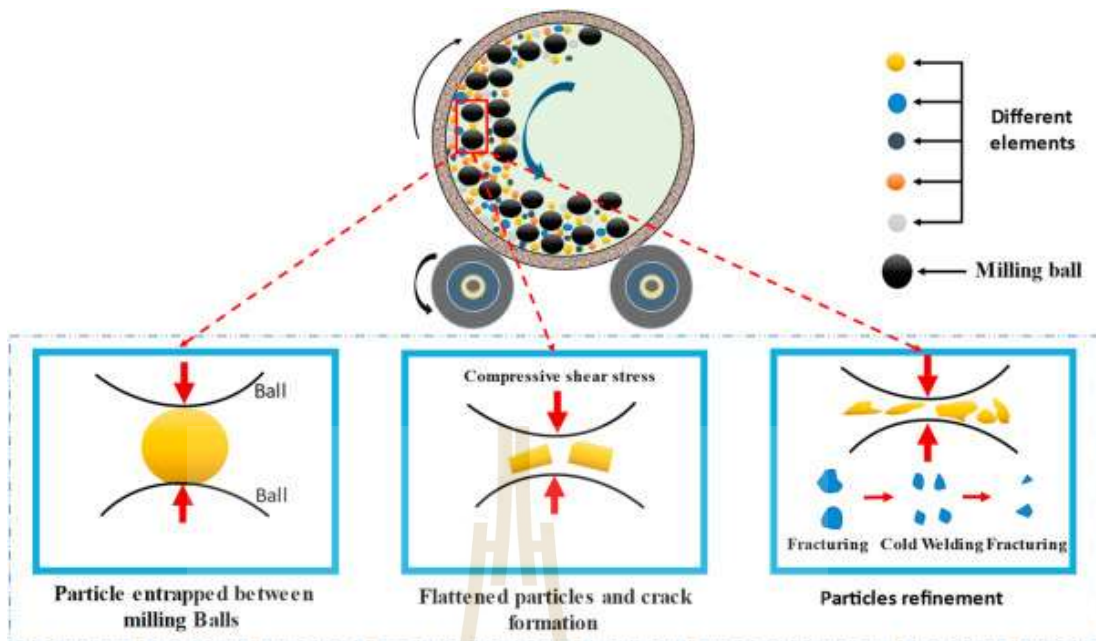


Figure 14 Mechanical alloying with flat and crack bulk sample (Kumar *et al.*, 2022).

### Solid-state reaction

Solid-state reaction is a synthesis method used to produce polycrystalline materials. The reaction typically occurs at high temperatures, depending on the crystallization conditions of each material. Firstly, the MA is used to mix the initial powders. Following this, calcination is applied to form the crystallite phase, and the materials powders is compressed into bulk pellets. Finally, these bulk pellets are sintered to create ceramic pellets. An example of the solid-state reaction process is illustrated in Figure 15.

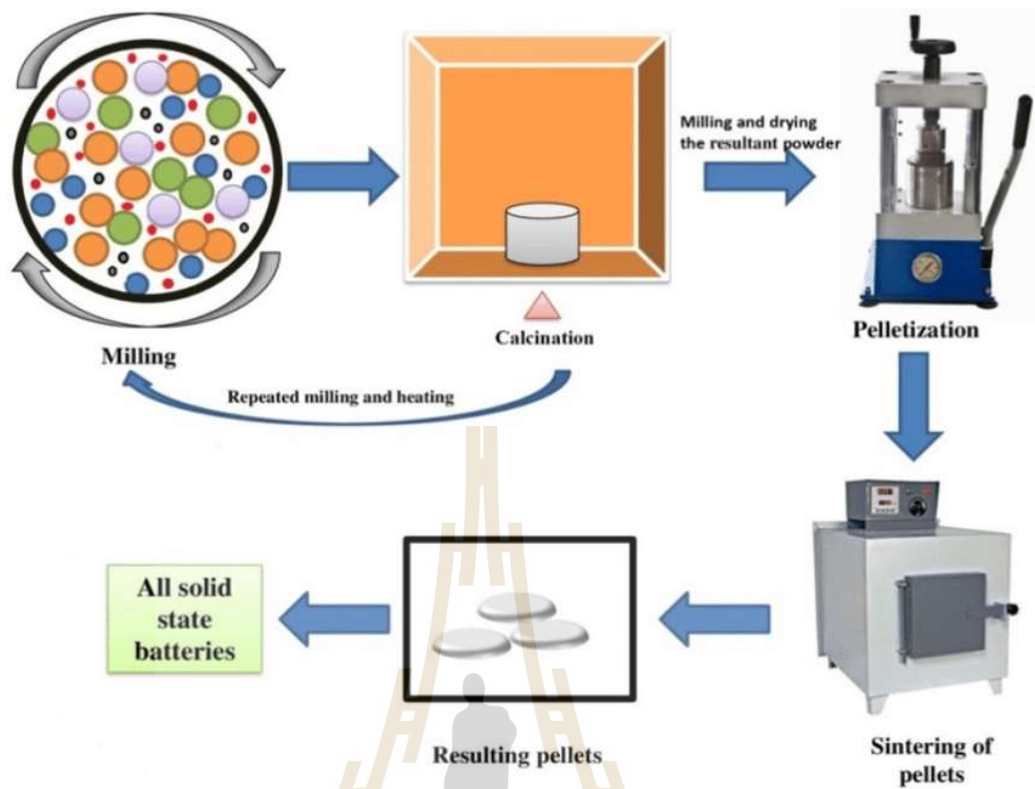


Figure 15 Schematic representation of solid-state reaction method (Sodhiya *et al.*, 2021).

### 2.2.3 Beta zinc antimonide $\beta$ -Zn<sub>4</sub>Sb<sub>3</sub>

In the Zn–Sb system, the commonly studied crystalline phases include ZnSb, Zn<sub>3</sub>Sb<sub>2</sub> and Zn<sub>4</sub>Sb<sub>3</sub> (Adjadj *et al.*, 2006). The Zn<sub>4</sub>Sb<sub>3</sub> which has polymorphs of  $\alpha$ -Zn<sub>4</sub>Sb<sub>3</sub>,  $\beta$ -Zn<sub>4</sub>Sb<sub>3</sub> and  $\gamma$ -Zn<sub>4</sub>Sb<sub>3</sub>, was investigated in terms of its phase diagram by Mayer K. W. in 1978 (Mayer *et al.*, 1978). Among these polymorphs, The  $\beta$ -Zn<sub>4</sub>Sb<sub>3</sub> stands out as an excellent thermoelectric material, particularly in the intermediate temperature range of 200–400 °C (473.15–673.15 K), with a maximum figure of merit (ZT) of approximately 1.3 at 400 °C (Caillat *et al.*, 1997; Ur *et al.*, 2003). The crystalline structure of  $\beta$ -Zn<sub>4</sub>Sb<sub>3</sub> is of the hexagonal rhombohedral space group  $R\bar{3}c$ . The structure of  $\beta$ -Zn<sub>4</sub>Sb<sub>3</sub> contains 30 Sb atoms and 36 Zn atoms per a unit cell (Snyder *et al.*, 2004; Mayer *et al.*, 1978). Zn atoms are partially occupied at the positions 36 Zn(1) site(f) and interstitial positions 36 Zn(1, 2, 3, 4) site(e, f), with varying occupancy percentages (%). Similarly, Sb atoms are partially occupied at the positions 18 Sb(1) site(e) and 12 Sb(2) site(c), also with different occupancy percentages (%). The current issue is determining the accurate model for  $\beta$ -Zn<sub>4</sub>Sb<sub>3</sub> among the proposed models of Zn<sub>39</sub>Sb<sub>30</sub>, Zn<sub>6</sub>Sb<sub>5</sub> and Zn<sub>13</sub>Sb<sub>10</sub> (Nylén *et al.*, 2004; Bokii and Klevtsova, 1965; Snyder *et*

*al.*, 2004). Models for  $Zn_{39}Sb_{30}$  and  $Zn_{13}Sb_{10}$  are shown in Figure 16 while the  $Zn_6Sb_5$  model is depicted in Figure 17.

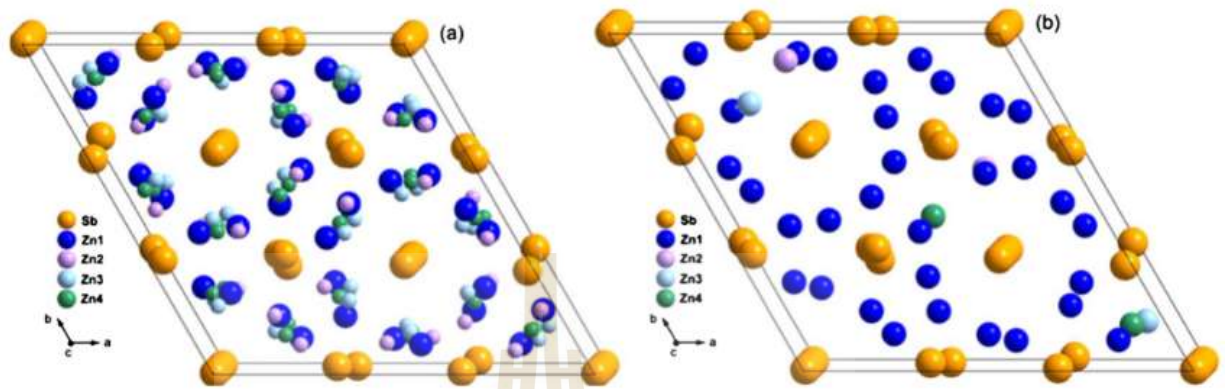


Figure 16 (a) Crystalline structure model of  $Zn_{39}Sb_{30}$  and (b) Crystalline structure model of  $Zn_{13}Sb_{10}$  (Zou *et al.*, 2015).

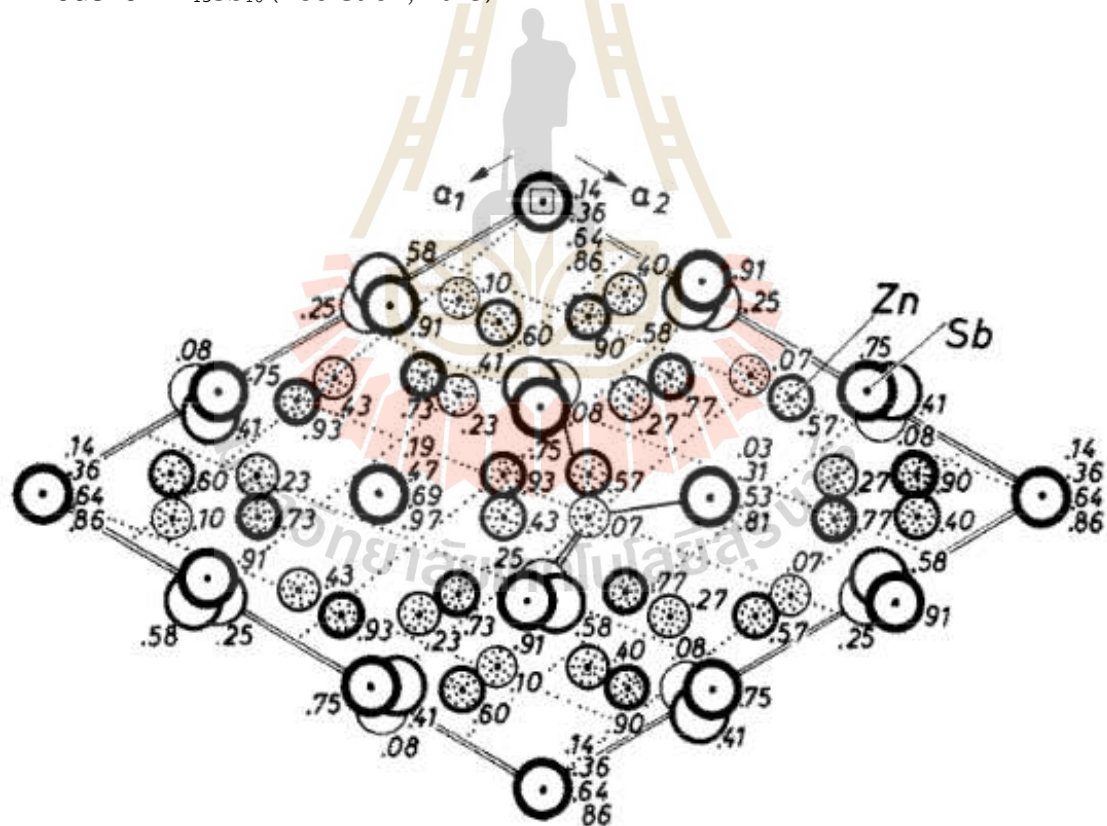
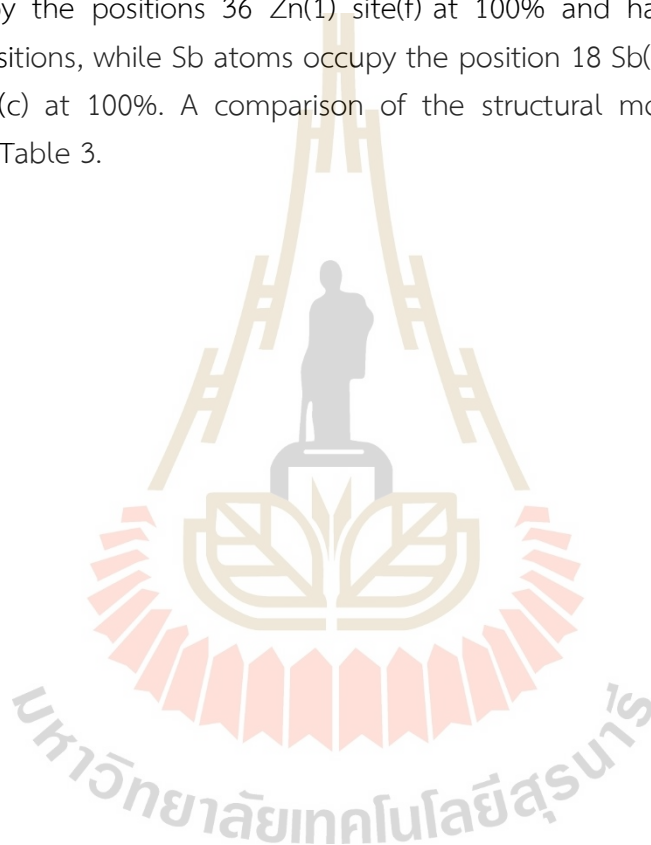


Figure 17 Crystalline structure model of  $Zn_6Sb_5$  (Mayer *et al.*, 1978).

In the  $Zn_6Sb_5$  model or Mayer model, Zn atoms occupy the position 36 Zn(1) site(f) at 100% and 18 Zn(1) site(e) at 11% while Sb atoms are positioned at the position 18 Sb(1) site(e) at 89% and 12 Sb(2) site(c) at 100% occupancy. In the  $Zn_{39}Sb_{30}$  or three interstitial model, Zn atoms are found the position 36 Zn(1) site(f) at 90% occupancy, interstitial positions 36 Zn(2) site(f) with approximately 5%, and 36 Zn(3) site(f) with around 6% occupancy. Sb atoms are located at the position 18 Sb(1) site(e) and 12 Sb(2) site(c) at 100% occupancy each. The full occupancy model, closely matches the experimental X-ray diffraction results for  $\beta$ - $Zn_4Sb_3$  (Qiu *et al.*, 2010). In this model, Zn atoms occupy the positions 36 Zn(1) site(f) at 100% and have no occupancy at interstitial positions, while Sb atoms occupy the position 18 Sb(1) site(e) at 100% and 12 Sb(2) site(c) at 100%. A comparison of the structural models for  $\beta$ - $Zn_4Sb_3$  is presented in Table 3.



**Table 3** Comparison of structure model  $\beta$ -Zn<sub>4</sub>Sb<sub>3</sub> with intermediate step to interstitial model (Snyder *et al.*, 2004).

Site multiplicity	Site occupancy (fraction)			
	Zn(1) (36f)	Sb(1) (18e)	Sb(2) (12c)	Zn Interstitial (36f)
Mayer Model	1	0.89 Sb 0.11 Zn	0	1
Full occupancy Model	1	1	1	0
Three interstitial Model	0.9	1	1	0.17

The calculated X-ray diffraction pattern for the Zn<sub>39</sub>Sb<sub>30</sub>, Zn<sub>6</sub>Sb<sub>5</sub> and Zn<sub>13</sub>Sb<sub>10</sub> models appear very similar, with nearly identical diffraction peaks. This research, the synthesized  $\beta$ -Zn<sub>4</sub>Sb<sub>3</sub> powders were compared with Mayer's model of Zn<sub>6</sub>Sb<sub>5</sub> because of Mayer's model of Zn<sub>6</sub>Sb<sub>5</sub> was refined based on calculations and experiment. The X-ray diffraction (XRD) patterns for the Zn<sub>39</sub>Sb<sub>30</sub>, Zn<sub>6</sub>Sb<sub>5</sub> and Zn<sub>13</sub>Sb<sub>10</sub> models are shown in Figure 18, Figure 19 and Figure 20, respectively.

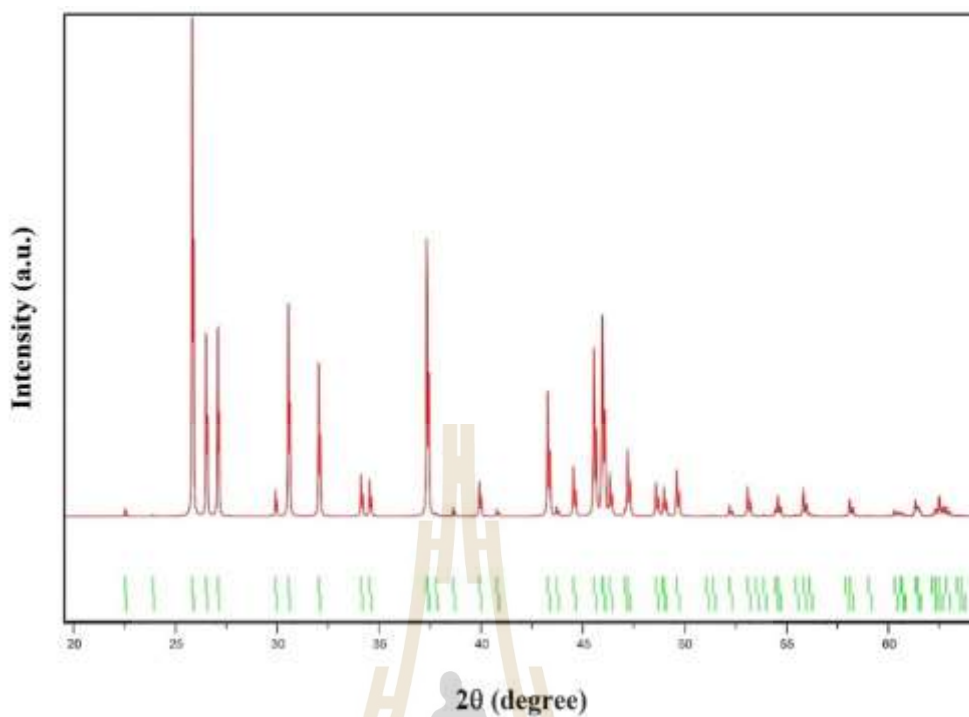


**Figure 18** Calculated X-ray diffraction pattern yields of  $Zn_{39}Sb_{30}$  model by using Boru's CIF- 7040405 (Borup *et al.*, 2016).

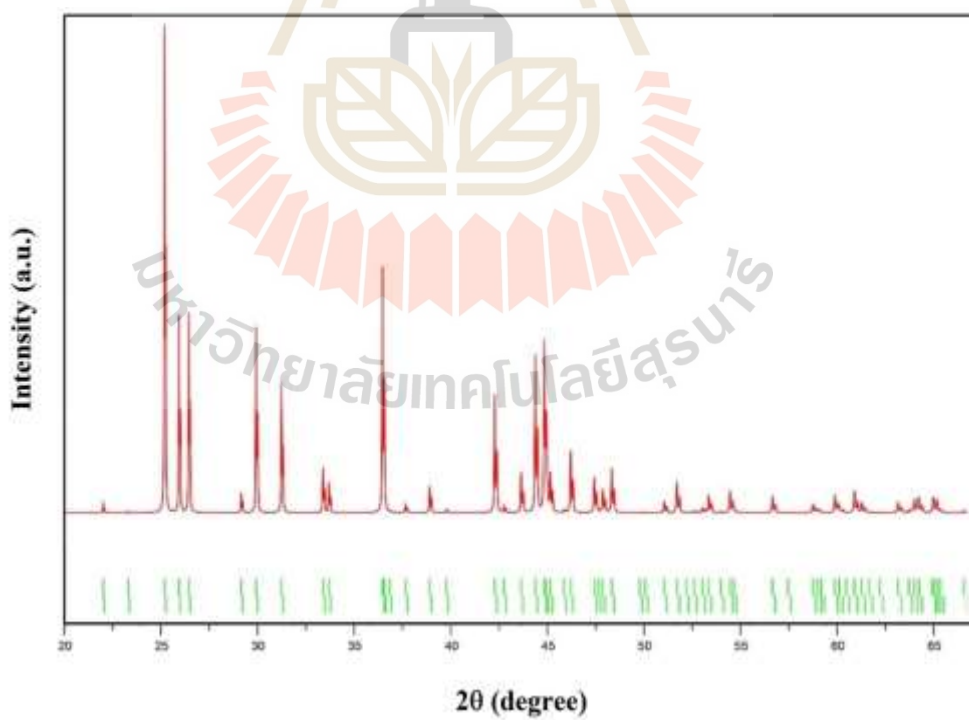


**Figure 19** Calculated X-ray diffraction pattern yields of  $Zn_6Sb_5$  model by using Jeffrey Snyder's CIF-cm0515505\_si\_001(Snyder *et al.*, 2004).

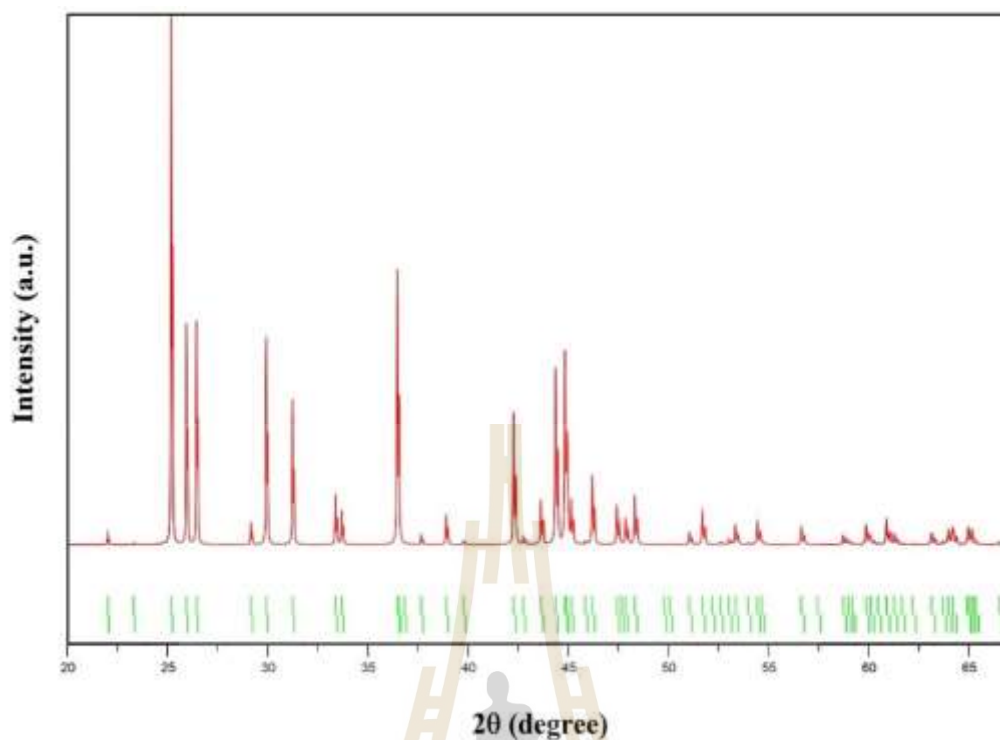


**Figure 20** Calculated X-ray diffraction pattern yields of  $Zn_{13}Sb_{10}$  model by using Yurij's CIF- 4001474 (Mozharivskij *et al.*, 2006).

The most popular method for synthesizing high-purity  $\beta$ - $Zn_4Sb_3$  materials is quenching. This process involves placing powdered Zn and Sb elements into a sealed quartz tube filled with argon gas, heating the mixture to 700–750°C to melt it into ingot of  $\beta$ - $Zn_4Sb_3$  (Lin *et al.*, 2014; Böttger *et al.*, 2011). The ingot is crushed into powder using a ceramic mortar and pestle. The XRD patterns of the  $\beta$ - $Zn_4Sb_3$  powders amply produced by both Lin and Böttger's research groups were found to match the calculated XRD patterns of the  $Zn_{39}Sb_{30}$ ,  $Zn_6Sb_5$  and  $Zn_{13}Sb_{10}$  models. XRD pattern of quenched  $\beta$ - $Zn_4Sb_3$  materials are displayed in Figure 21 (Böttger *et al.*, 2011). Although, high pure  $\beta$ - $Zn_4Sb_3$  materials can be synthesized using the quenching method, it is not optimal for producing large quantities due to the challenges associated with filling the quartz tube with precursors and crushing the material into fine  $\beta$ - $Zn_4Sb_3$ .

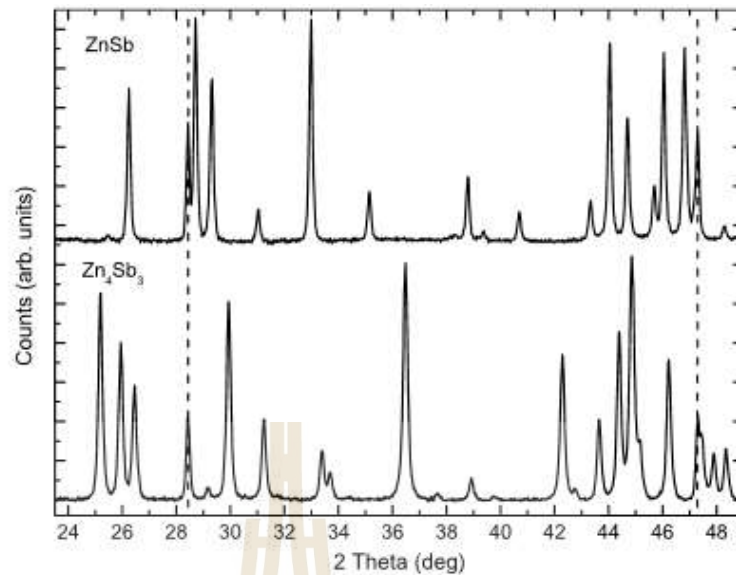


**Figure 21** XRD yields of ZnSd (top) and Zn<sub>4</sub>Sb<sub>3</sub> (bottom) were prepares by quenching method (Böttger *et al.*, 2011).

The Mechanical alloying method is also used to prepare  $\beta$ -Zn<sub>4</sub>Sb<sub>3</sub>, making it suitable for conventional production and large-scale synthesis (Lee and Lin, 2018). The  $\beta$ -Zn<sub>4</sub>Sb<sub>3</sub> powders synthesized using this method exhibit an XRD pattern similar to those produced by the quenching method. The XRD pattern of the  $\beta$ - powders synthesized through mechanical alloying is shown in Figure 22. As well known, Zn element can evaporate at temperature of 350 °C. Therefore, when using the calcination method, it is important to compensate for this by adding extra Zn powder to the sample precursors to ensure optimal synthesis (Ueno *et al.*, 2006; Ito *et al.*, 2003; Shim *et al.*, 2015).

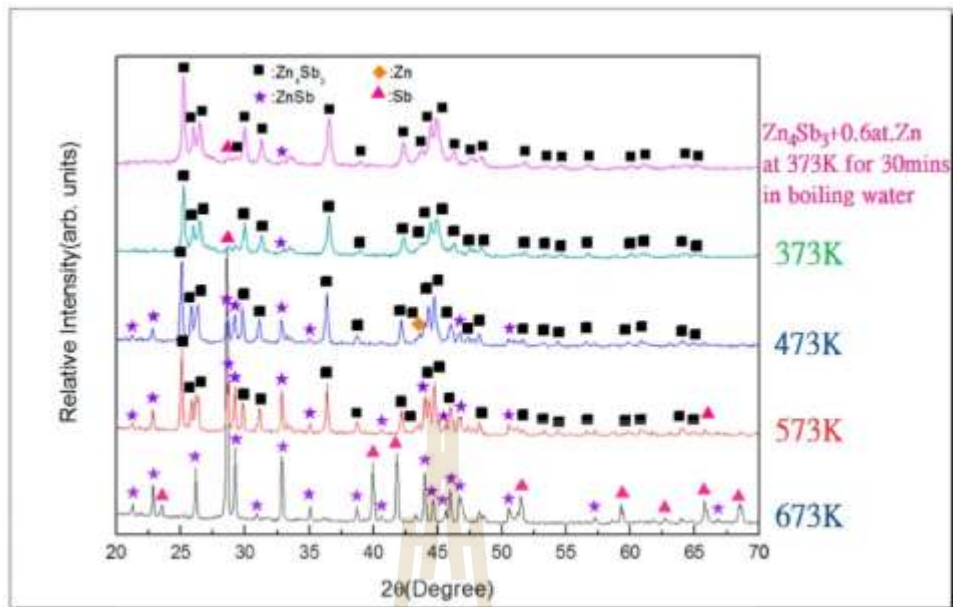


**Figure 22** XRD pattern of  $\beta$ - $\text{Zn}_4\text{Sb}_3$  with 0.6 at. % Zn rich via different sintered temperatures in vacuum (Lee and Lin, 2018).

The mechanical alloying (MA) method is a materials synthesis technique that uses a ball mill to grind and mix initial precursor elements, forming crystalline phase and homogeneous mixture. However, since the crystalline phase is often incomplete after milling, the precursors are further calcined and sintered to fully develop the crystalline structure, a process known as the "solid-state reaction method". This thesis employs the solid-state reaction process to synthesis  $\beta$ - $\text{Zn}_4\text{Sb}_3$  powders. According to the MA method, the precursor powders formed small crystalline phase of  $\beta$ - $\text{Zn}_4\text{Sb}_3$ ,  $\text{ZnSb}$ ,  $\text{Sb}$  and  $\text{Zn}$  phases as shown in the XRD results in Figure 23. SEM images of the precursor powders before and after using MA method are shown in Figure 24. Generally, the thermoelectric materials are typically pressed into ceramic pellets to study its thermoelectric properties and for use in modules. Therefore, the compression and sintering processes were studied to determine the optimal conditions for fabricating  $\beta$ - $\text{Zn}_4\text{Sb}_3$  ceramic with homogeneous surfaces and minimal porosity (Ahn *et al.*, 2011). The surfaces of the  $\beta$ - $\text{Zn}_4\text{Sb}_3$  ceramic pellet were influenced by temperature and pressure that presented in Figure 25 and Figure 26.

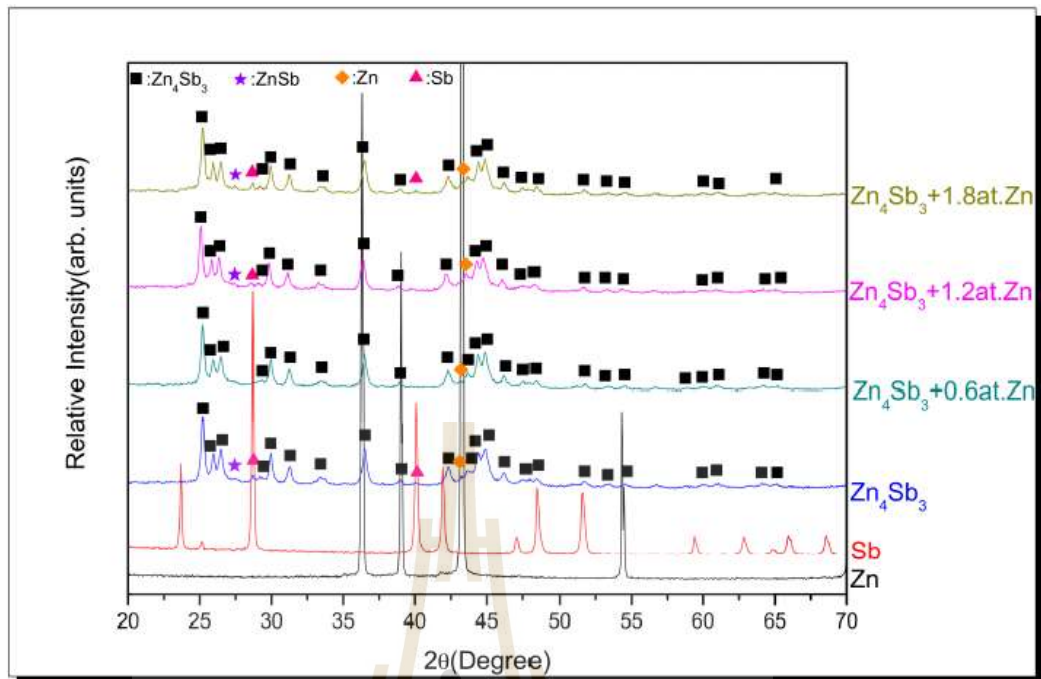


Figure 23 XRD pattern of milled  $\beta$ - $\text{Zn}_4\text{Sb}_3$  with different at. % Zn rich (Lee and Lin, 2018).

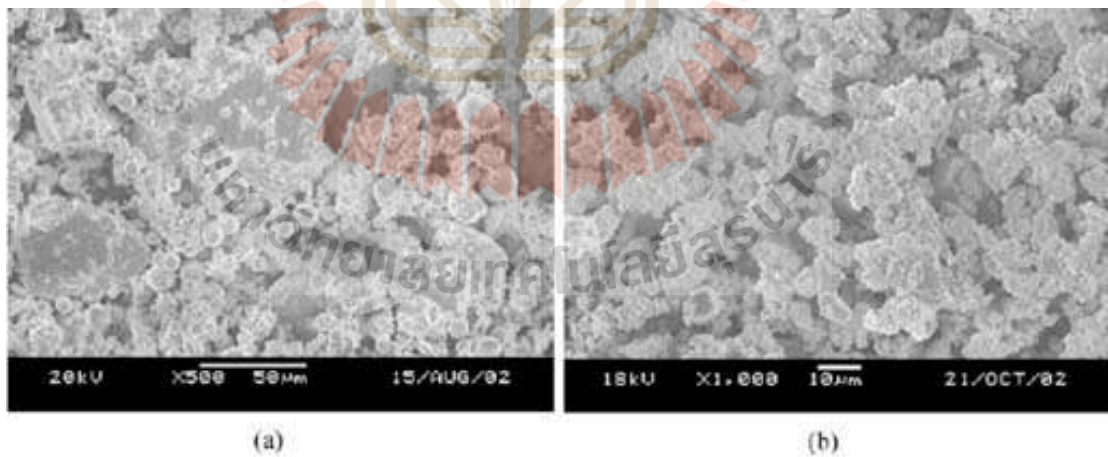
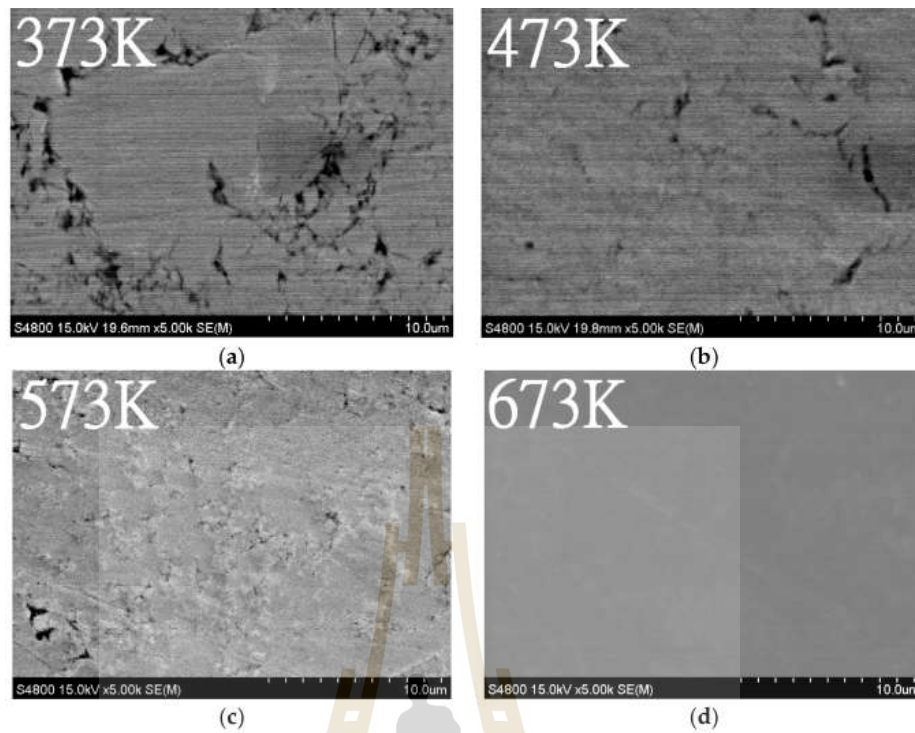
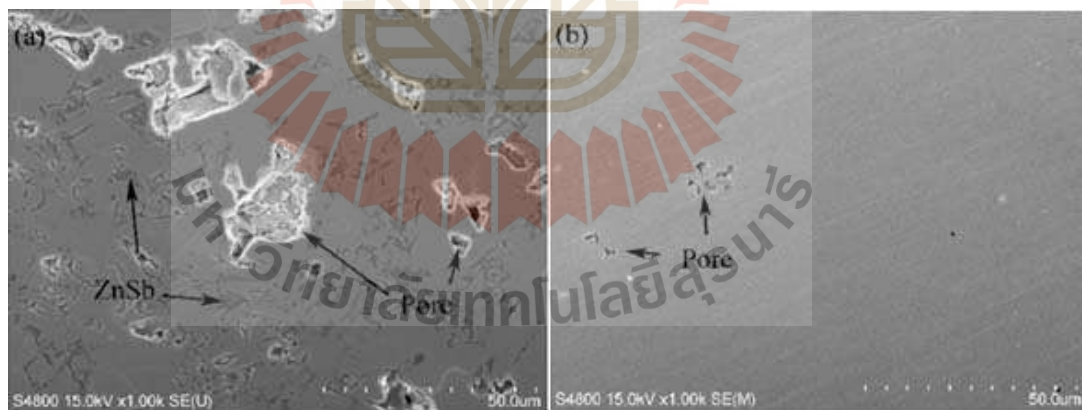


Figure 24 SEM images of  $\beta$ - $\text{Zn}_4\text{Sb}_3$  powder; (a) Before mechanical alloying method and (b) After mechanical alloying method (Ur *et al.*, 2003).



**Figure 25** SEM images of hot-pressed  $\beta$ - $\text{Zn}_4\text{Sb}_3$  ceramic at temperatures of 373 K, 473 K, 573 K and 673 K with pressure 0.98 GPa (Lee and Lin, 2018).



**Figure 26** SEM images of hot-pressed  $\beta$ - $\text{Zn}_4\text{Sb}_3$  ceramic with pressing pressures of 100 MPa (a) and 200 MPa (b) at 673 K (Ahn *et al.*, 2011).

Based on the experimental results, applying high pressing pressure and sintering at elevated temperatures leads to reduced porosity and a smooth surface on  $\beta$ - $\text{Zn}_4\text{Sb}_3$  pellet ceramic. Additionally, these conditions result in higher density, which significantly affects the Seebeck coefficient, thermal conductivity, and electrical conductivity. According to the research by Ahn J.H. and colleagues, they observed that

applying a high pressure of 250 MPa during the compression of  $\beta$ -Zn<sub>4</sub>Sb<sub>3</sub> ceramic pellets resulted in an improved Seebeck coefficient of 200  $\mu\text{V/K}$  at 673 K, stable thermal conductivity ranging from 0.7–0.6  $\text{W/mK}$  at 473–673 K, and low electrical resistivity (indicating good electrical conductivity) of 115  $\mu\Omega\text{m}$  across the same temperature range (Ahn *et al.*, 2011). The effects of pressing pressure on the Seebeck coefficient, thermal conductivity, and electrical conductivity are illustrated in Figure 27. This thesis, high pressing pressure and elevated sintering temperatures were employed to fabricate  $\beta$ -Zn<sub>4</sub>Sb<sub>3</sub> ceramic pellets.

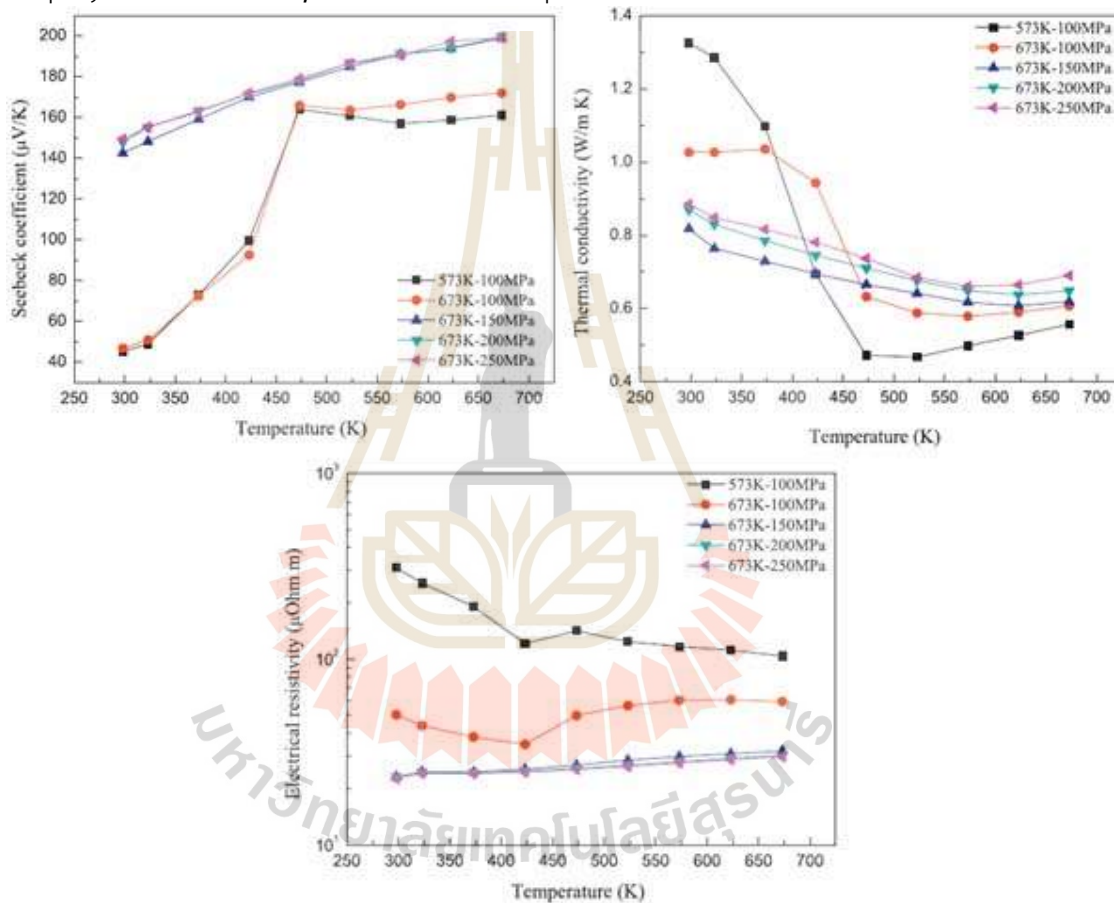


**Figure 27** Seebeck coefficient, thermal conductivity and electrical conductivity of hot-pressed  $\beta$ -Zn<sub>4</sub>Sb<sub>3</sub> ceramic pellets via different temperatures and pressure (Ahn *et al.*, 2011).

### 2.3 Thermoelectric generator modules

Thermoelectric generators modules are key components in electronic devices, used to directly convert heat into electrical current since the 19<sup>th</sup> century. The thermoelectric effect, first discovered by Thomas Johann Seebeck in 1821, Typically, thermoelectric generators (TEGs), also known as longitudinal TEGs, are constructed

using either dual-leg or single-leg designs. In the dual-leg TEGs, both P-type and N-type thermoelectric materials are used, with electric and heat transport occurring parallel to each other along isotropic properties (Crawford, 2014). In contrast, single-leg TEGs are made with either P-type or N-type thermoelectric materials, as shown in Figure 28 and Figure 29, respectively. On the other hand, transverse thermoelectric (TTE) modules, where the directions of electric and heat transport are perpendicular, are primarily used in applications like thermal radiation detectors, thermocouples, and cooling systems. The transverse thermoelectric modules often feature serpentine or tilted arrangements with anisotropic properties, as illustrated in Figure 30.

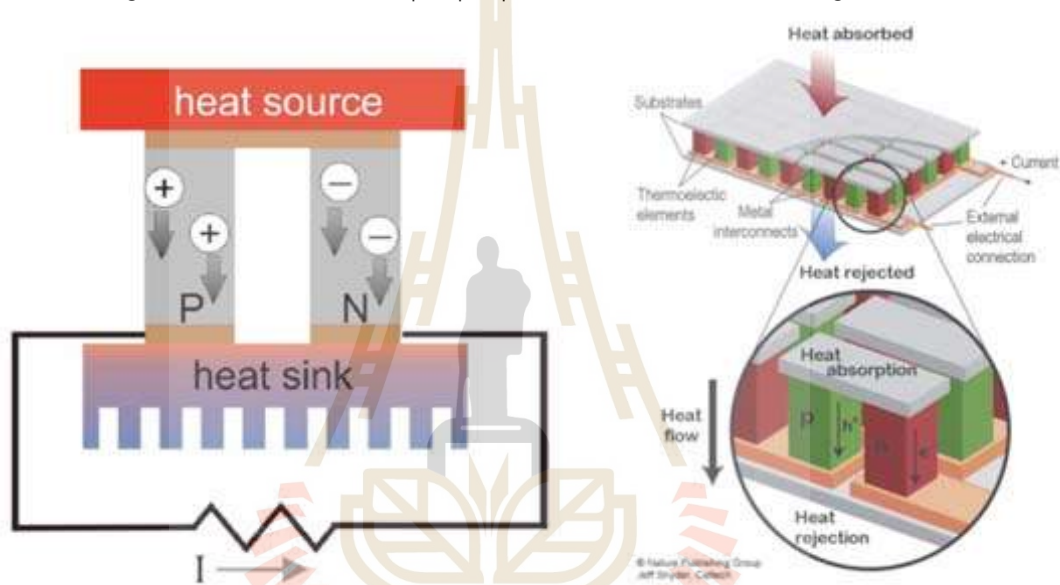


**Figure 28** Schematic of a dual leg TEG module and dual leg series TEG device with isotropic properties (Crawford, 2014).

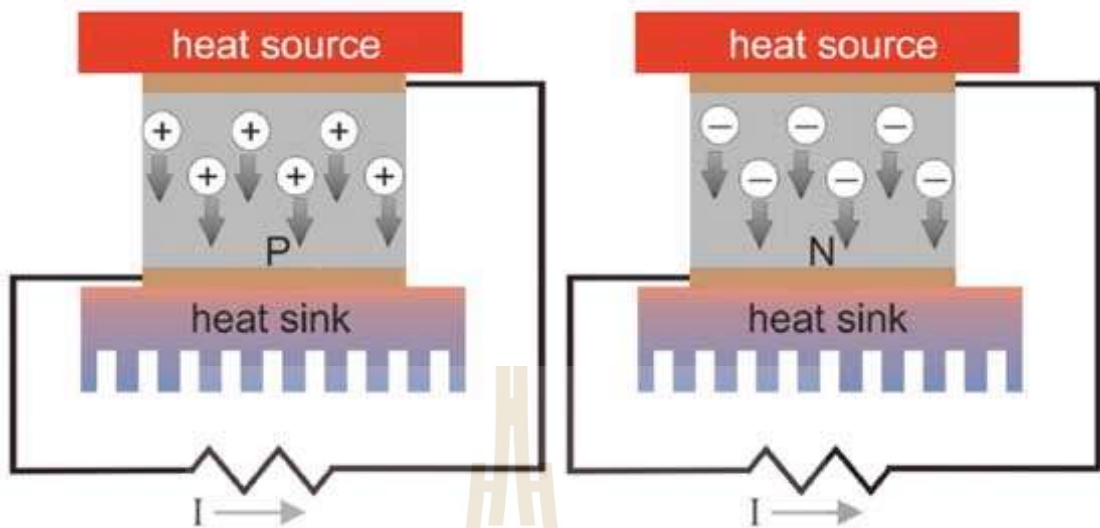


**Figure 29** Schematic of single leg TEG module with isotropic properties (Crawford, 2014).

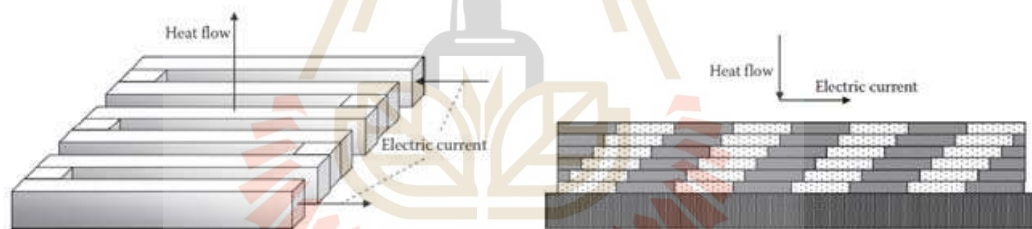


**Figure 30** Schematic of serpentine and tilted-multilayer TTE module with anisotropic thermoelectric properties (Goldsmid, 2017).

TTE modules have gained popularity since the 19th century, with developments in tilted ceramic block TTE and artificially tilted TTE films (Zahner *et al.*, 1998; Kyarad and Lengfellner, 2006; Reitmaier *et al.*, 2010; Dreßler *et al.*, 2015; Kanno, 2016; Mu *et al.*, 2019; Li *et al.*, 2022; Uchida, 2022). Mostly, the studies have focused on improving the performance of TTE modules to make them suitable as TEG modules for powering microelectronic devices (Bathen and Linder, 2017; Jaworski *et al.*, 2010; Kim *et al.*, 2021; Uchida, 2022; Mu *et al.*, 2019). The TTE films module and TTE ceramic pellet module are shown in Figure 31 and Figure 32. However, TE modules have not yet matched the performance of TEG modules due to limitations such as electrical current loss and high electrical resistivity. These issues are primarily caused by the tilted angle of the TTE module, which leads to the formation of self-resistance barriers within the module (Goldsmid, 2017).

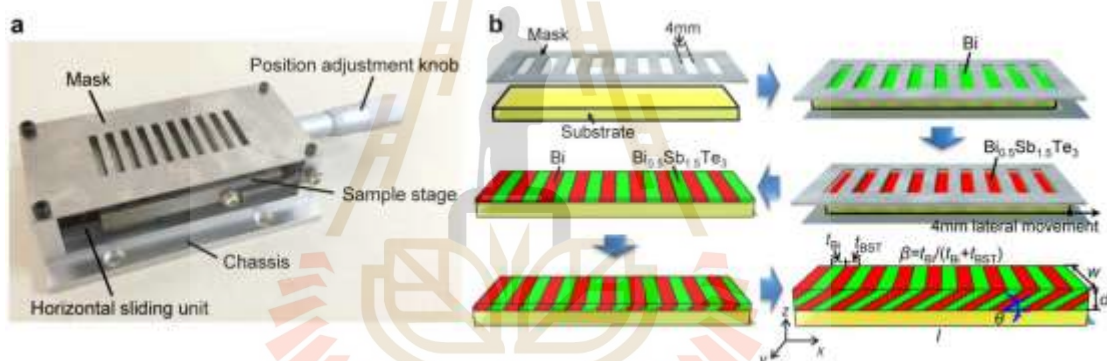


**Figure 31** (a) Photograph of misaligned make assembly equipment for sputtering Bi/Bi<sub>0.5</sub>Sb<sub>1.5</sub>Te<sub>3</sub> TTE device, (b) Illustration of layer by layer stacking of Bi/Bi<sub>0.5</sub>Sb<sub>1.5</sub>Te<sub>3</sub> (Mu *et al.*, 2019).

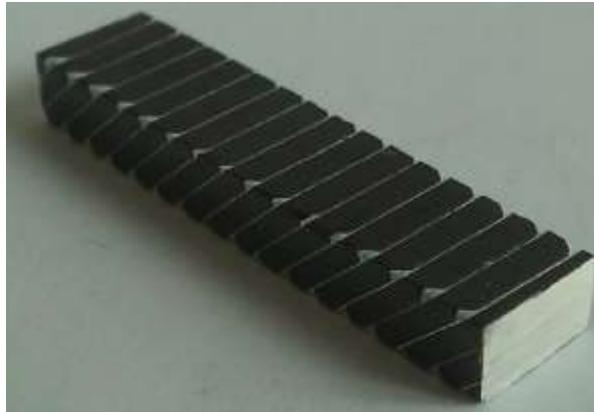


**Figure 32** Tilted ceramic block TTE device prepared by  $\text{La}_{1.97}\text{Sr}_{0.03}\text{CuO}_4$  with silver paste connector (Dreßler *et al.*, 2015).

Recently, a new TEG model known as the monolithic TEG module has been developed. This all-in-one TEG module features a structural design that simplifies fabrication processes. Various thermoelectric configurations can be applied to the monolithic TEG module, as shown in Figure 33. A key aspect of all monolithic TEG modules is the use of alternative resistive materials to separate TEG cells and conductive materials for electrical connections, such as ZO,  $\text{SiO}_2$ , Ag,  $\text{Ag}_2\text{S}$ -alloy (Lai *et al.*, 2022). The terminal positions of electrical charges for different monolithic TEG module designs, such as single leg, dual leg, unileg, and transverse are illustrated in Figure 34. Huajun L. and his research team reported on the fabrication process of monolithic  $\text{Ag}_2\text{S}_{0.2}\text{Se}_{0.8}/\text{Ag}_2\text{S}/\text{Bi}_{0.5}\text{Sb}_{1.5}\text{Te}_3$  TEG modules, which are dual-leg TEG models consisting of three alloy materials of  $\text{Ag}_2\text{S}_{0.2}\text{Se}_{0.8}$ ,  $\text{Bi}_{0.5}\text{Sb}_{1.5}\text{Te}_3$ ,  $\text{Ag}_2\text{S}$  as n-type, p-type and insulator materials, respectively (Lai *et al.*, 2022) (Dreßler *et al.*, 2015). However, this monolithic TEG module is limited to low-temperature applications due to the material constraints of  $\text{Ag}_2\text{S}_{0.2}\text{Se}_{0.8}$  and  $\text{Bi}_{0.5}\text{Sb}_{1.5}\text{Te}_3$  materials (Mansouri *et al.*, 2021; Singh *et al.*, 2020). The monolithic  $\text{Ag}_2\text{S}_{0.2}\text{Se}_{0.8}/\text{Ag}_2\text{S}/\text{Bi}_{0.5}\text{Sb}_{1.5}\text{Te}_3$  TEG modules is shown in Figure 35.

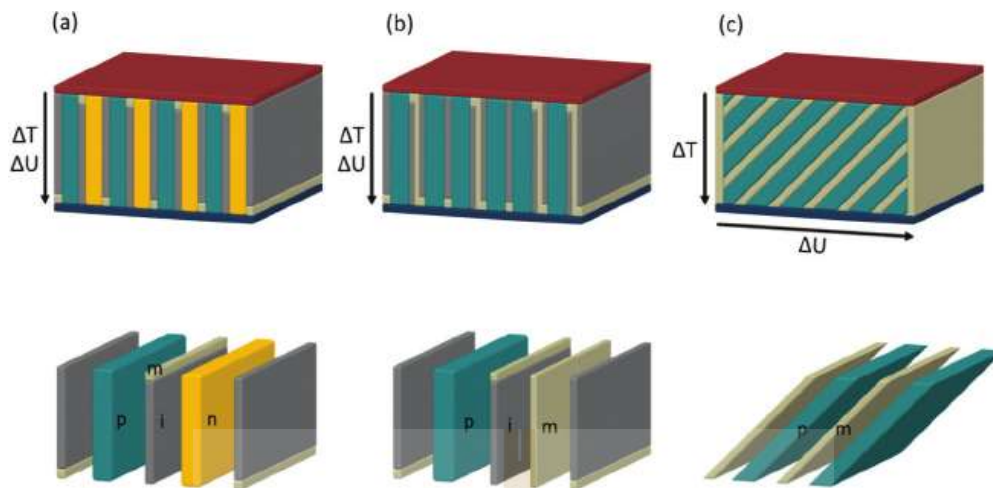


**Figure 33** Schematic of dual leg, unleg and transverse series monolithic TEG device (Dreßler *et al.*, 2015).

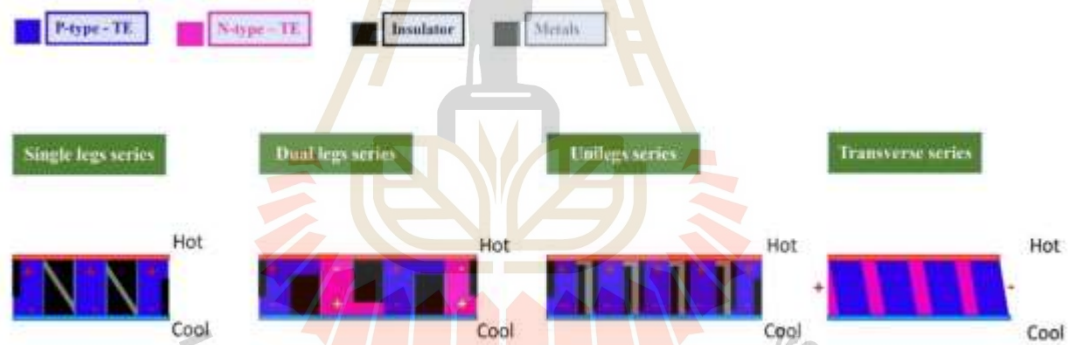


**Figure 34** Illustration of charge positions of all monolithic TEGs model.

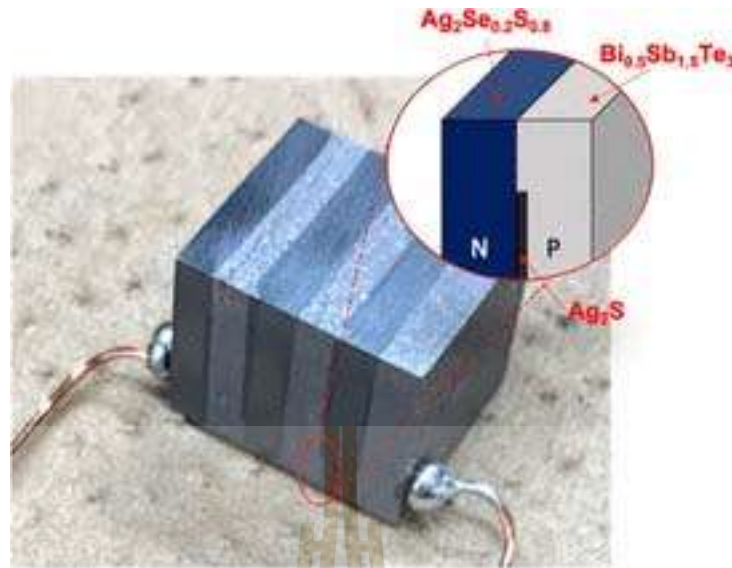


**Figure 35** Monolithic  $\text{Ag}_2\text{S}_{0.2}\text{Se}_{0.8}/ \text{Ag}_2\text{S} / \text{Bi}_{0.5}\text{Sb}_{1.5}\text{Te}_3$  TEG modules.

To simplify the fabrication processes of TEG modules and enhance for using in industrials waste heat recycling, in this thesis presents the development of novel single leg series monolithic  $\beta\text{-Zn}_4\text{Sb}_3/\text{ZnO}$  TEG modules with a modified zigzag electrical connection. Synthesized  $\beta\text{-Zn}_4\text{Sb}_3$  and commercial ZnO were used as p-type thermoelectric material and insulator material, respectively (Jantrasee *et al.*, 2016). The  $\beta\text{-Zn}_4\text{Sb}_3$  powers were synthesized through solid-state reaction and calcination under a flow of Ar gas flow. These powders were characterized and used to prepare sintered  $\beta\text{-Zn}_4\text{Sb}_3$  pellets, which thermoelectric properties were evaluated. Efficient performance of the monolithic  $\beta\text{-Zn}_4\text{Sb}_3/\text{ZnO}$  TEG modules was assessed by measuring the electrical power output, calculated deploying equation of

$$P_{\text{out}} = NI^2R_L = N \left[ \frac{S(T_h - T_c)}{R_g + R_L} \right]^2 R_L \quad (109) \quad (\text{Goldsmid, 2010}).$$

## CHAPTER III

### EXPERIMENTAL PROCEDURE

Chapter III presents the experimental procedures of this research. The detailed steps are outlined in the following sections.

#### 3.1 Synthesis of $\beta$ -Zn<sub>4</sub>Sb<sub>3</sub> powders

The  $\beta$ -Zn<sub>4</sub>Sb<sub>3</sub> powders were prepared through a solid-state reaction and calcination under a flow of Ar gas. Initially, elemental powders of Zn [99.9%, Alfa Aesar™] and Sb [99.5%, Sigma-Aldrich] were prepared in a stoichiometric ratio 4:3 with with excess Zn powders conditions. The premixed powders were weighted to 10 g for each Zn-rich condition. The excess Zn rich was added to compensate for any losses of Zn elements due to evaporation during high temperatures calcination (Ur *et al.*, 2003). The premixed powders, along with 2 mm zirconia balls, were placed into a 125 ml polypropylene (PP) cylindrical bottle, with zirconia balls filling approximately 75% of the PP bottle's volume. Then, the filled PP bottle was rotated at a maximum speed of 700 rpm using a roller milling machine for 24 hours. After milling, the Zn-Sb powder mixture was calcined under an Ar gas flow, which was passed through a water jar serving as an air barrier. The heating rate was set to 10 °C/min until the target temperature was reached, where it was then held steady for specified time conditions. Finally, the mixture was allowed to cool to room temperature. An illustration of the process synthesis is shown in Figure 36. The series of synthesis conditions of  $\beta$ -Zn<sub>4</sub>Sb<sub>3</sub> powders is presented in Table 4. These conditions were tested to compare the crystallite phases of  $\beta$ -Zn<sub>4</sub>Sb<sub>3</sub> in order to determine the optimal synthesis conditions.

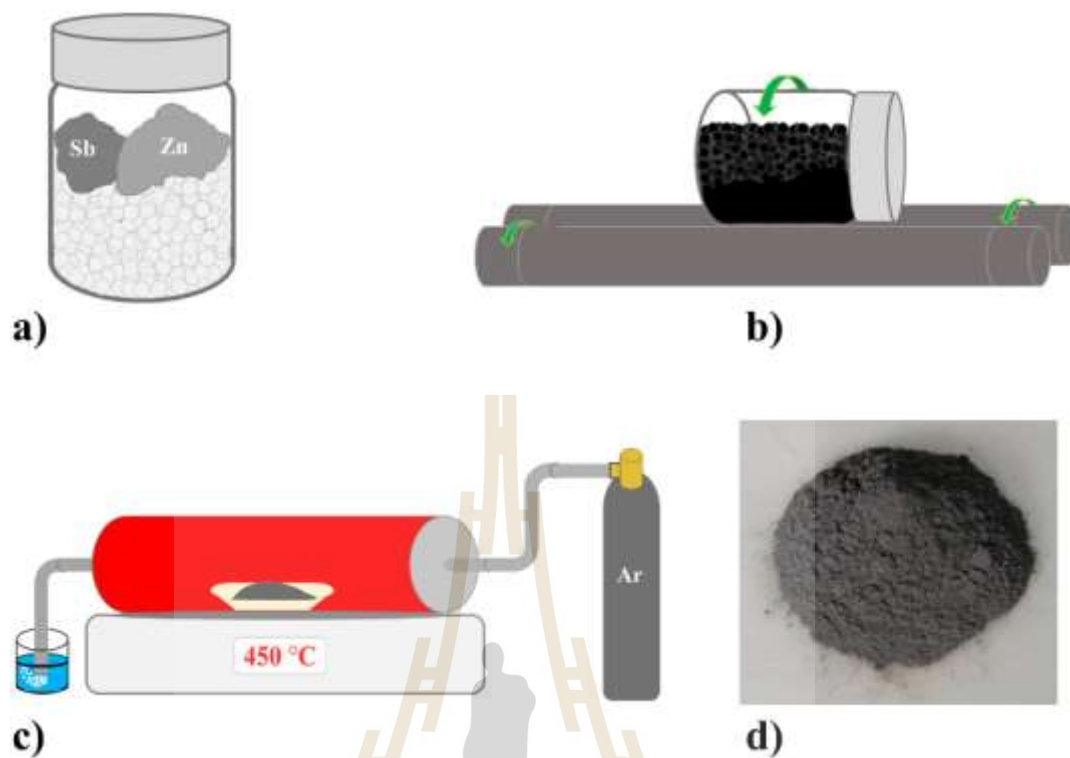


**Figure 36** Process synthesis of  $\beta$ - $\text{Zn}_4\text{Sb}_3$  powders: a) Premixed powders with zirconia balls were filled into a PP bottle, b) The filled PP bottle was rotated using roller milling machine, c) The mixture powders were calcined under Ar gas flow, and d) Synthesized  $\beta$ - $\text{Zn}_4\text{Sb}_3$  powders.

**Table 4** Series conditions of process synthesis of  $\beta$ -Zn<sub>4</sub>Sb<sub>3</sub> powders versus excess Zn, calcination temperature and calcination holding time.

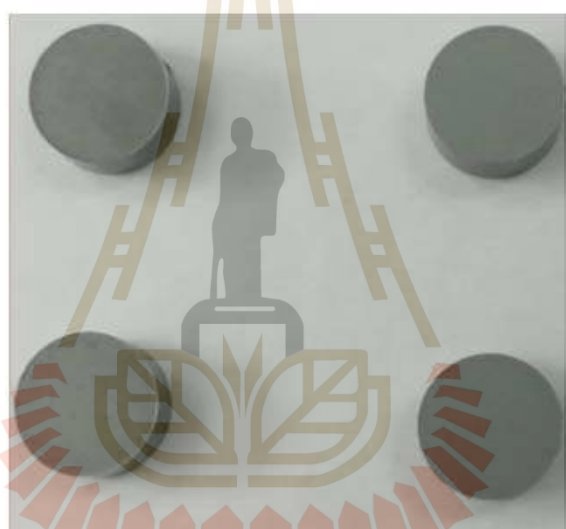
Excess Zn (at.% Zn)	Calcination Temp.	Holding time (hour)
0	Non cal., 300 °C, 400°C, 500°C	3
0, 5, 10, 15, 20	400 °C	3
10	400 °C	1, 3, 5
10	350 °C, 400 °C, 450 °C	3
10–14	400 °C	3
10–14	450 °C	3
10–14	500 °C	3

### 3.2 Fabrication of sintered $\beta$ -Zn<sub>4</sub>Sb<sub>3</sub> pellets

The synthesized  $\beta$ -Zn<sub>4</sub>Sb<sub>3</sub> powders were filled into a circular compression mould with a hole diameter of 1 cm. The mold was pressed to pressures of 500 MPa and 700 MPa, held for 15 minutes. The high compression pressure directly increased the density of the pellets, as shown in Table 5 (Lee and Lin, 2018). The maximum pressure of our hydraulic equipment is 700 MPa with 500 MPa used for comparison. As shows in Figure 37, the pressed  $\beta$ -Zn<sub>4</sub>Sb<sub>3</sub> pellets were sintered under Ar gas flow at a heating rate 1 °C/min until the target temperatures of 500 °C, 550 °C, 575 °C and 600 °C were reached. The pellets were held at these temperatures for 6 hours and then allowed to cool to room temperature. Finally, the successfully sintered  $\beta$ -Zn<sub>4</sub>Sb<sub>3</sub> pellets are depicted in Figure 38.

**Table 5** Pressure in compression process with calculation density of pressed  $\beta$ -Zn<sub>4</sub>Sb<sub>3</sub> pellets.

Materials	Diameter (cm)	Pressure (tons/MPa)	Thickness (cm)	Density % (g/cm <sup>3</sup> )
$\beta$ -Zn <sub>4</sub> Sb <sub>3</sub>	1.0	4.6/500	3.7	83
$\beta$ -Zn <sub>4</sub> Sb <sub>3</sub>	1.0	5.6/700	3.6	86



**500 MPa**

**700 MPa**

**Figure 37** The  $\beta$ -Zn<sub>4</sub>Sb<sub>3</sub> bulk pellets after were pressed at 500 and 700 MPa, respectively.

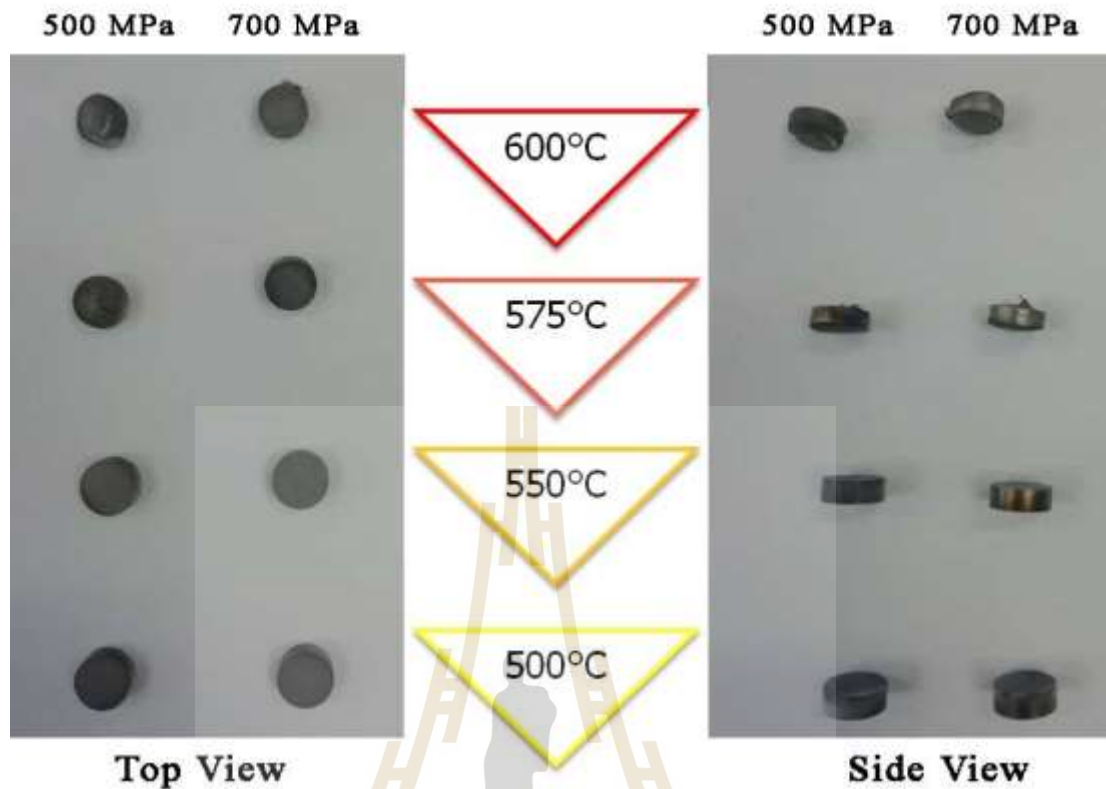


**Figure 38** The sintered  $\beta$ - $\text{Zn}_4\text{Sb}_3$  pellets after were sintered at 500 °C, 550 °C, 575 °C and 600 °C for 6 hours.

Based on the experimental results, the optimal condition for fabricating the sintered  $\beta$ - $\text{Zn}_4\text{Sb}_3$  pellets is a compression pressure of 700 MPa. The pellets sintered at compression pressure 700 MPa and a temperature of 550 °C showed good durability, although some swelling was observed at the rims. To refine the process further, sintering at 525 °C was also explored under the same 700 MPa compression. As a result, sintered  $\beta$ - $\text{Zn}_4\text{Sb}_3$  pellets were produced under condition of 700 MPa with sintering temperature at 500 °C, 525 °C and 550 °C.

### 3.3 Fabrication of test cells monolithic $\beta$ -Zn<sub>4</sub>Sb<sub>3</sub> /ZnO TEG module

Initially, the synthesized  $\beta$ -Zn<sub>4</sub>Sb<sub>3</sub> powders were filled into a square compression mold size 1x1 cm with a weight of 0.2 g and gently pressed at 100 MPa. Next commercial ZnO powders [99.9%, KemAus™] were added into the same mold for 0.2 g and gently pressed. The ZnO powders layers served as insulating plates due to the high electrical resistivity of ZnO materials (Jantrasee *et al.*, 2016). The soft compression process for the  $\beta$ -Zn<sub>4</sub>Sb<sub>3</sub> and ZnO powders was repeated twice. Afterward, the combined  $\beta$ -Zn<sub>4</sub>Sb<sub>3</sub> and ZnO powders was firmly hard pressed at 700 MPa for 15 minutes. The compression process is depicted in Figure 39. The pressed  $\beta$ -Zn<sub>4</sub>Sb<sub>3</sub>/ZnO pellets were sintered by gradually increasing the temperature at a rate of 1 °C/min under Ar gas flow until reaching 500 °C, and held for 6 hours. Following the sintering process, the pellets were coated with ethyl cyanoacetate to strengthen the multi-stack structure. Electrical wires were then used to connect the two  $\beta$ -Zn<sub>4</sub>Sb<sub>3</sub> layers in a zigzag configuration, forming a series circuit between the positive and negative terminals. To protect against lead solder melting during operation at 300 °C, the top and bottom of the test cells were covered with a cement filler. The above process was repeated using different initial weights of  $\beta$ -Zn<sub>4</sub>Sb<sub>3</sub> powders for 0.5 g, 1 g, 2 g and 4 g, to compare the open-circuit voltage, IV characteristics, and electrical power output, with the goal of identifying the optimal starting weight for the fabrication of monolithic multi-stack  $\beta$ -Zn<sub>4</sub>Sb<sub>3</sub>/ZnO TEG modules. Finally, the monolithic  $\beta$ -Zn<sub>4</sub>Sb<sub>3</sub>/ZnO TEG test cells were successfully fabricated, as shown in Figure 40.

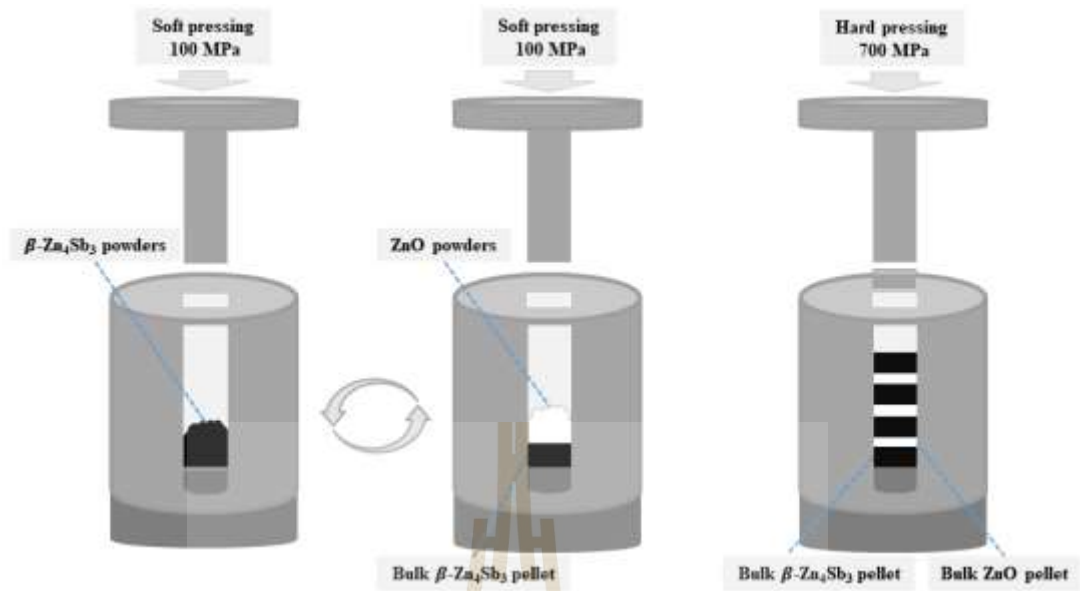


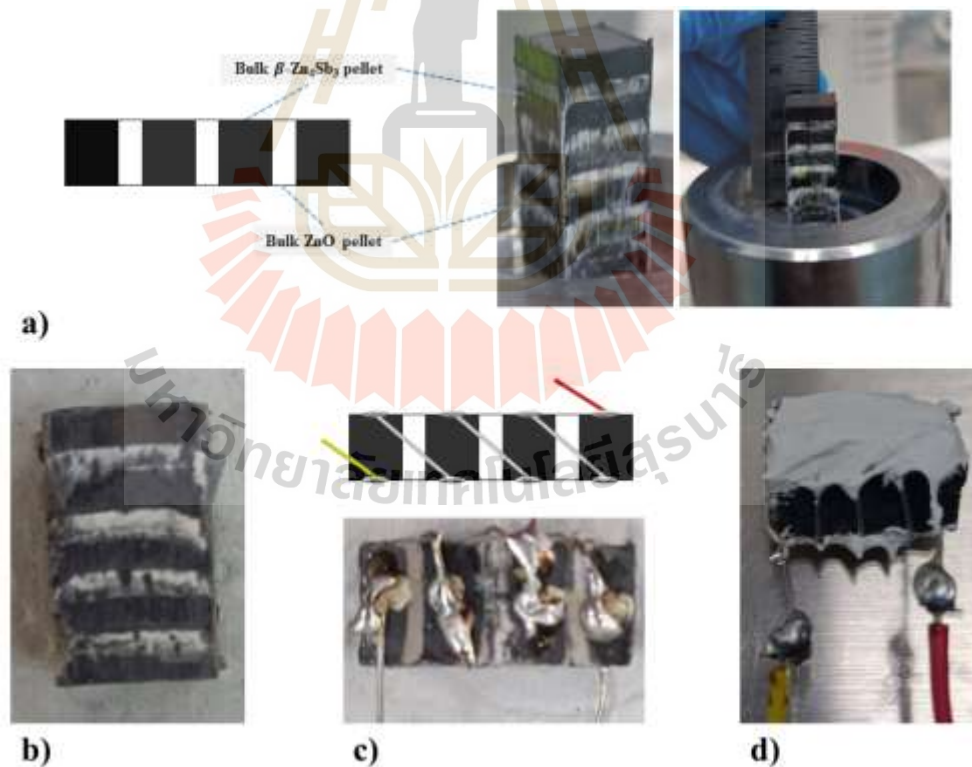
Figure 39 The cyclical compression process for preparing  $\beta$ -Zn<sub>4</sub>Sb<sub>3</sub>/ZnO pellets.



Figure 40 The test cells of monolithic  $\beta$ -Zn<sub>4</sub>Sb<sub>3</sub>/ZnO TEGs versus weight size of  $\beta$ -Zn<sub>4</sub>Sb<sub>3</sub> pellets part.

### 3.4 Fabrication of monolithic multi-stack $\beta$ -Zn<sub>4</sub>Sb<sub>3</sub>/ZnO TEG module

This fabrication process is similar to that of the test cells, but with the soft compression method of  $\beta$ -Zn<sub>4</sub>Sb<sub>3</sub> powders and ZnO powders repeated multiple times. Afterward, the multi-stack layers of multi-stack of  $\beta$ -Zn<sub>4</sub>Sb<sub>3</sub> and ZnO powders was firmly hard pressed at 700 MPa for 15 minutes. The compression processes is depicted in Figure 39. The pressed multi-stacks  $\beta$ -Zn<sub>4</sub>Sb<sub>3</sub>/ZnO pellets were sintered by gradually increasing the temperature at a rate of 1 °C/min under Ar gas flow until reaching 500 °C, and held for 6 hours. After sintering, the multi-stacks  $\beta$ -Zn<sub>4</sub>Sb<sub>3</sub>/ZnO pellets were coated by ethyl cyanoacetate to enhance its strength. Then the  $\beta$ -Zn<sub>4</sub>Sb<sub>3</sub> layers of the multi-stack pellet were then connected with electrical wires in a zigzag configuration to form a series circuit between the positive and negative terminals. To protect against lead solder melting during operation at 300 °C, the top and bottom of the multi-stack  $\beta$ -Zn<sub>4</sub>Sb<sub>3</sub>/ZnO TEGs were coated with a cement filler. Finally, the monolithic multi-stack  $\beta$ -Zn<sub>4</sub>Sb<sub>3</sub>/ZnO TEGs were successfully fabricated, as shows in Figure 41.



**Figure 41** Fabrication processes of monolithic  $\beta$ -Zn<sub>4</sub>Sb<sub>3</sub>/ZnO TEGs: a) compressed multi-stacks  $\beta$ -Zn<sub>4</sub>Sb<sub>3</sub>/ZnO pellet, b) sintered multi-stacks  $\beta$ -Zn<sub>4</sub>Sb<sub>3</sub>/ZnO pellet, c) connected electrical wire with zigzags connection of monolithic  $\beta$ -Zn<sub>4</sub>Sb<sub>3</sub>/ZnO TEGs, and d) monolithic  $\beta$ -Zn<sub>4</sub>Sb<sub>3</sub> TEGs was plastered with cement filler.

### 3.5 Materials characterization

In this work, the  $\beta$ -Zn<sub>4</sub>Sb<sub>3</sub> sample was analyzed crystallite structure, local oxidation of component elements, and the binding energy of materials elements. The details of the technical characterizations and methods are outlined in the following subtopics.

#### 3.5.1 X-ray diffraction

The crystallite structure of  $\beta$ -Zn<sub>4</sub>Sb<sub>3</sub> was investigated using X-ray diffraction technique (D8-Bruker). The X-ray diffraction technique (D8-Bruker) is shown in Figure 43. The XRD technique was employed to determine the crystallite structure pattern of  $\beta$ -Zn<sub>4</sub>Sb<sub>3</sub>, and the resulting diffraction patterns were compared with Mozharivskyj's model (Mozharivskyj *et al.*, 2006). However, the X-ray diffraction for all samples revealed the presence of a secondary phase. The fundamental principle of X-ray diffraction is based on Bragg's law scattering, which describes how X-rays interfere through constructive and destructive interference with each other beam, depending on the diffraction angles. This correlation are explained by following equation.

$$2d \sin \theta = n\lambda \quad (113)$$

Where  $d$  is space between crystallite plan,  $\theta$  is an angle of incident X-ray beam,  $\lambda$  is X-ray wavelength, which the wavelength is 0.15406 nm, and  $n$  is the order of the X-ray interference beam, along with destruction and construction.

the intensity and width of the X-ray diffraction patterns can be used to calculate the crystallite sizes of the samples. However, this study did not focus on crystallite size. Crystallite sizes are typically calculated using the Debye-Scherrer equation, as shows in equations (114).

$$D = \frac{k\lambda}{\beta \cos \theta} \quad (114)$$

Where;

$D$  is a crystallite size

$k$  is a spherical factor, which the factor is  $k \approx 0.9$

$\beta$  is a full width half maximum (FWHM) intensity of x-ray diffraction peaks.

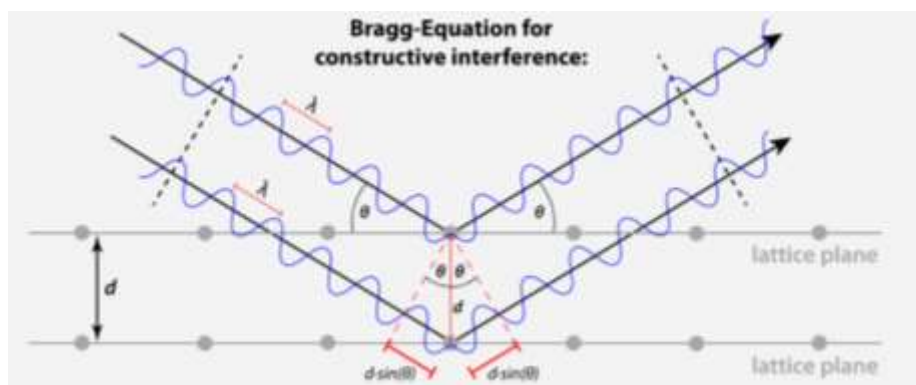


Figure 42 Shows x-ray incident and diffraction, according to Bragg's law ([www.didaktik.physik.uni-muenchen.de/elektronenbahnen/en/index.php](http://www.didaktik.physik.uni-muenchen.de/elektronenbahnen/en/index.php)).



Figure 43 Shows X-ray diffraction machine, D8-Bruker, SUT.

### 3.5.2 X-ray absorption spectroscopy

X-ray absorption spectroscopy (XAS) is a technique used to study the near-edge structure of materials elements by analyzing X-ray absorption near-edge structure (XANES) spectra. This method investigates the ionization energy for exciting core electrons. The transmission intensities of the X-ray beam are measured to determine the ionization energy of core electrons, which reveals the oxidation state of local elements within the sample. Each electron orbital and absorption edge absorb specific X-ray energies, as illustrated in Figure 44. Therefore, the X-ray absorption spectra of the electron orbitals provide insight into the material's structure. Typically,

the X-ray absorption measurement are conducted in transmission mode for bulk samples, as shown in Figure 45. The intensity of the transmitted X-ray beam relative to the incident X-ray beam intensity is expressed as a function of the X-ray absorption coefficient  $\mu(E)$ , represented by the following (115).

$$\mu(E)t = -\ln \frac{I}{I_0} \quad (115)$$

Where;

$\mu_E$  is absorption coefficient.

$I$  is x-ray transmission intensity

$I_0$  is x-ray incident intensity.

$t$  is sample thickness.

The XANES measurement technique as transmission mode is shown in Figure 45.

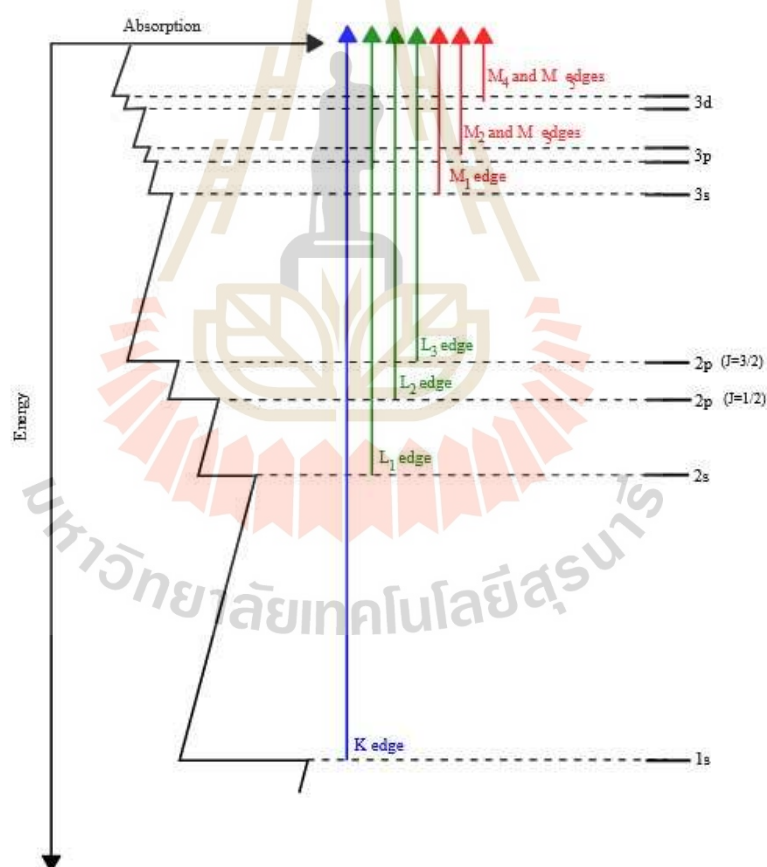


**Figure 44** Illustration of a x-ray absorption energies of K edge, L edges and M edges (Chem.libretexts, 2000).

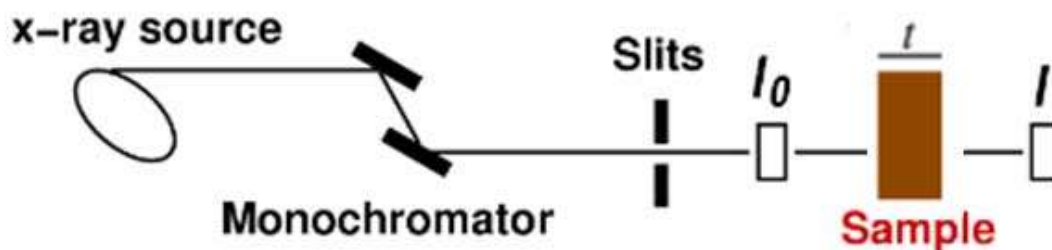


Figure 45 Illustration of x-ray absorption transmission mode (Mit.edu, 2004).

### 3.6 Thermoelectric properties

The thermoelectric properties of materials include the Seebeck coefficient, electrical conductivity, electrical power factor, and thermal conductivity. In this research, the commercial Linseis LSR-3 equipment was used to measure these properties. This equipment operates based on the principle of thermoelectric measurement (Goldsmid, 2010), where it measures the voltage ( $V$ ) as a function of the temperature gradient across the sample, as you know Figure 46.

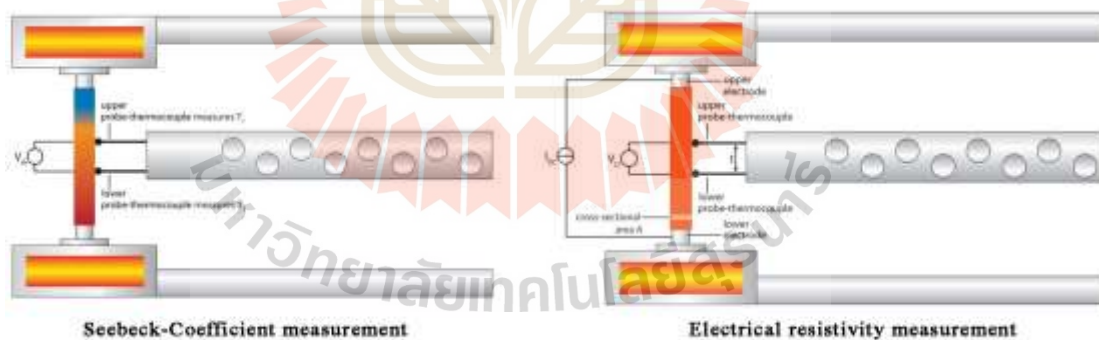


Figure 46 Illustration of Seebeck coefficient and electrical resistivity (Linseis, 2024).



Figure 47 LINSEIS LSR-3 Seebeck type resistivity measurement system.

### 3.7 Module evaluation

Due to limitations of commercial equipment for evaluating IV-curves and electrical output power curves of the TEG modules, a custom-built heating/cooling system with IV measurement capabilities was developed. The system is controlled by a temperature controller board, while the IV-curve was measured using a commercial current/voltage meter and a potentiometer. The setup is illustrated in Figure 48.

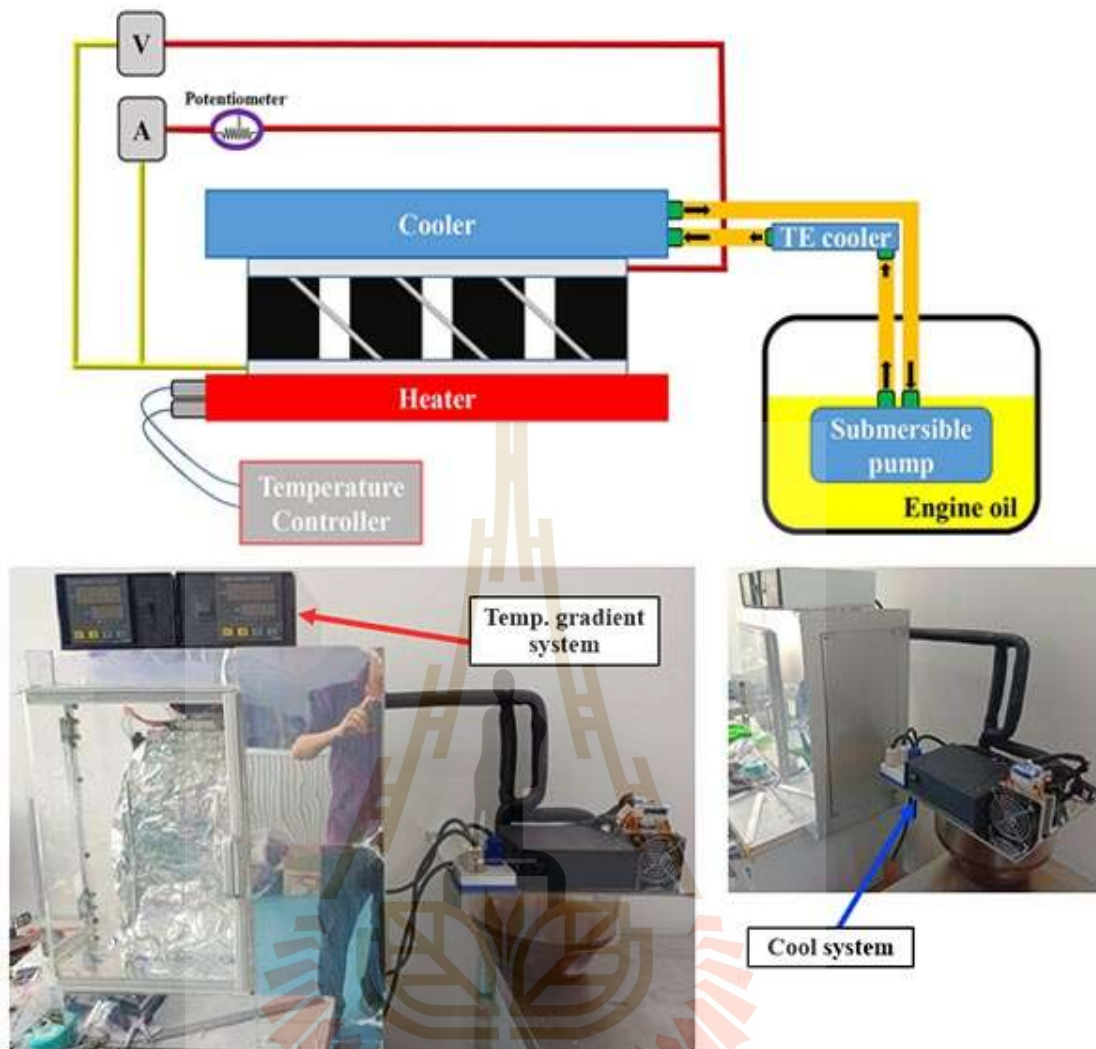


Figure 48 The self-made heating/cooling system with IV measurement capabilities.

## CHAPTER IV

### RESULTS AND DISCUSSION

Chapter IV presents the complete experimental results, including the structural characterization of the synthesized  $\beta$ -Zn<sub>4</sub>Sb<sub>3</sub> powders and the thermoelectric properties of sintered  $\beta$ -Zn<sub>4</sub>Sb<sub>3</sub> pellets. This chapter also includes the analysis and evaluation of monolithic  $\beta$ -Zn<sub>4</sub>Sb<sub>3</sub>/ZnO TEG modules. The results are presented according to scientific hypotheses and specific theories. This chapter is divided into five sections: X-ray diffraction, X-ray absorption, thermoelectric properties, module analysis and evaluation, respectively.

#### 4.1 X-ray diffraction

According to the synthesis of  $\beta$ -Zn<sub>4</sub>Sb<sub>3</sub> powders, the process synthesis of  $\beta$ -Zn<sub>4</sub>Sb<sub>3</sub> powders were investigated using comparative X-ray diffraction (XRD) pattern of the synthesized  $\beta$ -Zn<sub>4</sub>Sb<sub>3</sub> powders, along with calculated XRD pattern of  $\beta$ -Zn<sub>4</sub>Sb<sub>3</sub> of Mayer's model. Initially, the optimal calcination temperature for the synthesis of  $\beta$ -Zn<sub>4</sub>Sb<sub>3</sub> powders without excess Zn powder was determined by comparing temperatures of non-calcined, 300 °C, 400 °C and 500 °C, and held for 3 hours. The experimental results indicate that the optimal calcination temperature for synthesis  $\beta$ -Zn<sub>4</sub>Sb<sub>3</sub> powders without excessing of Zn powder is condition of calcination temperature at 400 °C, as it produced essential 3 peaks around  $2\theta \sim 25^\circ$  in the XRD pattern of  $\beta$ -Zn<sub>4</sub>Sb<sub>3</sub> materials. Comparative XRD patterns of the synthesized  $\beta$ -Zn<sub>4</sub>Sb<sub>3</sub> powders without excessing of Zn powder for calcination temperature of non-calcined, 300 °C, 400 °C and 500 °C are shown in Figure 49.

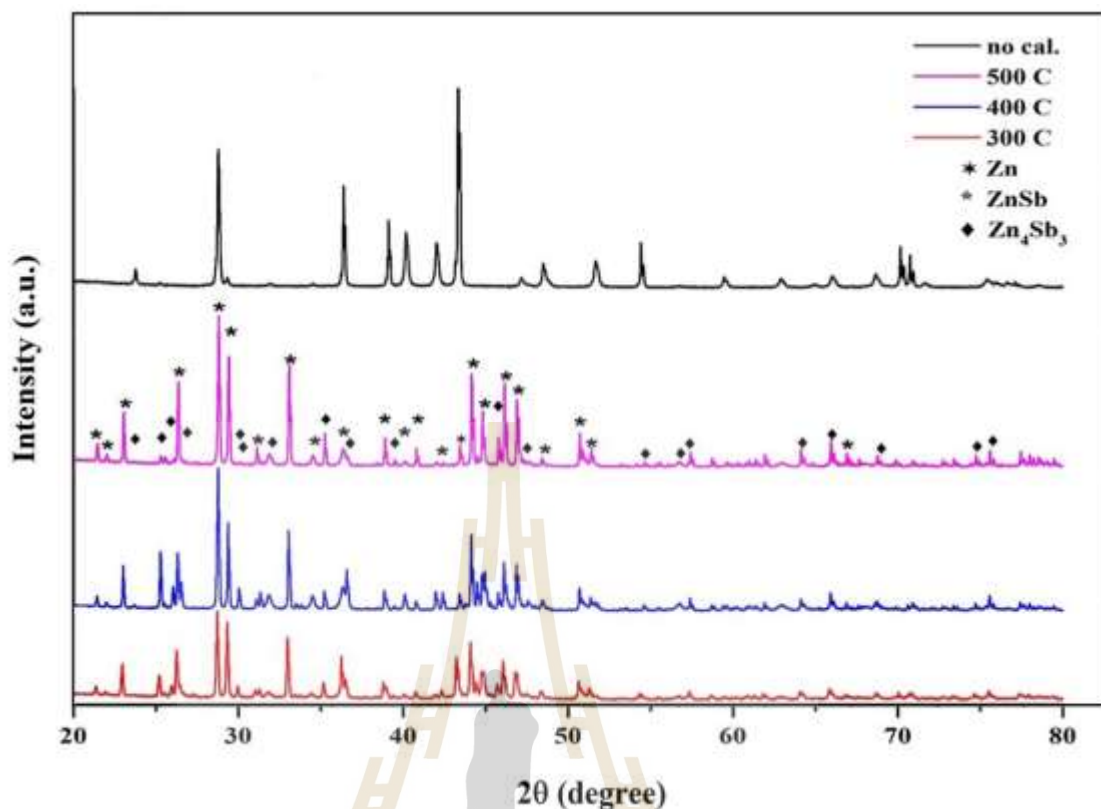


**Figure 49** X-ray diffraction patterns of the synthesized  $\beta$ - $Zn_4Sb_3$  powders under conditions of calcination temperature non-calcined, 300 °C, 400 °C and 500 °C without excess of Zn.

The optimal calcination temperature for synthesizing  $\beta$ - $Zn_4Sb_3$  powders without excessing of Zn powder is 400 °C. To investigate the effects of varying amounts of excess Zn, different conditions were tested by adding 0, 5, 10, 15 and 20 at.% Zn to the premixed powders. The XRD pattern results indicate that the optimal amount of excess Zn powder is 10 at.% because the XRD pattern of the synthesized  $\beta$ - $Zn_4Sb_3$  powders with this addition closely resembles of Mayer's model. The comparison XRD pattern of the synthesized  $\beta$ - $Zn_4Sb_3$  powders under varying excessed Zn conditions at a calcination temperature of 400 °C for 3 hours are shown in Figure 50.

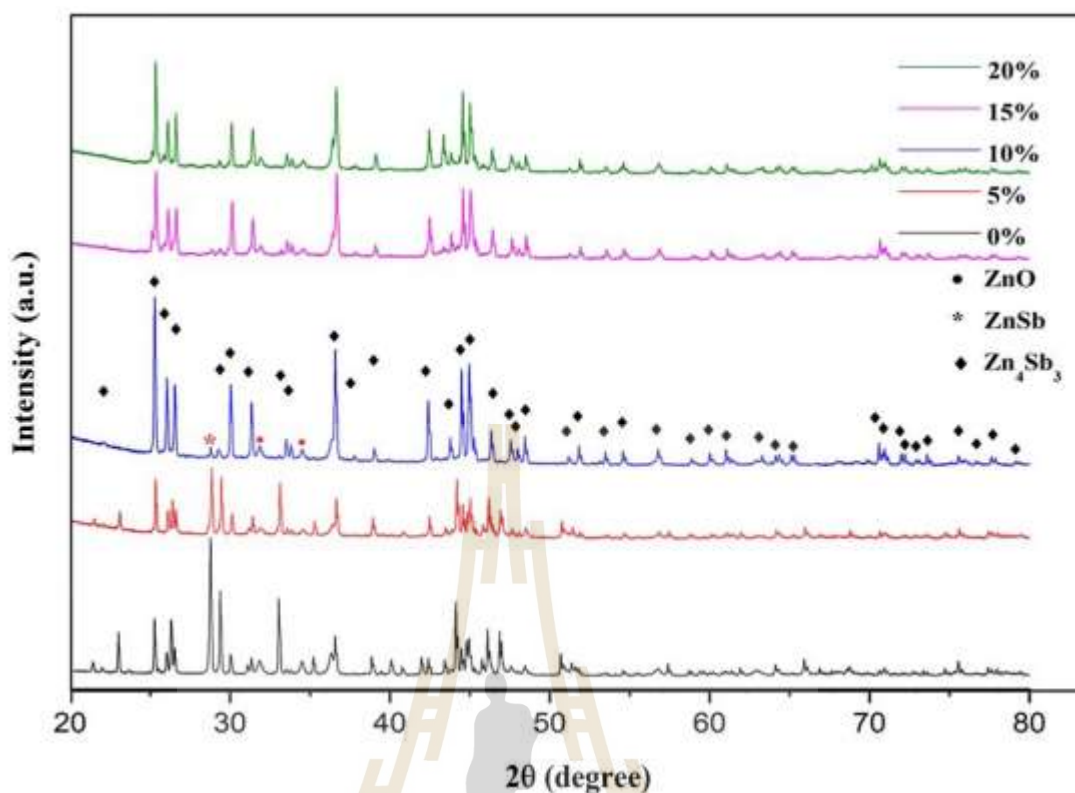


**Figure 50** The comparison XRD pattern of the synthesized  $\beta$ - $\text{Zn}_4\text{Sb}_3$  powders under varying excess Zn condition via calcination temperature 400 °C and held for 3 hours.

The optimal conditions for synthesizing  $\beta$ - $\text{Zn}_4\text{Sb}_3$  powders is usage excess of 10 at.% Zn powder and calcination at 400 °C for 3 hours. The calcination holding time was then for 1, 3 and 5 hours. The XRD pattern results show that calcination holding time for 3 hours produces the best XRD pattern for the synthesized  $\beta$ - $\text{Zn}_4\text{Sb}_3$  powders, closely matching XRD pattern of  $\beta$ - $\text{Zn}_4\text{Sb}_3$  of Mayer's model and outperforming other conditions. Although the XRD pattern under calcination holding time for 3 hours resembles under calcination holding time for 3 hours. Indeed, the XRD pattern of the synthesized  $\beta$ - $\text{Zn}_4\text{Sb}$  powders under calcination holding time for 3 hours has clearer peaks and higher intensity. The comparison XRD pattern of the synthesized  $\beta$ - $\text{Zn}_4\text{Sb}_3$  powders under varying holding time, using excess Zn of 10 at.% and calcination temperature of 400 °C are shown in Figure 51.

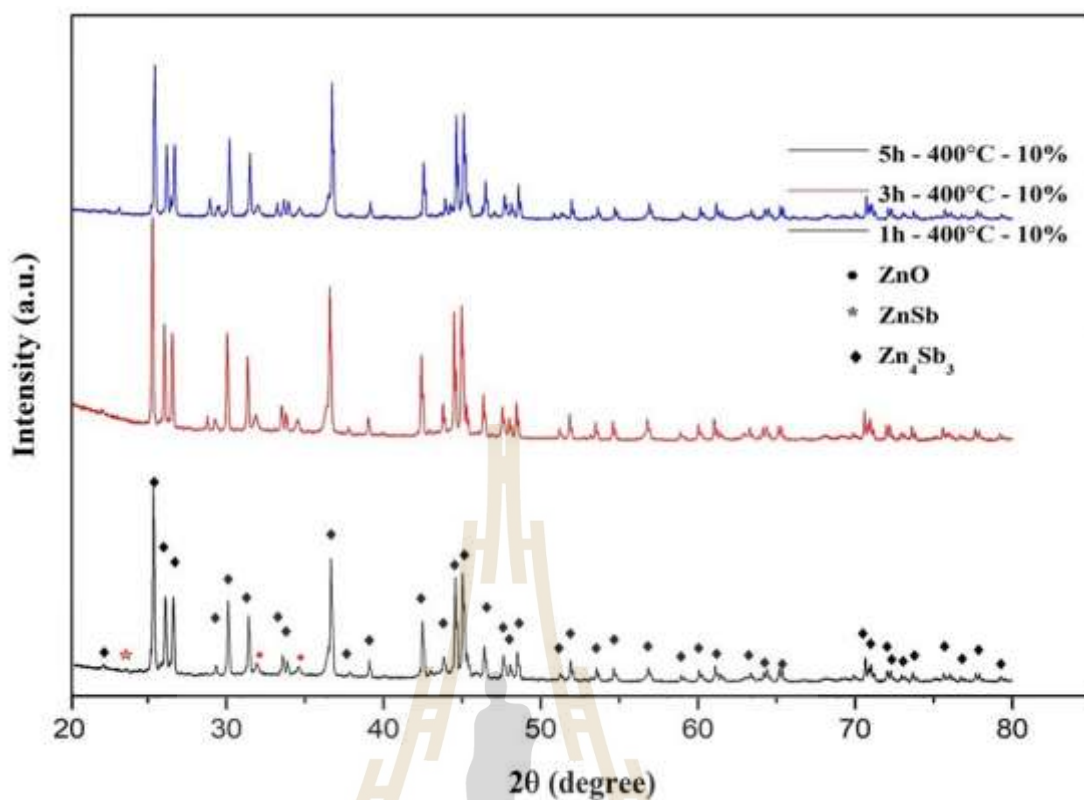


**Figure 51** XRD pattern of varying holding time via excessing Zn of 10 at.% Zn and calcination temperature 400 °C.

Currently, the optimal conditions for synthesizing  $\beta$ - $\text{Zn}_4\text{Sb}_3$  powders is excess 10 at.% Zn and calcination temperature of 400 °C for 3 hours. To further refine these conditions, calcination temperature 350 °C, 400 °C and 450 °C were investigated. The XRD pattern results indicate that a calcination temperature condition of 450 °C yields a better XRD pattern for  $\beta$ - $\text{Zn}_4\text{Sb}_3$  materials better compared to 400 °C, due to reduced impurity phases of ZnSb, Zn and Sb. The comparison of XRD pattern for the synthesized  $\beta$ - $\text{Zn}_4\text{Sb}_3$  powders under conditions of calcination temperature at 350 °C, 400 °C and 450 °C is shown in Figure 52.

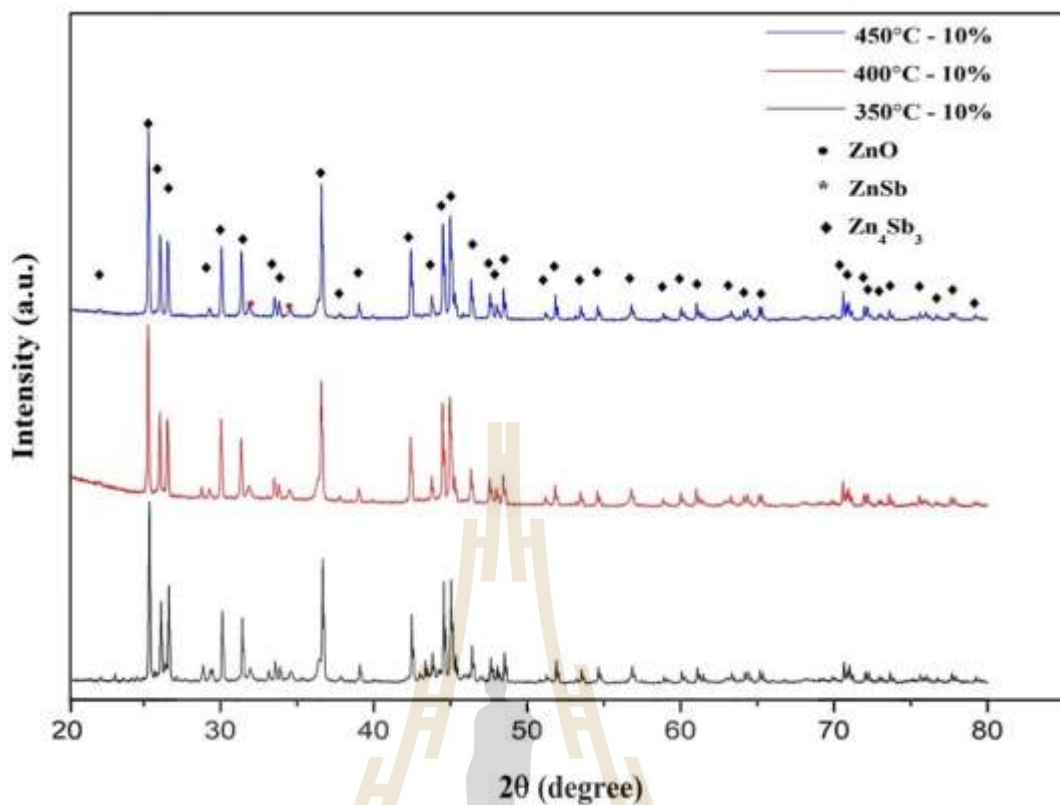


**Figure 52** The comparison XRD pattern of the synthesized  $\beta$ - $\text{Zn}_4\text{Sb}_3$  powders under varying calcination temperature at 350 °C, 400 °C and 450 °C via adding 10 at.% Zn and calcination holding time for 3 hour.

Under the current conditions, the optimal synthesis for  $\beta$ - $\text{Zn}_4\text{Sb}_3$  powders involves using excess Zn powders 10 at.% and calculating at 450 °C for 3 hours. To further refine, conditions of excess Zn powders as 10, 11, 12, 13, 14 at.% were subjected to the same calcination process. As depicted in Figure 53, the XRD diffraction pattern of the synthesized  $\beta$ - $\text{Zn}_4\text{Sb}_3$  powders under 12 at.% Zn rich at calcination temperature at 450 °C for 3 hours produced the best results, with minimal impurity phases of ZnSb, Zn and Sb.

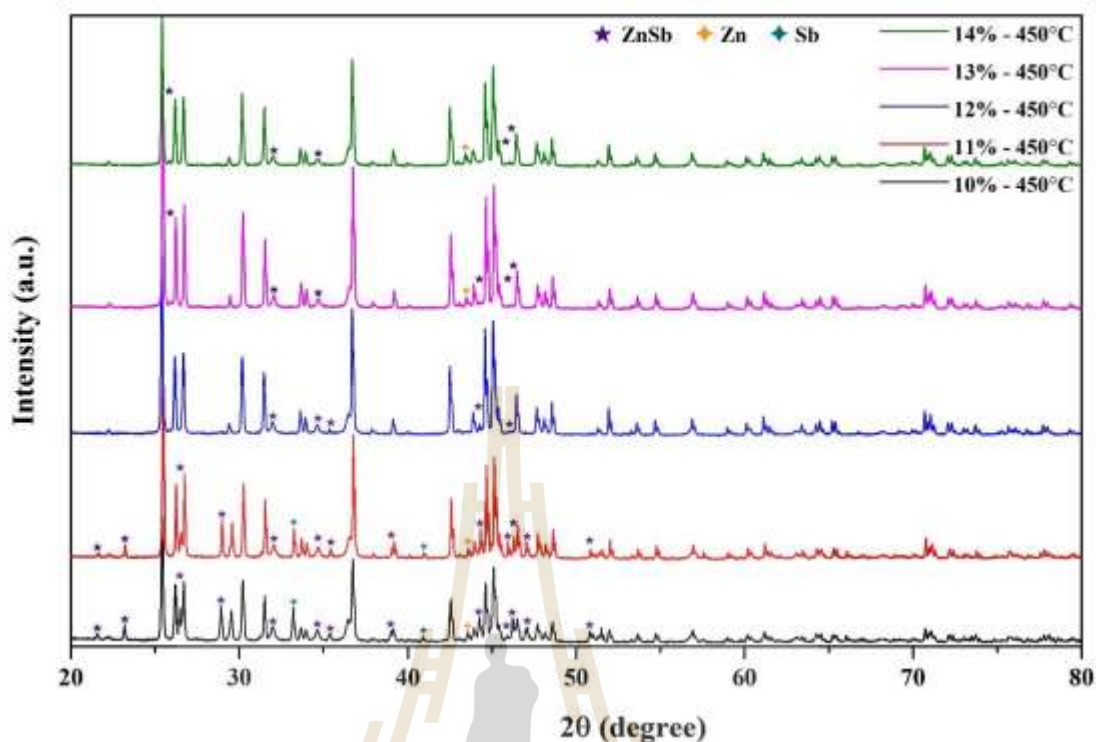


**Figure 53** Comparison XRD pattern of the synthesized  $\beta$ - $Zn_4Sb_3$  powders under excessing Zn for 10, 11, 12, 13 and 14 at.% Zn and calcination at 450 °C for 3 hours.

Additionally, calcination temperature of 400 °C and 425 °C were investigated with excess Zn powders as 10, 11, 12, 13, 14 at.%. As shown in Figure 54 and Figure 55, the XRD diffraction pattern of the synthesized  $\beta$ - $Zn_4Sb_3$  powders under calcination temperature at 400 °C and 425 °C with excess Zn powders as 10, 11, 12, 13, 14 at.% Zn, indicate that the best results for both 400 °C and 425 °C were obtained with excess Zn powders 13 at.%, as depict in Figure 54 and Figure 55. Finally, Figure 56 compares the XRD patterns for the best synthesis conditions: 400 °C with 13 at.% Zn, 425 °C with 13 at.% Zn and 450 °C with 12 at.% Zn, all with a holding time of 3 hours. Among these, the optimal condition for synthesizing  $\beta$ - $Zn_4Sb_3$  powders is excess Zn powders 12 at.% under calcination temperature 450 °C for 3 hours, as it results in the least amount of impurity phases

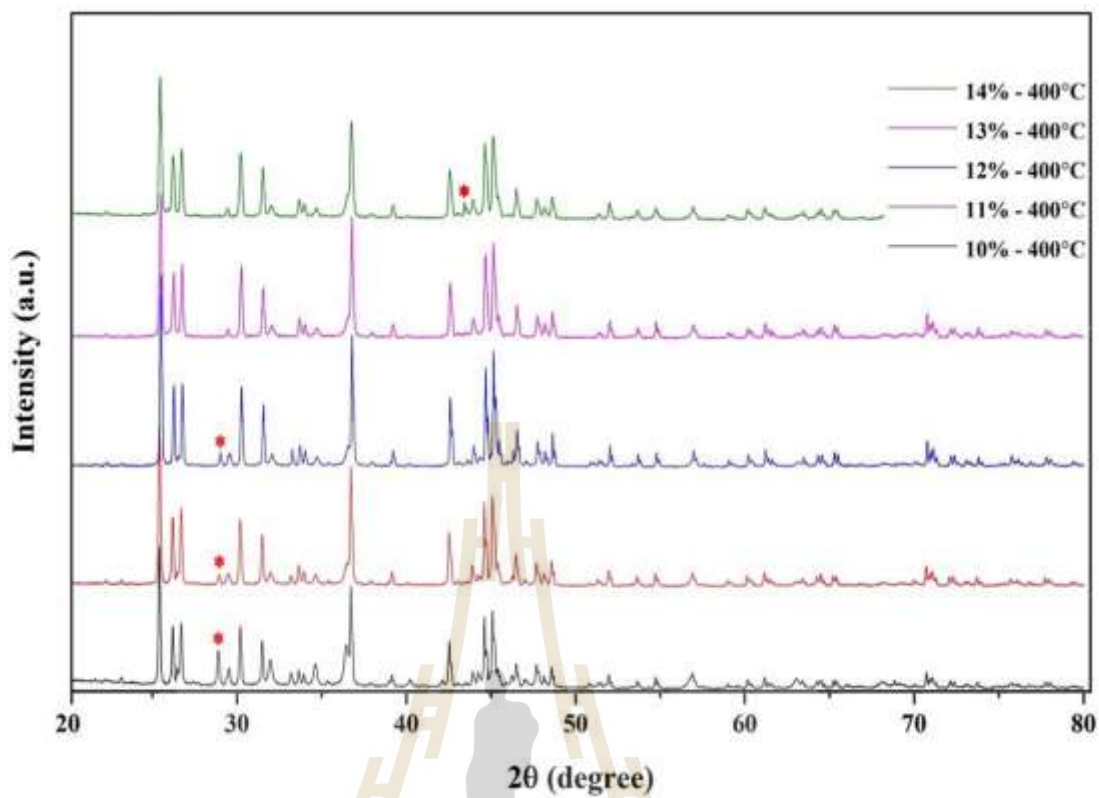


Figure 54 Comparison XRD pattern of the synthesized  $\beta$ - $\text{Zn}_4\text{Sb}_3$  powders under excessing Zn for 10, 11, 12, 13 and 14 at.% Zn and calcination at 400 °C for 3 hours.

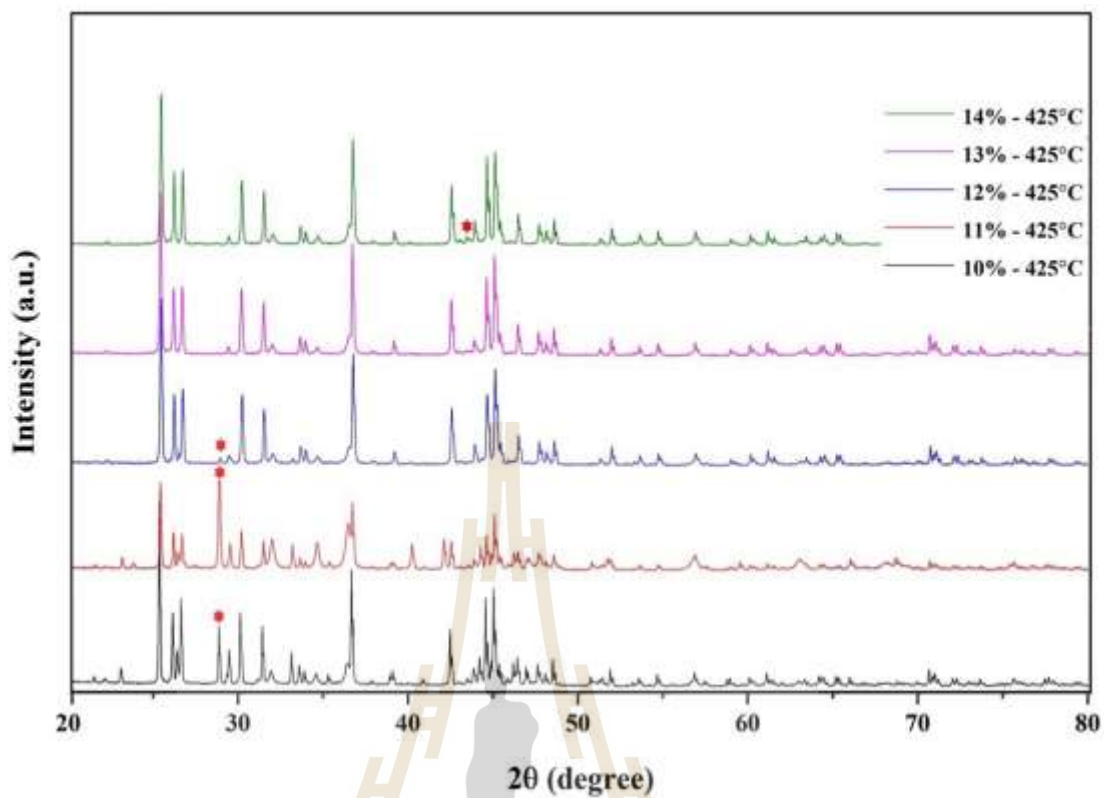
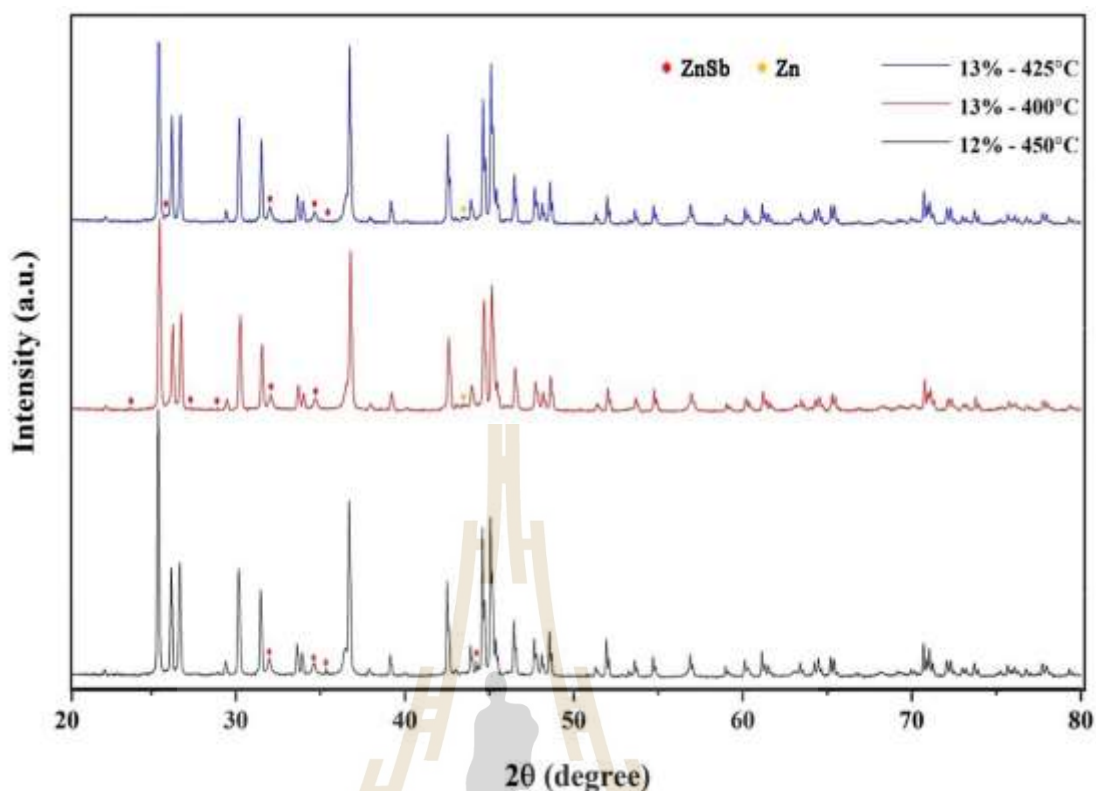


Figure 55 Comparison XRD pattern of the synthesized  $\beta$ - $\text{Zn}_4\text{Sb}_3$  powders under excessing Zn for 10, 11, 12, 13 and 14 at.% Zn and calcination at 425 °C for 3 hours.



**Figure 56** Comparison of the synthesis series of excessing Zn for 10, 11, 12, 13, 14 and 15 at.% Zn and calcination at 400 °C, 425 °C, 450 °C for 3 hours.

#### 4.2 X-ray absorption spectroscopy

The purest  $\beta$ -Zn<sub>4</sub>Sb<sub>3</sub>, synthesized with excessing 12 at.% Zn rich at a calcination temperature of 450 °C for 3 hours, were investigated using x-rays absorption near-edge structure (XANES) spectra at the Zn K-edge and Sb L-edges. This analysis was conducted at SUT-NANOTEC-SLRI XAS beamline (BL 5.2) using synchrotron. The exciting core electrons as oxidation states of Zn atoms in the synthesized  $\beta$ -Zn<sub>4</sub>Sb<sub>3</sub> powder were measured at level K (Zn K-edge) across energy range 9,550–9800 eV, as shown in Figure 57. The normalized XANES spectrum of the Zn K-edge reveals a rising energy edge range of 9,640–9,667, with the main absorption edge at 9,659 eV. Then, the derivation of normalized XANES spectrum of the Zn K-edge of the synthesized  $\beta$ -Zn<sub>4</sub>Sb<sub>3</sub> powders further confirms the main absorption edge at 9,659 eV, as expressed in Figure 58.

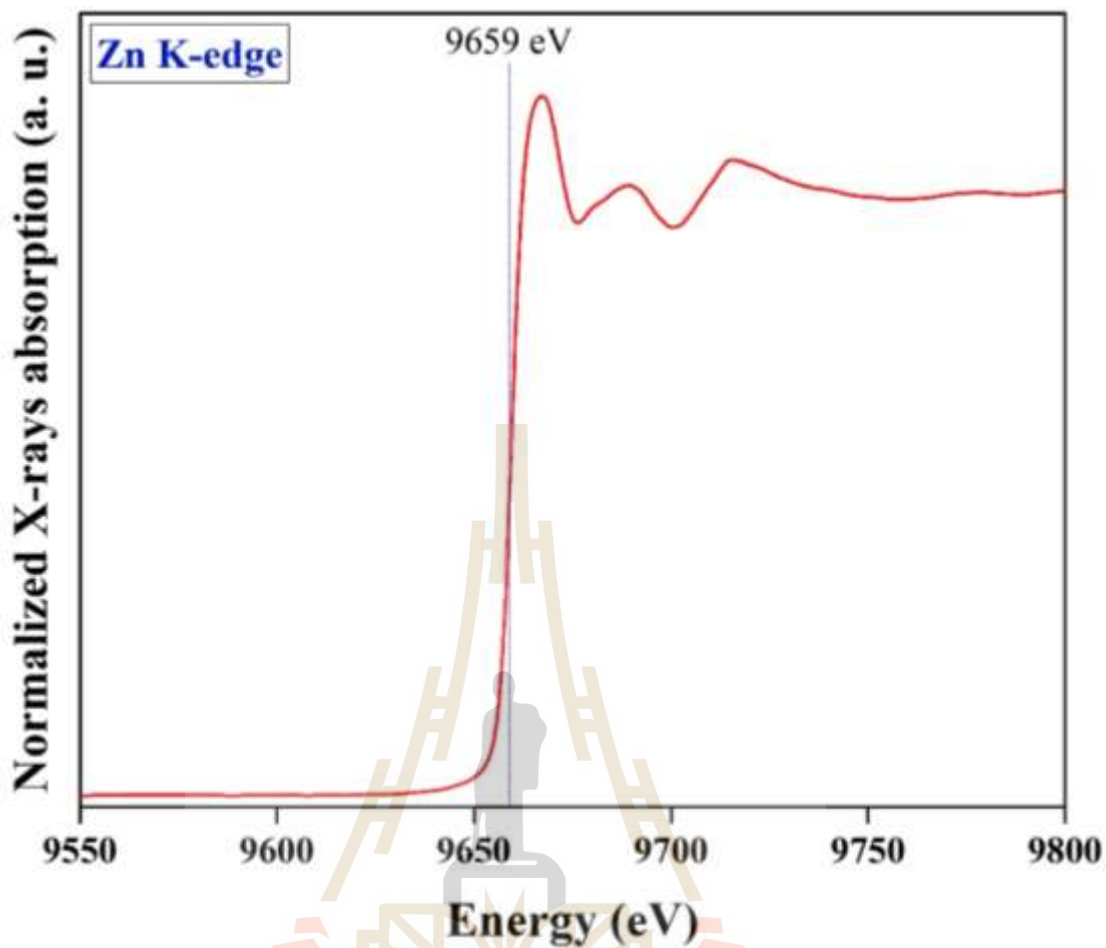


Figure 57 Normalized XANES of Zn K-edge of the high pure synthesized  $\beta$ - $Zn_4Sb_3$  powder.

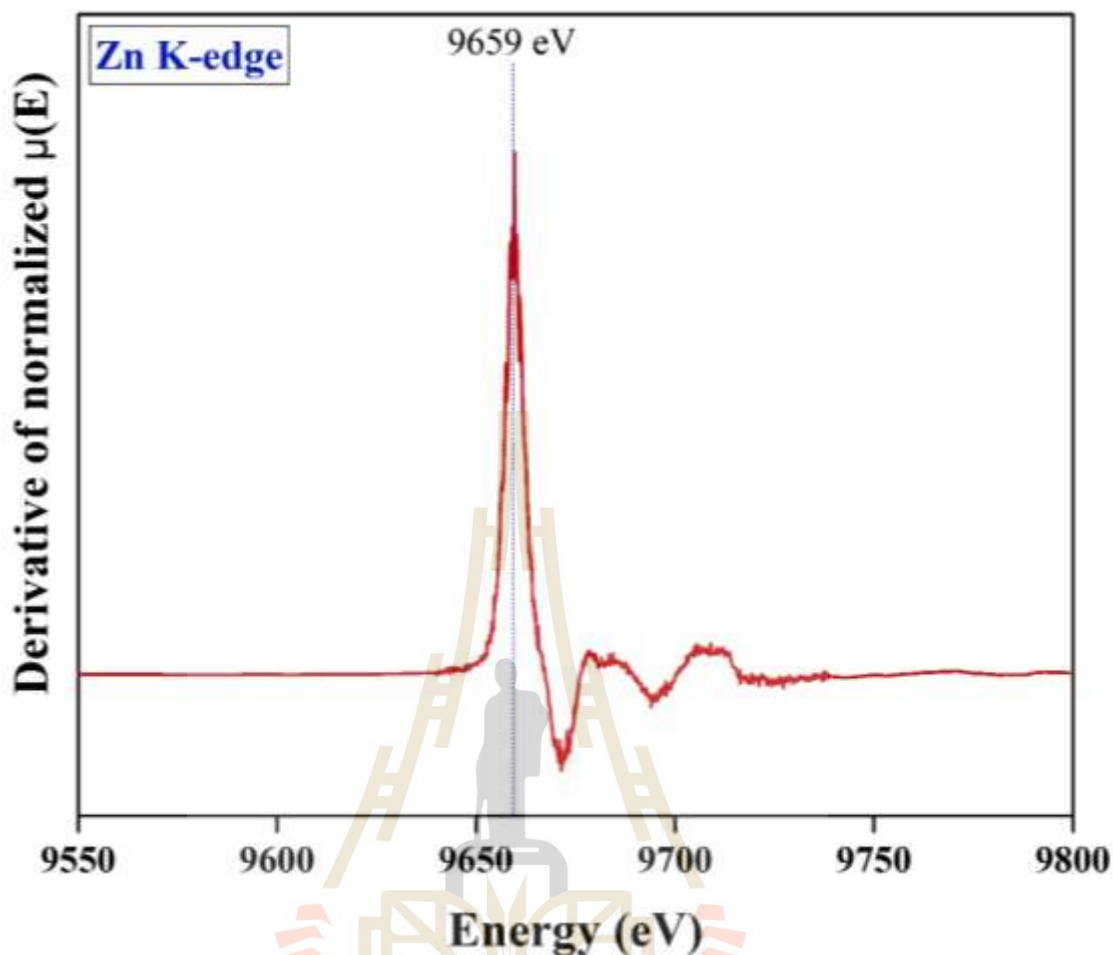


Figure 58 Derivative normalized XANES of Zn K-edge of the high pure synthesized  $\beta$ - $\text{Zn}_4\text{Sb}_3$  powder.

The exciting core electrons as oxidation states of Sb atoms in the synthesized  $\beta$ - $\text{Zn}_4\text{Sb}_3$  powders were measured at level L (Sb L-edges) across energy range 4,000–4,750 eV, as shown in Figure 59. The normalized XANES spectrum for the Sb L3, L2 and L1-edge reveal rising energy edges range of 4,100–4,150 eV, 4,377–4,397 eV and 4,690–4,700 eV, with the main absorption edges at 4,132 eV, 4,380 eV and 4,698 eV, respectively. Then, the derivation of normalized XANES spectrum for the Sb L3, L2 and L1-edge of the synthesized  $\beta$ - $\text{Zn}_4\text{Sb}_3$  powders further confirms these main absorption, as shown in Figure 60.

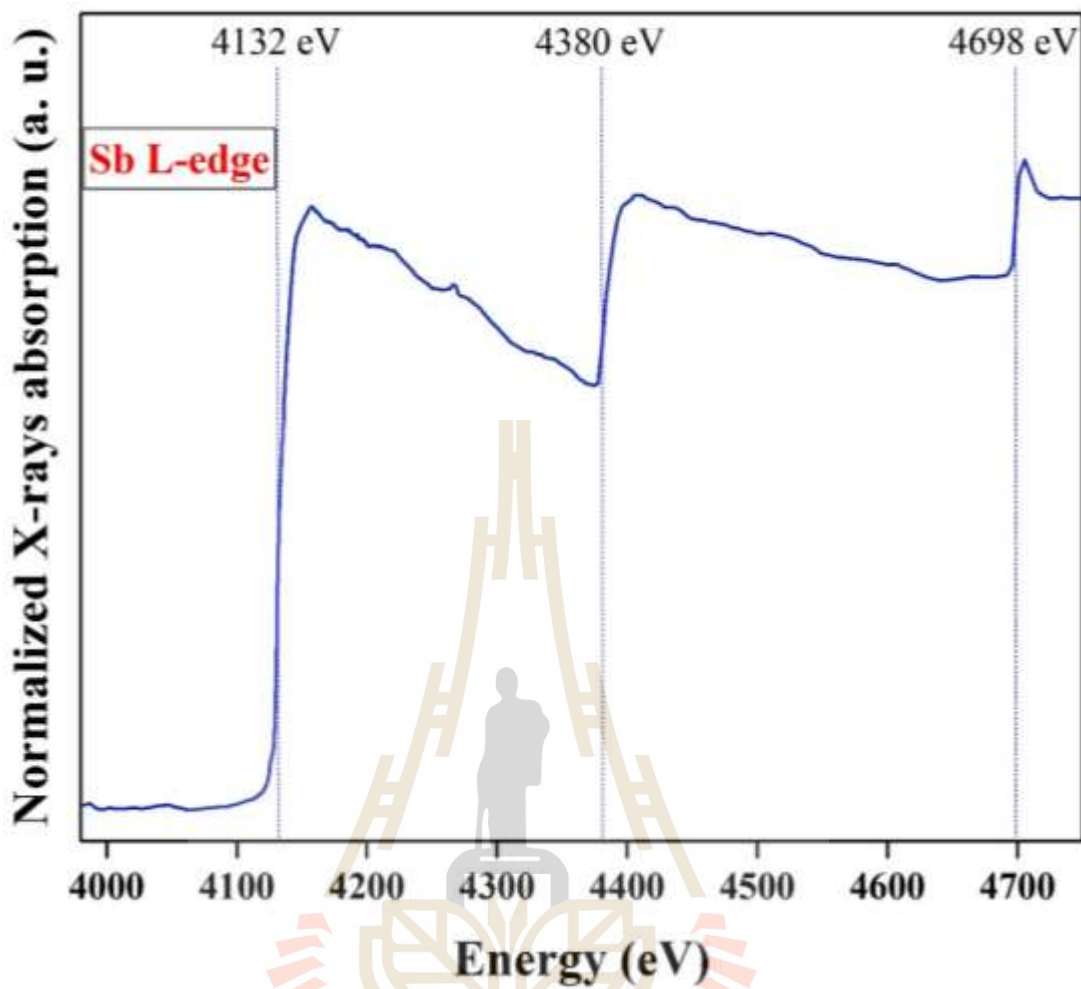
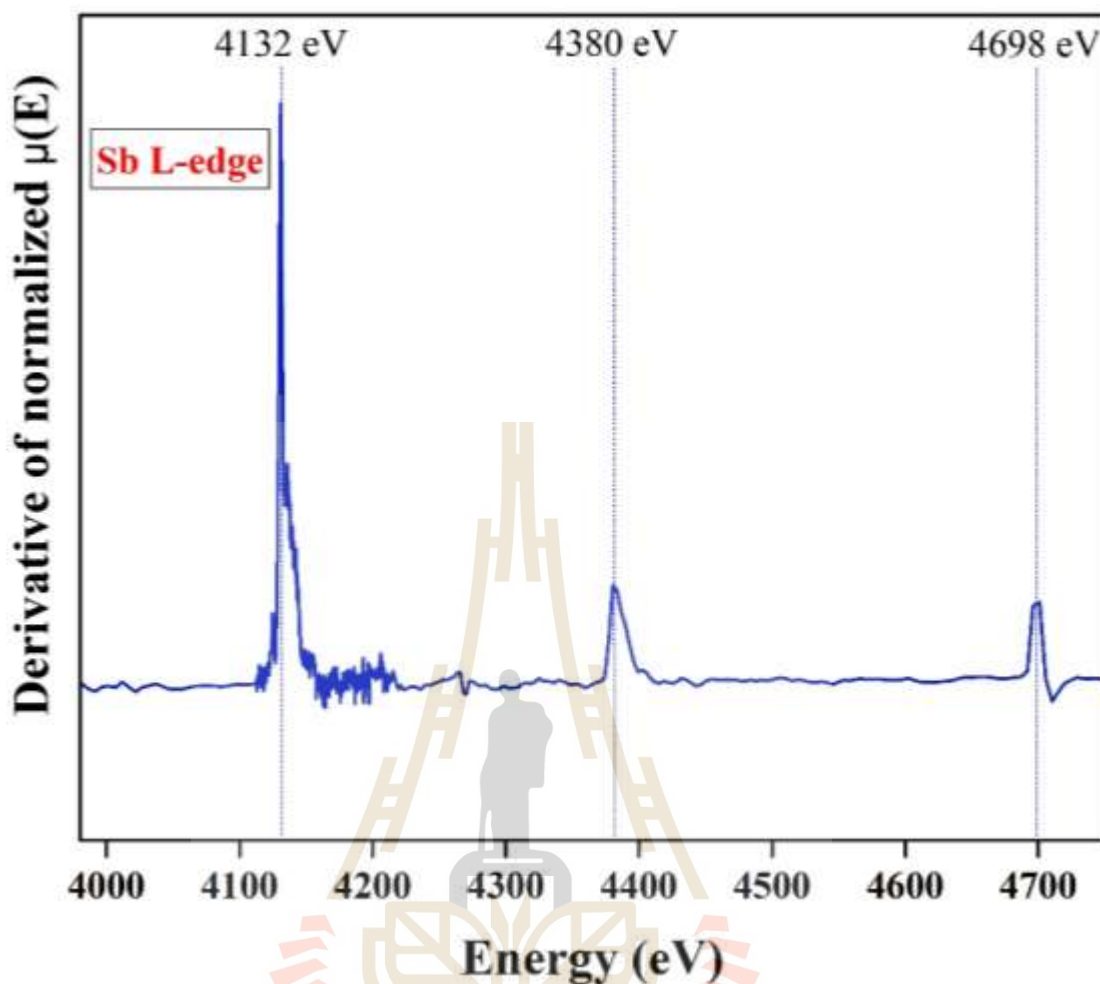


Figure 59 Normalized XANES of Sb L3, L2 and L1-edge of the high pure synthesized  $\beta$ - $\text{Zn}_4\text{Sb}_3$  powder.



**Figure 60** Derivative normalized XANES of Sb L3, L2 and L1-edge of the high pure synthesized  $\beta$ -Zn<sub>4</sub>Sb<sub>3</sub> powder.

Originally,  $\beta$ -Zn<sub>4</sub>Sb<sub>3</sub> is an alloy material with characteristic ionization energies of exciting core electrons as oxidation states of Zn<sup>0</sup> and Sb<sup>0</sup>. Based on the experimental results from the normalized XANES and derivative normalized XANES spectra of the Zn K-edge and Sb L-edges for the high pure synthesized  $\beta$ -Zn<sub>4</sub>Sb<sub>3</sub> powders, it is confirmed that the ionization energy of exciting core electrons as oxidation state correspond to the Zn<sup>0</sup> and Sb<sup>0</sup> oxidation states. This finding aligns with the absorption edge database of the Hephaestus program (Ravel and Newville, 2005) and further confirms that the synthesized  $\beta$ -Zn<sub>4</sub>Sb<sub>3</sub> powders is devoid of existing ionic bonding and oxides.

### 4.3 Thermoelectric properties

The high pure synthesized  $\beta$ -Zn<sub>4</sub>Sb<sub>3</sub> powder were used to fabricate the sintered  $\beta$ -Zn<sub>4</sub>Sb<sub>3</sub> pellets. The thermoelectric properties of these sintered pellets, including Seebeck coefficient, electrical resistivity and electrical power factor, were measured using Linseis LSR-3 equipment. The Seebeck coefficient of the sintered  $\beta$ -Zn<sub>4</sub>Sb<sub>3</sub> pellets, under produced under pressing pressure of 700 MPa and sintering temperature at 500 °C, 525 °C and 550 °C were measured across varying operating temperature. A comparison of the Seebeck coefficient is shown in Figure 61. The Seebeck coefficient of all sample increased with rising operating temperature up to 300 °C, after which the Seebeck coefficient continued decreased. The experimental results are consistent with literature reports (Lee and Lin, 2018; Kunioka *et al.*, 2018). The Seebeck coefficients of the sintered  $\beta$ -Zn<sub>4</sub>Sb<sub>3</sub> pellets at sintering temperatures of 500 °C, 525 °C and 550 °C are 255  $\mu$ V/°C, 216  $\mu$ V/°C and 191  $\mu$ V/°C, respectively. The positive Seebeck coefficient values of the sintered  $\beta$ -Zn<sub>4</sub>Sb<sub>3</sub> pellets confirms that the sintered pellets are p-type thermoelectric materials. The sintered  $\beta$ -Zn<sub>4</sub>Sb<sub>3</sub> pellets under condition of pressing pressure 700 MPa and sintering temperature at 500 °C showed the highest Seebeck coefficient at an operating temperature of 320 °C, as shown in Figure 61.

In addition to the Seebeck coefficient, the electrical resistivity was also measured. As depicted in Figure 62, the electrical resistivity of all sintered  $\beta$ -Zn<sub>4</sub>Sb<sub>3</sub> pellets samples gradually decreased with increasing operating temperature until reaching 200 °C.

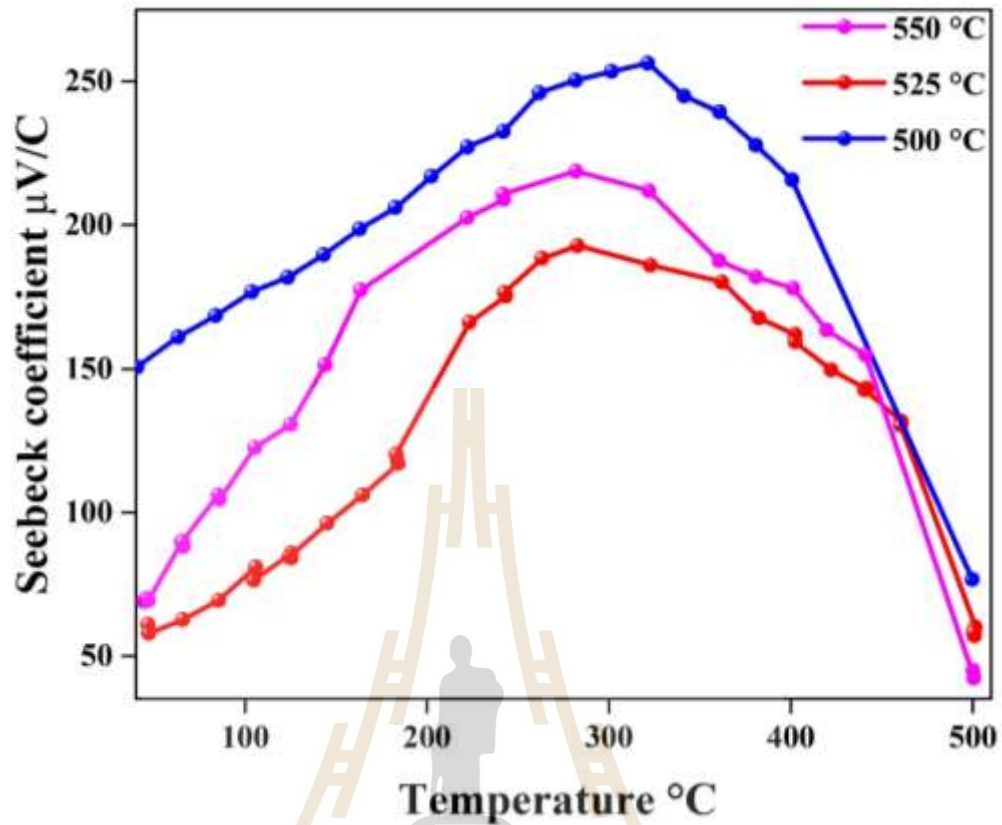


**Figure 61** Seebeck coefficient of the sintered  $\beta$ - $\text{Zn}_4\text{Sb}_3$  pellets versus varying temperature.

The electrical resistivity of all samples remains constant across the operating temperature range of 200–480 °C. The electrical resistivity of the sintered  $\beta$ - $\text{Zn}_4\text{Sb}_3$  pellets within this temperature range is approximately  $1.25 \times 10^{-6} \Omega \cdot \text{m}$  for the sample sintered at 500 °C,  $1.60 \times 10^{-6} \Omega \cdot \text{m}$  for the sample sintered at 500 °C, and  $1.90 \times 10^{-6} \Omega \cdot \text{m}$  for the sample sintered at 500 °C. Although the electrical resistivity curves of all samples are similar, the pellet sintered under a condition of pressing pressure of 700 MPa with sintering temperature of 500 °C stands out, exhibiting the lowest electrical resistivity and thus the highest electrical conductivity. High electrical conductivity positively impacts the figure of merit, as indicated by Equation (96), which reflects superior thermoelectric properties.

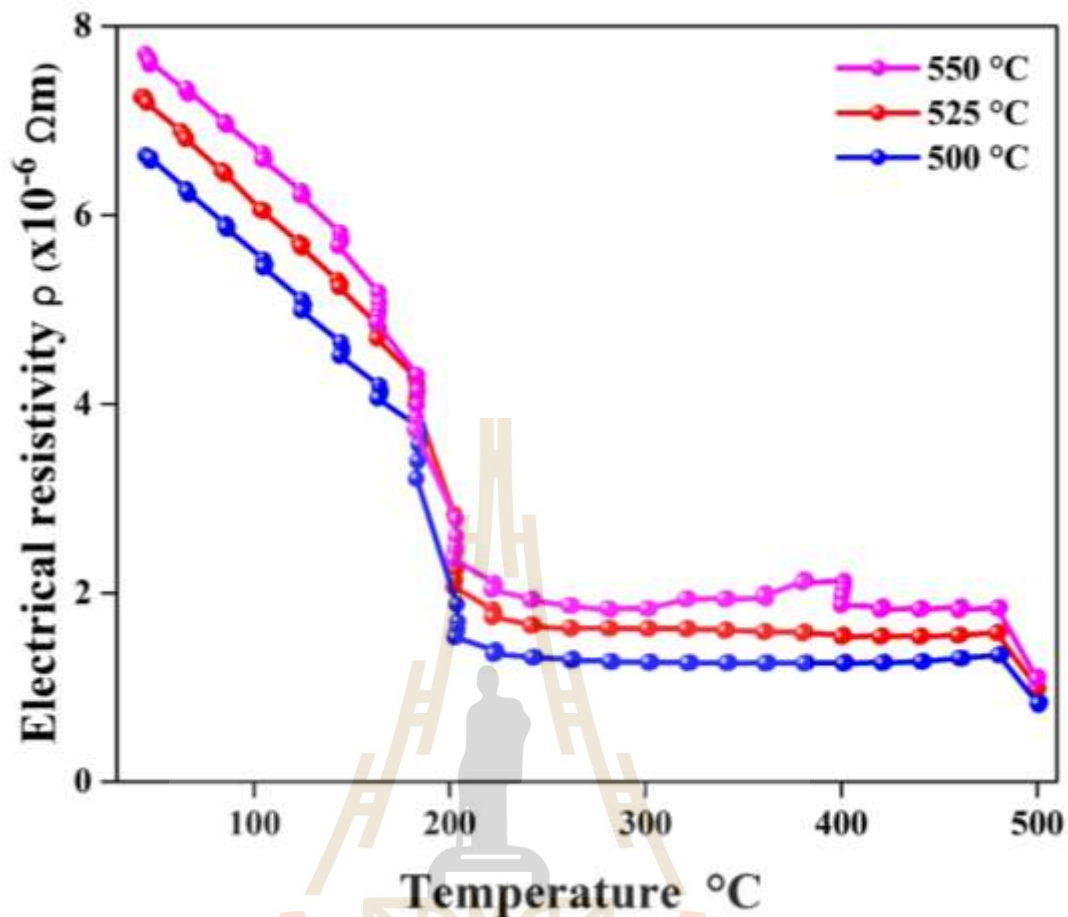


Figure 62 Electrical resistivity of the sintered  $\beta$ -Zn<sub>4</sub>Sb<sub>3</sub> pellets versus varying temperature.

The performance of thermoelectric materials is evaluated by electrical power factor. The electrical power factor of the sintered  $\beta$ -Zn<sub>4</sub>Sb<sub>3</sub> pellets was measured across varying operating temperature. As shown in Figure 63, the electrical power factor exhibits significant fluctuations, which may be attributed to the inherent properties of the sintered  $\beta$ -Zn<sub>4</sub>Sb<sub>3</sub> pellets and potential issues with the measurement equipment. Despite this, the results suggest that the optimal operating temperature for all sintered  $\beta$ -Zn<sub>4</sub>Sb<sub>3</sub> pellets is approximately across temperature range 200–300 °C.

Consequently, a monolithic multi-stack  $\beta$ -Zn<sub>4</sub>Sb<sub>3</sub>/ZnO TEG module were fabricated under condition of pressing pressure of 700 MPa and sintering temperature at 500 °C. This module was tested for performance at operating temperature at 200 °C and 300 °C, corresponding to the highest Seebeck coefficient of 255  $\mu$ V/°C at 320 °C and the optimal operating temperature range (high power factor) of 200–300 °C.

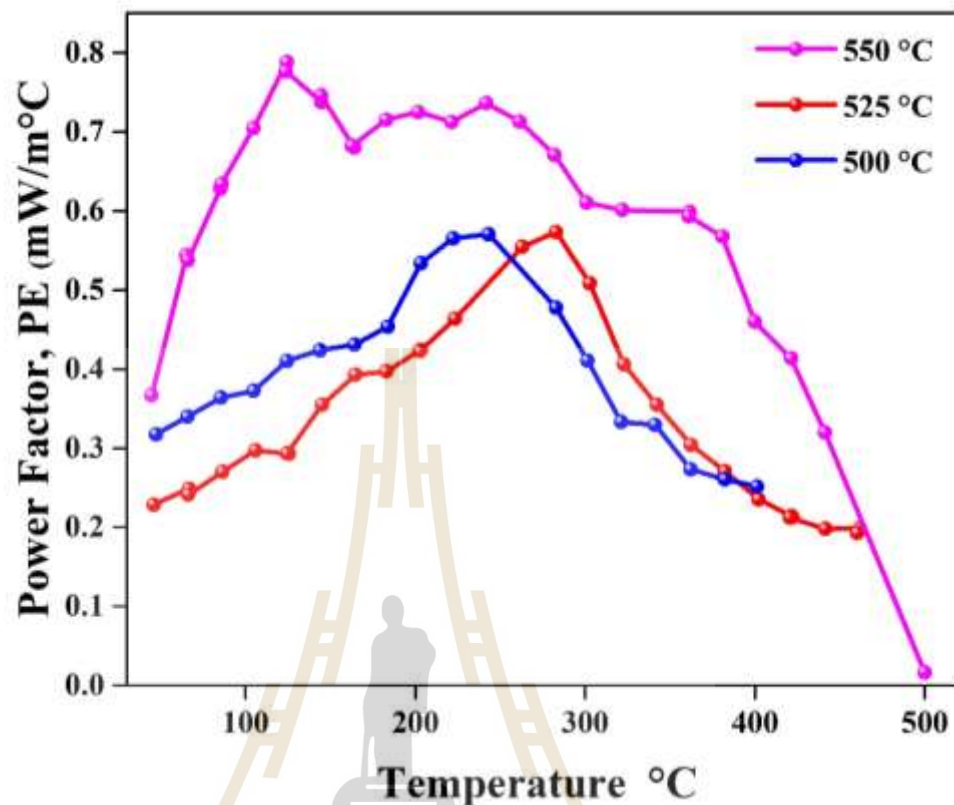
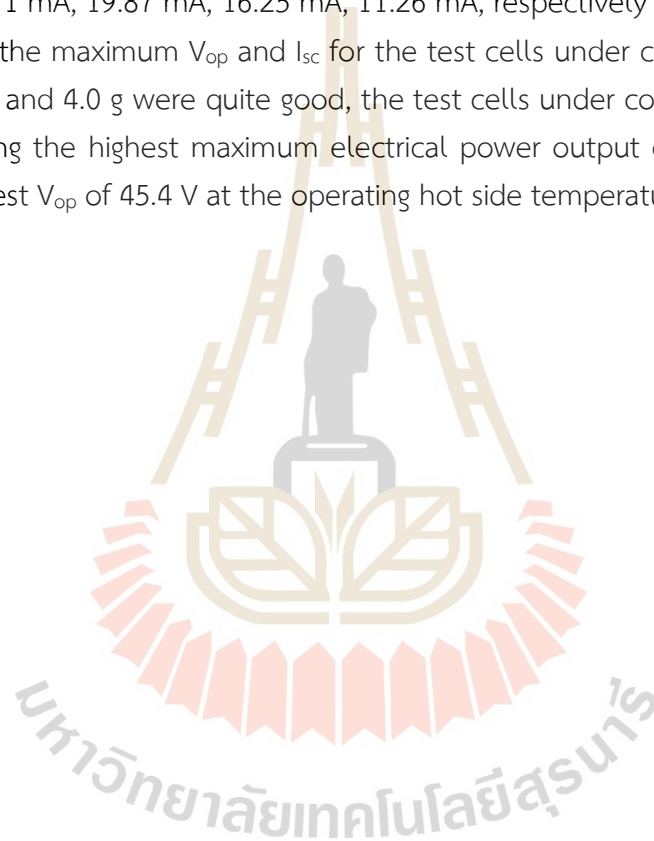


Figure 63 Electrical power factor of the sintered  $\beta$ -Zn<sub>4</sub>Sb<sub>3</sub> pellets versus varying temperature.

#### 4.4 Module analysis and evaluation

The performance of test cells of monolithic  $\beta$ -Zn<sub>4</sub>Sb<sub>3</sub>/ZnO TEG modules and monolithic multi-stack  $\beta$ -Zn<sub>4</sub>Sb<sub>3</sub>/ZnO TEG modules was evaluated using a custom-built heating/cooling system with IV measurement capabilities. Initially, the test cells of the monolithic  $\beta$ -Zn<sub>4</sub>Sb<sub>3</sub>/ZnO TEG modules were assessed for IV characteristics and electrical power output curves. Based on the results, the monolithic multi-stack  $\beta$ -Zn<sub>4</sub>Sb<sub>3</sub>/ZnO TEG modules were fabricated under the condition of the test cells that expressed the best IV-characteristics and electrical power output curves. The test cells were investigated under different conditions, with varying weights of  $\beta$ -Zn<sub>4</sub>Sb<sub>3</sub> powders : 0.2 g, 0.5 g, 1 g, 2 g and 4 g applied to each side of the  $\beta$ -Zn<sub>4</sub>Sb<sub>3</sub> component (Figure 40). Open-circuit voltage ( $V_{op}$ ) and short circuit current ( $I_{sc}$ ) were measured, representing the maximum potential difference and current between the charge terminals of the modules, respectively. The  $V_{op}$  and  $I_{sc}$  measurements of the test cells

under condition of weight 0.2 g, 0.5 g, 1 g, 2 g and 4 g were conducted under operating conditions with a hot side temperature ( $T_h$ ) of 100 °C and gradient temperature ( $\Delta T$ ) of 50 °C,  $T_h=200$  °C –  $\Delta T=50$  °C,  $T_h=200$  °C –  $\Delta T=100$  °C,  $T_h=300$  °C –  $\Delta T=50$  °C and  $T_h=300$  °C –  $\Delta T=100$  °C. The  $V_{op}$  and  $I_{sc}$  results of all the test cells of monolithic  $\beta$ - $Zn_4Sb_3/ZnO$  TEG modules under these conditions are presented in Table 6. The  $V_{op}$  and  $I_{sc}$  values showed an increase with rising hot side temperature and temperature gradient. The maximum  $V_{op}$  and  $I_{sc}$  values for the test cells under condition weight of 0.2 g, 0.5 g, 1.0 g, 2.0 g, 4.0 g are 23.1 mV, 38.1 mV, 45.4 mV, 39.5 mV 41.2 mV, and 8.81 mA, 16.71 mA, 19.87 mA, 16.25 mA, 11.26 mA, respectively at  $T_h=300$  °C –  $\Delta T=100$  °C. Although the maximum  $V_{op}$  and  $I_{sc}$  for the test cells under condition weight of 0.5 g, 1.0 g, 2.0 g and 4.0 g were quite good, the test cells under condition of 1 g was the best, achieving the highest maximum electrical power output of 595  $\mu W$  (Figure 65) and the highest  $V_{op}$  of 45.4 V at the operating hot side temperature of 300°C –  $\Delta T=100$  °C.



**Table 6** List of open-circuit voltage ( $V_{op}$ ) and short circuit current ( $I_{sc}$ ) versus varying operating condition temperature of the test cells of monolithic couple  $\beta$ -Zn<sub>4</sub>Sb<sub>3</sub>/ZnO TEGs with condition of 0.5 g, 1.0 g, 2.0 g and 4.0 g.

Test cells conditions (g)	100°C, $\Delta T$ 50°C		200°C, $\Delta T$ 50°C		200°C, $\Delta T$ 100°C		300°C, $\Delta T$ 50°C		300°C, $\Delta T$ 100°C	
	$V_{op}$ (mV)	$I_{sc}$ (mA)	$V_{op}$ (mV)	$I_{sc}$ (mA)	$V_{op}$ (mV)	$I_{sc}$ (mA)	$V_{op}$ (mV)	$I_{sc}$ (mA)	$V_{op}$ (mV)	$I_{sc}$ (mA)
0.2	5.4	2.12	10.7	4.11	13.7	5.33	12.4	5.11	23.1	8.81
0.5	8.8	1.74	13.8	5.09	28.9	9.62	20.8	8.86	38.1	16.71
1	16.2	6.07	24.1	11.50	31.8	15.61	24.7	11.87	45.4	19.87
2	11.3	4.00	20.9	8.43	29.6	12.02	27.7	11.09	39.5	16.29
4	9.3	1.60	18.9	4.67	23.1	6.55	18.4	4.30	41.2	11.26

Therefore, test cells condition of 1.0 g was selected to applied in fabrication of the multi-stack  $\beta$ -Zn<sub>4</sub>Sb<sub>3</sub>/ZnO TEG modules. Moreover, the IV-curve and electrical power output curve of the test cells of monolithic  $\beta$ -Zn<sub>4</sub>Sb<sub>3</sub>/ZnO TEG module under condition of 1.0 g are shown in Figure 64 and Figure 65, respectively.

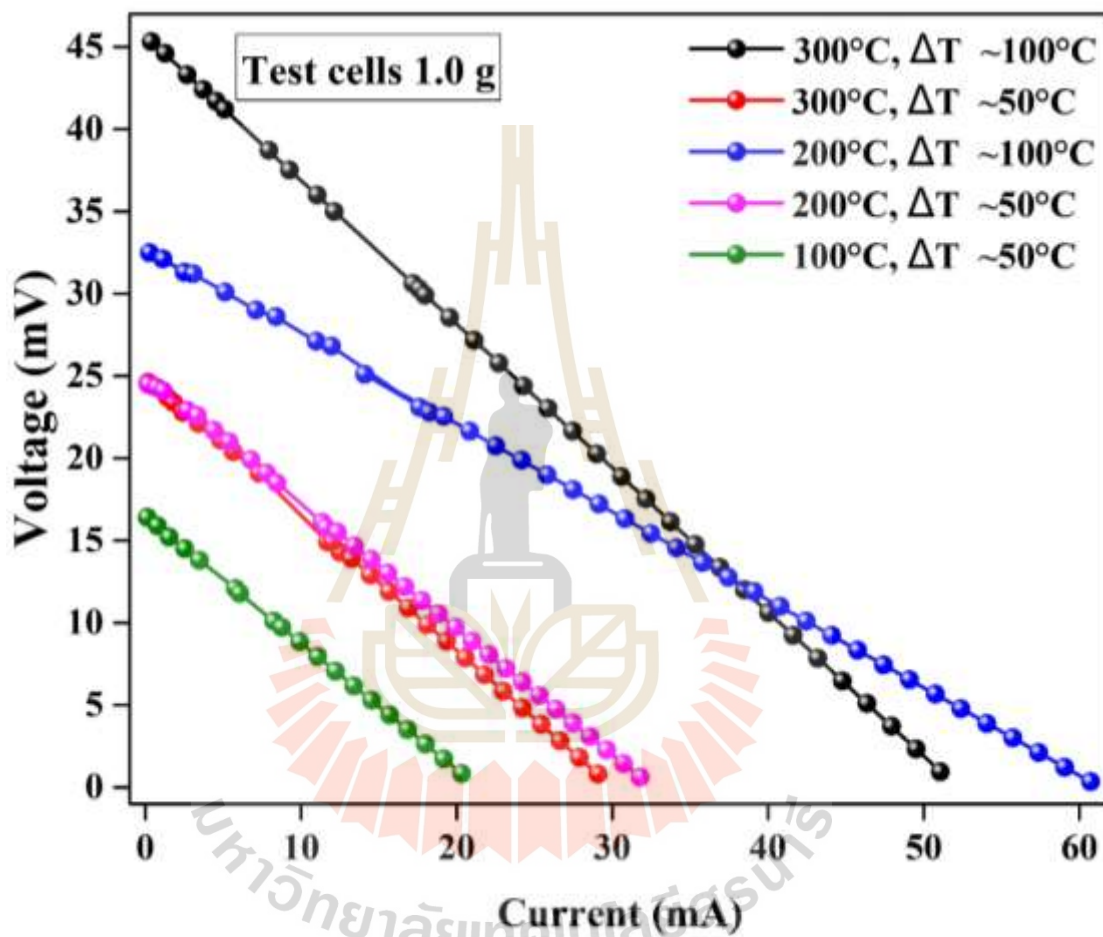


**Figure 64** IV-curve of the test cells of monolithic  $\beta$ -Zn<sub>4</sub>Sb<sub>3</sub>/ZnO TEGs under condition of weight 1.0 g versus different operating  $T_h$  and  $\Delta T$ .

The IV-curve of the test cells of monolithic  $\beta$ -Zn<sub>4</sub>Sb<sub>3</sub>/ZnO TEG module under condition weight of 1.0 g reveals a significant area under the curve at operating conditions of  $T_h=300$  °C –  $\Delta T=100$  °C and  $T_h=200$  °C –  $\Delta T=100$  °C. Moreover, the maximum power output of these test cells is approximately 595  $\mu$ W at  $T_h=300$  °C –  $\Delta T=100$  °C. A comparison of the maximum electrical power output ( $P_{out}$ ) under operating temperatures is presented in Table 7.

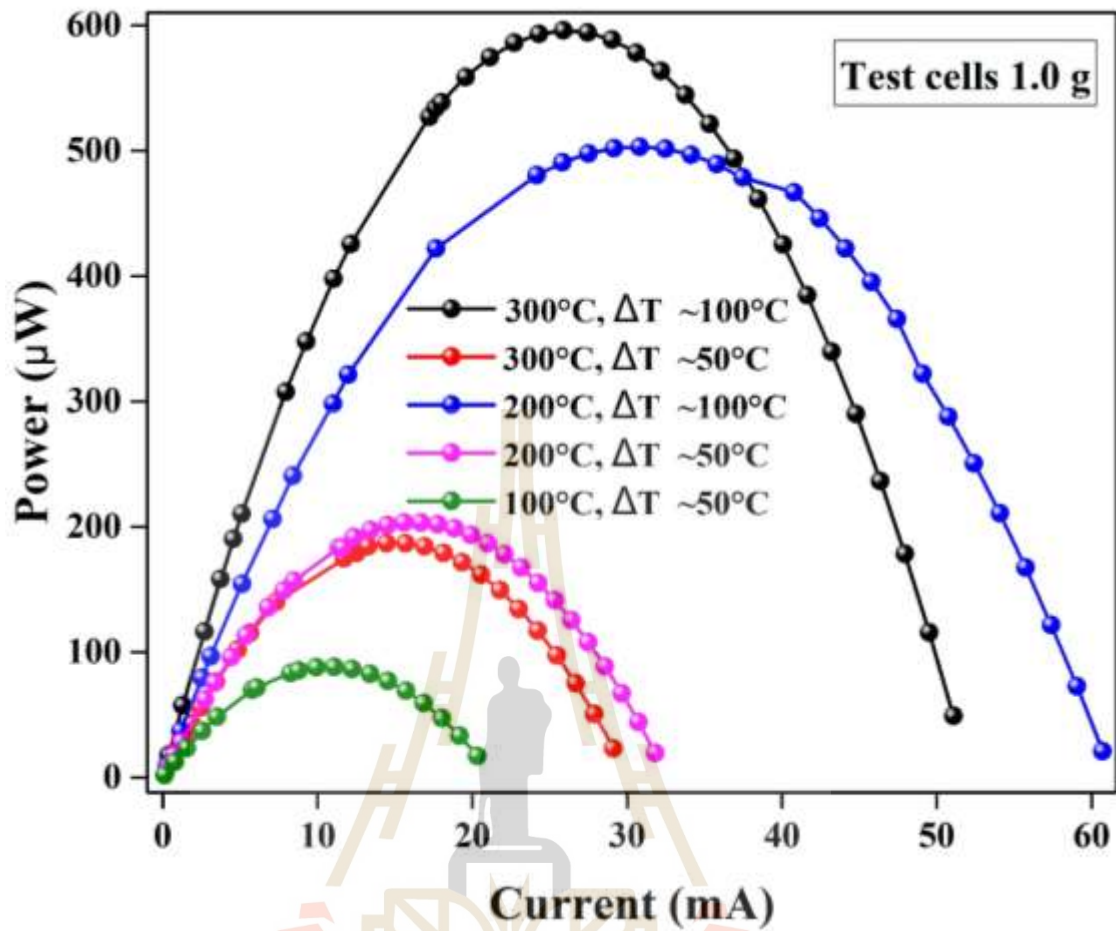


Figure 65 Electrical power output curves of the test cells of monolithic  $\beta\text{-Zn}_4\text{Sb}_3/\text{ZnO}$  TEG module under condition of weight 1.0 g versus different operating  $T_h$  and  $\Delta T$ .

The IV-curves, electrical power output curves and comparative tables of the test cells of monolithic  $\beta\text{-Zn}_4\text{Sb}_3/\text{ZnO}$  TEG modules under conditions of weight 0.2 g, 0.5 g, 2.0 g and 4.0 g are shown in [appendix figure and table part](#).

**Table 7** Comparison of maximum electrical power output of test cell of monolithic  $\beta$ -Zn<sub>4</sub>Sb<sub>3</sub>/ZnO TEG module under condition of weight 1.0 g for different conditions of  $T_h$  and  $\Delta T$ .

Hot-side Temperature	Gradient temperature ( $\Delta T$ )	Maximum $P_{out}$
100 °C	50 °C	87 $\mu W$
200 °C	50 °C	204 $\mu W$
200 °C	100 °C	502 $\mu W$
300 °C	50 °C	186 $\mu W$
300 °C	100 °C	595 $\mu W$

The monolithic multi-stack  $\beta$ -Zn<sub>4</sub>Sb<sub>3</sub>/ZnO TEG module was measured  $V_{op}$  and  $I_{sc}$  across its charge terminals. The  $V_{op}$  and  $I_{sc}$  of the monolithic multi-stack  $\beta$ -Zn<sub>4</sub>Sb<sub>3</sub>/ZnO TEG module were measured under various operating condition, with a hot side temperature ( $T_h$ ) of 100 °C and gradient temperature ( $\Delta T$ ) of 50 °C, as well as  $T_h=200$  °C –  $\Delta T=50$  °C,  $T_h=200$  °C –  $\Delta T=100$  °C,  $T_h=300$  °C –  $\Delta T=50$  °C and  $T_h=300$  °C –  $\Delta T=100$  °C. The results of  $V_{op}$  and  $I_{sc}$  of the monolithic multi-stack  $\beta$ -Zn<sub>4</sub>Sb<sub>3</sub>/ZnO TEG module under all operating conditions are listed in Table 8, as illustrated in Figure 62 and Figure 63.

**Table 8** The  $V_{op}$  and  $I_{sc}$  values for the monolithic multi-stack  $\beta$ -Zn<sub>4</sub>Sb<sub>3</sub>/ZnO TEG module were found to be 11.6 mV, 36.0 mV, 45.3 mV 47.5 mV, 73.1 mV and 5.11 mA, 14.83 mA, 18.07 mA, 13.53 mA, 18.36 mA, respectively, for  $T_h=100$  °C –  $\Delta T=50$  °C,  $T_h=200$  °C –  $\Delta T=50$  °C,  $T_h=200$  °C –  $\Delta T=100$  °C,  $T_h=300$  °C –  $\Delta T=50$  °C and 300°C –  $\Delta T$  100 °C, respectively. The results showed an increasing trend in both  $V_{op}$  and  $I_{sc}$  as  $T_h$  and  $\Delta T$  increased. As depicted in Figure 66, the IV-curves of the multi-stack  $\beta$ -Zn<sub>4</sub>Sb<sub>3</sub>/ZnO TEG module at operating temperature of  $T_h=300$  °C exhibit a similar steep slope under condition of  $\Delta T=50$  °C and  $\Delta T=100$  °C, while the intercepts on the current axis differ significantly between these two conditions. Conversely, the IV-curve results at  $T_h=200$  °C appear quite similar to each other, likely due to the effects of low electrical resistivity and the enhanced power factor of the  $\beta$ -Zn<sub>4</sub>Sb<sub>3</sub> pellets at an operating temperature of 200 °C, as illustrated in Figure 62 and Figure 63.

**Table 8** List of open-circuit voltage ( $V_{op}$ ) and short circuit current ( $I_{sc}$ ) versus varying operating condition temperature of the monolithic multi-stack  $\beta$ - $Zn_4Sb_3/ZnO$  TEGs.

Hot-side Temperature	Gradient temperature ( $\Delta T$ )	Open-circuit voltage ( $V_{op}$ ) mV	Short circuit current ( $I_{sc}$ ) mA
100 °C	50 °C	11.6	5.11
200 °C	50 °C	36.0	14.83
200 °C	100 °C	45.3	18.07
300 °C	50 °C	47.5	13.53
300 °C	100 °C	73.1	18.36

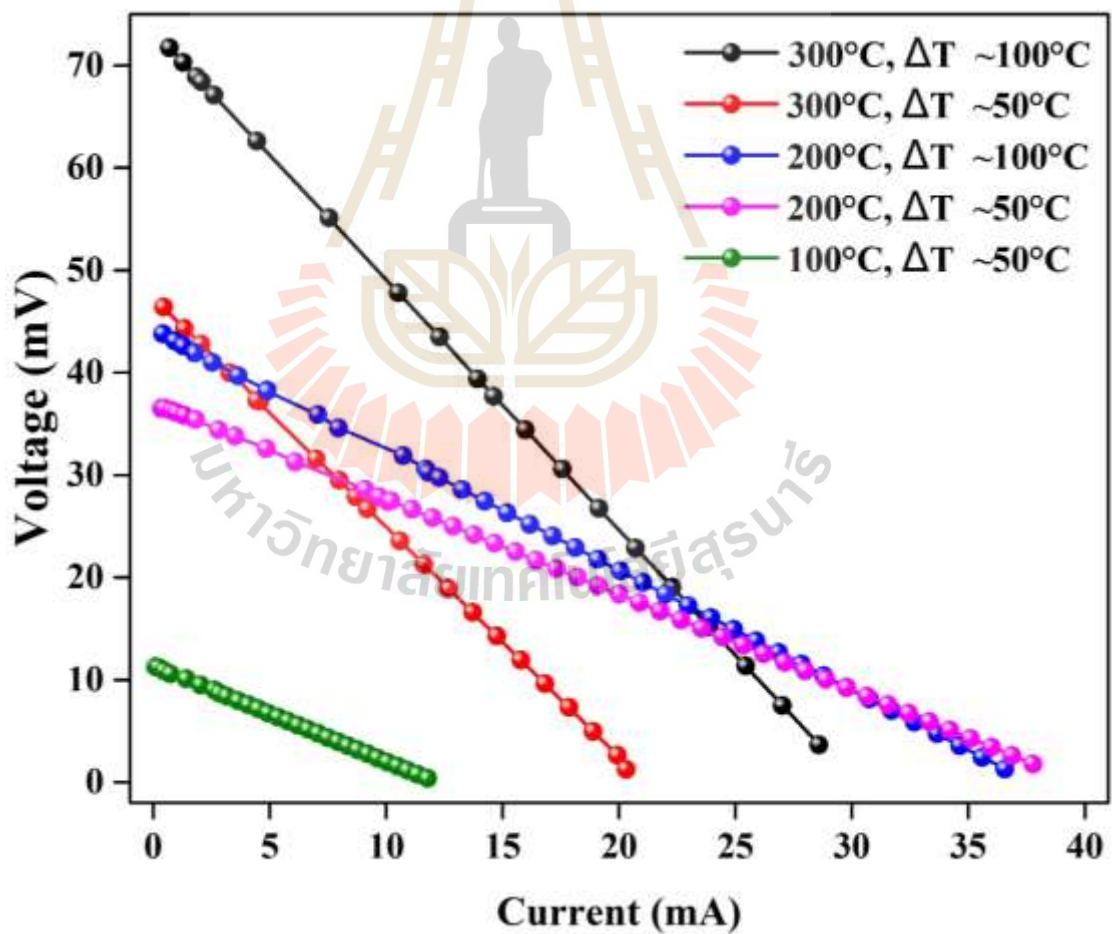


**Figure 66** IV characteristics of the monolithic multi-stack  $\beta$ - $Zn_4Sb_3/ZnO$  TEGs versus varying operation hot side temperature and temperature gradients  $\Delta T$ .

As depicted in Figure 67, the operating condition that produced the highest maximum electrical power output ( $P_{out}$ ) of 550  $\mu\text{W}$  was  $T_h=300\text{ }^\circ\text{C}-\Delta T=100\text{ }^\circ\text{C}$ , while the lowest  $P_{out}$  of 38  $\mu\text{W}$  was observed under the condition of  $T_h=100\text{ }^\circ\text{C}-\Delta T=50\text{ }^\circ\text{C}$ . A comparison of maximum electrical power output ( $P_{out}$ ) under different operating conditions is provided in Table 9. Although, the maximum electrical power output was achieved under the operating temperature of  $T_h=300\text{ }^\circ\text{C}-\Delta T=100\text{ }^\circ\text{C}$ , the optimal operating temperature for the monolithic  $\beta\text{-Zn}_4\text{Sb}_3/\text{ZnO}$  TEG module is  $T_h=200\text{ }^\circ\text{C}$ . This is because the electrical power output curves at  $T_h=200\text{ }^\circ\text{C}$  of the monolithic  $\beta\text{-Zn}_4\text{Sb}_3/\text{ZnO}$  TEG modules demonstrate remarkably consistent behaviour under both  $\Delta T=50\text{ }^\circ\text{C}$  and  $\Delta T=100\text{ }^\circ\text{C}$  conditions. The broad and consistent IV-curves and electrical power output curves at  $T_h=200\text{ }^\circ\text{C}$  suggest that the monolithic  $\beta\text{-Zn}_4\text{Sb}_3/\text{ZnO}$  TEG modules is suited for application as an electrical generator that can operate under fluctuation  $\Delta T$  conditions, specifically within the range of  $\Delta T$  50–100  $^\circ\text{C}$  at an operating temperature of 200  $^\circ\text{C}$ .

**Table 9** Results of the maximum electrical power output for different conditions of hot-side temperature and  $\Delta T$  of the monolithic  $\beta\text{-Zn}_4\text{Sb}_3/\text{ZnO}$  TEGs.

Hot-side Temperature	Gradient temperature ( $\Delta T$ )	Maximum $P_{out}$
100 $^\circ\text{C}$	50 $^\circ\text{C}$	38 $\mu\text{W}$
200 $^\circ\text{C}$	50 $^\circ\text{C}$	370 $\mu\text{W}$
200 $^\circ\text{C}$	100 $^\circ\text{C}$	418 $\mu\text{W}$
300 $^\circ\text{C}$	50 $^\circ\text{C}$	250 $\mu\text{W}$
300 $^\circ\text{C}$	100 $^\circ\text{C}$	550 $\mu\text{W}$

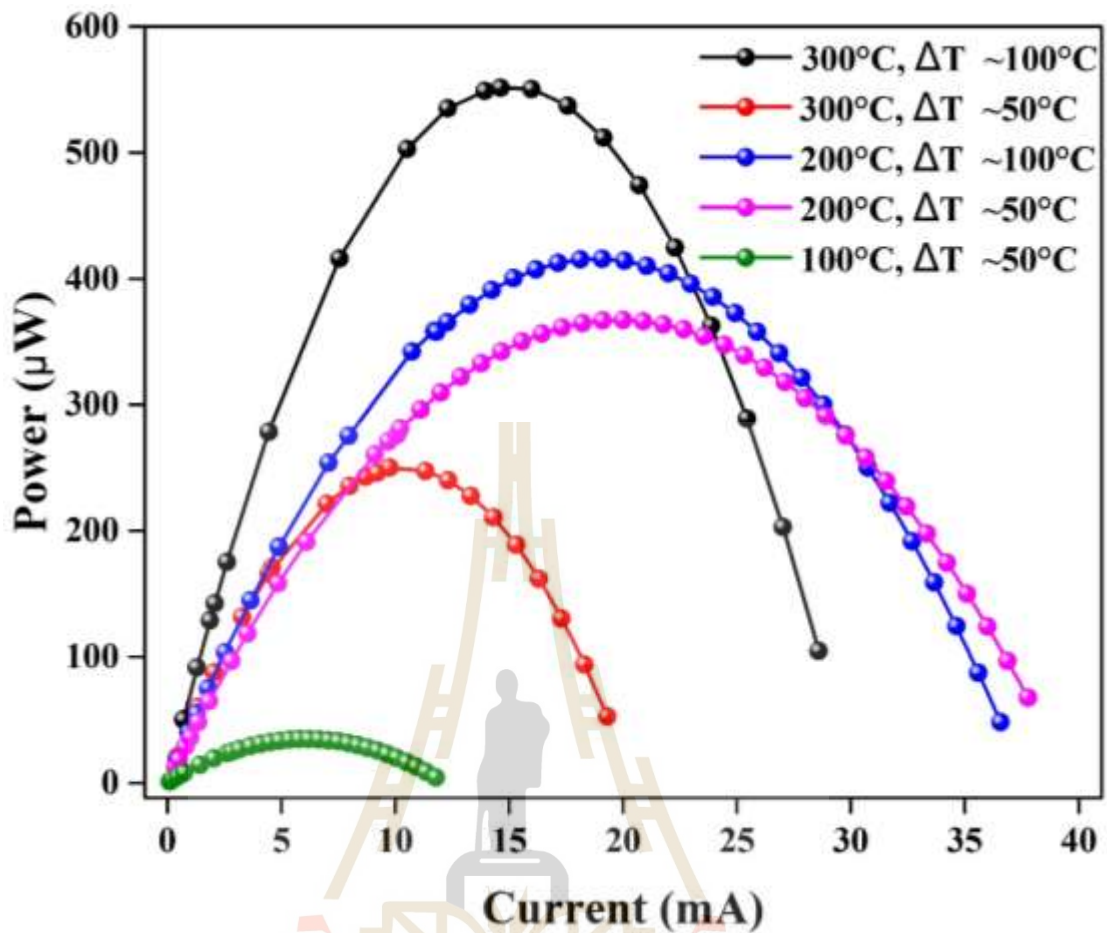


Figure 67 Electrical power output curves of the monolithic multi-stack  $\beta$ -Zn<sub>4</sub>Sb<sub>3</sub>/ZnO TEGs versus varying operation hot side temperature and temperature gradients  $\Delta T$ .

Based on the maximum electrical power output of 550  $\mu$ W, the monolithic  $\beta$ -Zn<sub>4</sub>Sb<sub>3</sub>/ZnO TEG modules are comparable to other monolithic TEG modules that reported in the literature. A comparison of the maximum electrical power output from this work with of other reports is shown in Table 10.

**Table 10** Comparison of the maximum electrical power output versus variant monolithic TEG modules of this work and literature reports.

TE-materials	N-pairs	N-cells	T <sub>h</sub> (°C)	ΔT (°C)	P <sub>out</sub> (μW)	Ref.
Single walled carbon nanotube (SWCNT)	8	16	70	50	7.19	(Hasan <i>et al.</i> , 2024)
Bi <sub>0.5</sub> Sb <sub>1.5</sub> Te <sub>3</sub> & Ag <sub>2</sub> S <sub>0.2</sub> Se <sub>0.8</sub>	3	6	130	50	2,350	(Lai <i>et al.</i> , 2022)
Ni <sub>0.9</sub> Mo <sub>0.1</sub> & La <sub>0.035</sub> Sr <sub>0.965</sub> TiO <sub>3</sub>	50	100	30	10	100	(Funahashi <i>et al.</i> , 2011)
Cu <sub>2.075</sub> Se & Ag <sub>2</sub> S <sub>0.55</sub> Se <sub>0.45</sub>	1	2	60	30	310	(Ang <i>et al.</i> , 2023)
β-Zn <sub>4</sub> Sb <sub>3</sub>	0	4	300	100	550	this work

## CHAPTER V

### CONCLUSION AND SUGGESTION

In this research, the  $\beta$ -Zn<sub>4</sub>Sb<sub>3</sub> powders was successfully synthesized using solid state reaction method via mechanical alloying technique. The crystallite structure was analyzed through X-ray diffraction technique. The oxidation states of Zn and Sb elements in the local structure of the synthesized  $\beta$ -Zn<sub>4</sub>Sb<sub>3</sub> powder were investigated using X-ray absorption near-edge structure spectra at the Zn K-edge and Sb-L edges. The sintered  $\beta$ -Zn<sub>4</sub>Sb<sub>3</sub> pellets were fabricated through a compression and sintering process under Ar gas flow system. Thermoelectric properties, including the Seebeck coefficient, electrical resistivity and power factor of the sintered  $\beta$ -Zn<sub>4</sub>Sb<sub>3</sub> pellets were measured using Linseis LSR-3 equipment. The test cells of monolithic  $\beta$ -Zn<sub>4</sub>Sb<sub>3</sub>/ZnO TEG modules, with conditions  $\beta$ -Zn<sub>4</sub>Sb<sub>3</sub> weight of 0.2 g, 0.5 g, 1 g, 2 g and 4 g were successfully fabricated using cyclical compression process, calcination method, and electrical connection method. Additionally, the monolithic multi-stack  $\beta$ -Zn<sub>4</sub>Sb<sub>3</sub>/ZnO TEG module was fabricated using the same procedures as the test cells. The electrical power output curves and IV-curves of both the test cells and the monolithic multi-stack  $\beta$ -Zn<sub>4</sub>Sb<sub>3</sub>/ZnO TEG module were evaluated and analyzed using a custom-built heating/cooling system with IV measurement capabilities. The conclusions of this research are divided into four sections: structure and characterization, thermoelectric properties, module analysis and evaluation, and suggestions for future work.

#### 5.1 Structure and characterization

X-ray diffraction (XRD) pattern of the synthesized  $\beta$ -Zn<sub>4</sub>Sb<sub>3</sub> powders, produced under conditions of excess Zn powders, were analyzed using XRD technique. The XRD patterns results indicated that optimal synthesis condition is adding 12 at.% Zn rich and calcination temperature of 450 °C for 3 hours. Under these conditions, the XRD patterns revealed a dominant crystalline phase of  $\beta$ -Zn<sub>4</sub>Sb<sub>3</sub> with minor secondary phases of ZnSb, Zn and Sb. The XRD patterns of the synthesized  $\beta$ -Zn<sub>4</sub>Sb<sub>3</sub> powders, with excess Zn powders 12 at.% and calcined at 450 °C for 3 hours, corresponds to the calculated XRD patterns  $\beta$ -Zn<sub>4</sub>Sb<sub>3</sub> of Mozharivskij's model (Mozharivskij *et al.*, 2006). The observed secondary phases of ZnSb, Zn and Sb are probably due to the limited temperature stability during calcination under argon gas flow, including the

inversion of the crystalline phase of ZnSb during cooling process, resulting in the formation of crystalline phase ZnSb at across temperature of 100–200 °C (Zhang *et al.*, 2016).

The ionization energy of exciting core electrons for Zn and Sb elements in the synthesized  $\beta$ -Zn<sub>4</sub>Sb<sub>3</sub> powders were investigated using X-ray absorption near-edge structure (XANES) spectroscopy. The ionization energies of exciting core electrons for Zn and Sb elements in local atoms structure of the synthesized  $\beta$ -Zn<sub>4</sub>Sb<sub>3</sub> powders were measured at level K (Zn K-edge) and level L (Sb L-edges), respectively. The primary absorption edges at the Zn K-edge and Sb L-edges indicate that the ionization energies of the core electrons correspond to oxidation states of Zn<sup>0</sup> and Sb<sup>0</sup>. The normalized XANES and derivative of normalized XANES spectra confirm that the synthesized  $\beta$ -Zn<sub>4</sub>Sb<sub>3</sub> powders have an alloy structure, demonstrating the absence of ionic bonding and oxides.

## 5.2 Thermoelectric properties

The Seebeck coefficient, electrical resistivity, and power factor of the sintered  $\beta$ -Zn<sub>4</sub>Sb<sub>3</sub> pellets were measured. The Seebeck coefficient of all sample increase with rising operating temperature, peaking around 300 °C, before gradually decreasing. Among the samples, the sintered  $\beta$ -Zn<sub>4</sub>Sb<sub>3</sub> pellet pressed at 700 MPa and sintered at 500 °C exhibited the highest Seebeck coefficient of 255  $\mu$ V/°C at an operating temperature of 320 °C. The positive Seebeck coefficient confirms that the sintered  $\beta$ -Zn<sub>4</sub>Sb<sub>3</sub> pellets are p-type thermoelectric materials. The electrical resistivity of the sintered  $\beta$ -Zn<sub>4</sub>Sb<sub>3</sub> pellets decreased steadily up to around 200 °C, after which it remained constant across the temperature range of 200–480 °C. While the electrical resistivity feature of all sintered  $\beta$ -Zn<sub>4</sub>Sb<sub>3</sub> pellets were similar, the sintered  $\beta$ -Zn<sub>4</sub>Sb<sub>3</sub> pellets under conditions of pressing pressure of 700 MPa with sintering temperature of 500 °C showed the lowest resistivity, making it the most favorable. The electrical power factor of all sample exhibited considerable fluctuations, likely due to inherent variations in the properties of the sintered  $\beta$ -Zn<sub>4</sub>Sb<sub>3</sub> pellets or possible sensor issues with the measurement equipment. Despite these fluctuations, the results suggest that the optimal operating temperature for all sintered  $\beta$ -Zn<sub>4</sub>Sb<sub>3</sub> pellets is across between 200–300 °C.

### 5.3 Module analysis and evaluation

The evaluation and performance of test cells of monolithic  $\beta$ -Zn<sub>4</sub>Sb<sub>3</sub>/ZnO TEG module was revealed using a custom-built heating/cooling system with IV measurement capabilities. The  $V_{op}$  and  $I_{sc}$  of test cells of monolithic  $\beta$ -Zn<sub>4</sub>Sb<sub>3</sub>/ZnO TEG module, with condition monolithic  $\beta$ -Zn<sub>4</sub>Sb<sub>3</sub> weight of 0.5 g, 1.0 g, 2.0 g and 4.0 g revealed significant potential results. However, the 1 g test cell of monolithic  $\beta$ -Zn<sub>4</sub>Sb<sub>3</sub>/ZnO TEG module was the most efficient in terms of mass usage and produced the highest maximum electrical power output of 595  $\mu$ W and the highest  $V_{op}$  of 45.4 V at an operating hot side temperature of 300°C –  $\Delta T=100$  °C.

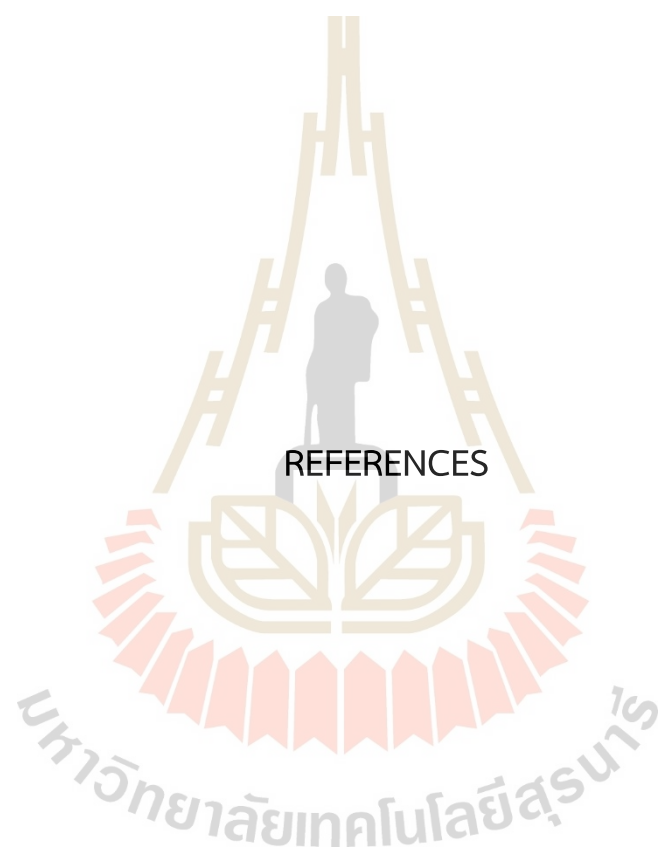
The evaluation and performance of the monolithic multi-stack  $\beta$ -Zn<sub>4</sub>Sb<sub>3</sub>/ZnO TEG module also was revealed using a custom-built heating/cooling system with IV measurement capabilities. The  $V_{op}$  and  $I_{sc}$  of monolithic multi-stack  $\beta$ -Zn<sub>4</sub>Sb<sub>3</sub>/ZnO TEG module revealed that both incremental  $V_{oc}$  and  $I_{sc}$  increased with rising operating temperatures and  $\Delta T$ . The IV-curve results of the multi-stack  $\beta$ -Zn<sub>4</sub>Sb<sub>3</sub>/ZnO TEG module at operating temperature of 300 °C shows the highest maximum electrical power output ( $P_{out}$ ) of 550  $\mu$ W and the highest  $V_{op}$  of 73.2 V, with similar steep slope under both  $T_h=300$  °C– $\Delta T=50$  °C and  $T_h=300$  °C– $\Delta T=100$  °C conditions. However, the optimal operating temperature for the monolithic multi-stack  $\beta$ -Zn<sub>4</sub>Sb<sub>3</sub>/ZnO TEG module was found to be the  $T_h=200$  °C– $\Delta T=50$ –100 °C, as the electrical power output curves at this temperature demonstrated consistent performance under both temperature gradient conditions. The wide and consistent of IV-curves and electrical power output curves of the monolithic multi-stack  $\beta$ -Zn<sub>4</sub>Sb<sub>3</sub>/ZnO TEG modules suggest their potential for use in electrical generators that can withstand temperature fluctuations at an operating temperature of 200 °C with  $\Delta T$  50–100 °C.

### 5.4 Suggestion

This work presents the invention of a thermoelectric generators module designed to recycle energy from industrial waste heat in industrial activities and public utilities, as mentioned in chapter I. The author aimed to use low cost materials and a simple fabrication method to invent a thermoelectric generators module that others can easily replicate. The author expected that the initial goal was for fabricated thermoelectric generator module to achieve at least  $V_{op}\sim 1$  volt and  $I_{sc}\sim 0.1$  A. While the results of this work did not meet these expectations. However, the author hoped that the fabrication of monolithic multi-stack  $\beta$ -Zn<sub>4</sub>Sb<sub>3</sub>/ZnO TEG modules will contribute

valuable insights and inspire future applications. Finally, the author would like to thank all readers and welcome any comments or suggestions.





REFERENCES

## REFERENCES

- Adjadj, F., Belbacha, E.-d., Bouharkat, M. and Kerboub, A. (2006). Crystallographic study of the intermediate compounds  $\text{SbZn}$ ,  $\text{Sb}_3\text{Zn}_4$  and  $\text{Sb}_2\text{Zn}_3$ . *Journal of Alloys and Compounds*. 419(1–2), 267–270.
- Ahn, J., Oh, M., Kim, B., Park, S., Min, B., Lee, H. and Shim, Y. (2011). Thermoelectric properties of  $\text{Zn}_4\text{Sb}_3$  prepared by hot pressing. *Materials Research Bulletin*. 46(9), 1490–1495.
- Ang, A. K. R., Yamazaki, I., Hirata, K., Singh, S., Matsunami, M. and Takeuchi, T. (2023). Development of  $\text{Cu}_2\text{Se}/\text{Ag}_2(\text{S}, \text{Se})$ -based monolithic thermoelectric generators for low-grade waste heat energy harvesting. *ACS Applied Materials & Interfaces*. 15(40), 46962–46970.
- Asfandiyar, Wei, T.-R., Li, Z., Sun, F.-H., Pan, Y., Wu, C.-F., Farooq, M. U., Tang, H., Li, F. and Li, B. (2017). Thermoelectric  $\text{SnS}$  and  $\text{SnS}-\text{SnSe}$  solid solutions prepared by mechanical alloying and spark plasma sintering: anisotropic thermoelectric properties. *Scientific reports*. 7(1), 43262.
- Beer, A. and Cochran, K. (1952) Chapter XIII semiconducting compounds : in digest of literature on dielectrics. *IEEE* (16), 136–152.
- Biswas, K., He, J., Blum, I. D., Wu, C.-I., Hogan, T. P., Seidman, D. N., Dravid, V. P. and Kanatzidis, M. G. (2012). High-performance bulk thermoelectrics with all-scale hierarchical architectures. *Nature*. 489(7416): 414–418.
- Bokii, G. and Klevtsova, R. (1965). X-ray structure investigation of the  $\beta$ -phase in the zinc—antimony system. *Journal of Structural Chemistry*. 6(6), 830–834.
- Bokov, D., Turki Jalil, A., Chupradit, S., Suksatan, W., Javed Ansari, M., Shewael, I. H., Valiev, G. H. and Kianfar, E. (2021). Nanomaterial by sol-gel method: synthesis and application. *Advances in Materials Science and Engineering*. 1–21.
- Borup, M. A., Blichfeld, A. B., Madsen, S. R. and Iversen, B. B. (2016). High-pressure single crystal X-ray diffraction study of thermoelectric  $\text{ZnSb}$  and  $\beta\text{-Zn}_4\text{Sb}_3$ . *Dalton Transactions*. 45(38), 15097–15103.
- Böttger, P. M., Diplas, S., Flage-Larsen, E., Prytz, Ø. and Finstad, T. G. (2011). Electronic structure of thermoelectric  $\text{Zn}-\text{Sb}$ . *Journal of Physics: Condensed Matter*. 23(26), 265502.

- Caillat, T., Fleurial, J.-P. and Borshchevsky, A. (1997). Preparation and thermoelectric properties of semiconducting  $Zn_4Sb_3$ . *Journal of Physics and Chemistry of Solids*. 58(7), 1119–1125.
- Chen, G. (2005). Nanoscale energy transport and conversion: a parallel treatment of electrons, molecules, phonons, and photons. *Oxford university press*.
- Crawford, C. (2014). Transverse thermoelectric effect.
- Dreßler, C., Bochmann, A., Schulz, T., Reimann, T., Töpfer, J. and Teichert, S. (2015). Transversal oxide–metal thermoelectric device for low–power energy harvesting. *Energy Harvesting and Systems*. 2(1), 25–35.
- Funahashi, S., Nakamura, T., Kageyama, K. and Ieki, H. (2011). Monolithic oxide–metal composite thermoelectric generators for energy harvesting. *Journal of Applied Physics*. 109(12).
- Gainza, J., Serrano–Sanchez, F., Rodrigues, J. E., Huttel, Y., Dura, O. J., Koza, M. M., Fernández–Díaz, M. T., Melendez, J. J., Markus, B. G. and Simon, F. (2020). High–performance n–type SnSe thermoelectric polycrystal prepared by arc–melting. *Cell Reports Physical Science*. 1(12).
- Gharsallah, M., Serrano–Sánchez, F., Bermúdez, J., Nemes, N., Martínez, J., Elhalouani, F. and Alonso, J. (2016). Nanostructured  $Bi_2Te_3$  prepared by a straightforward arc–melting method. *Nanoscale Research Letters*. (11), 1–7.
- Goldsmid, H. (2017). Transverse thermoelectric effects and their application. *Materials, Preparation, and Characterization in Thermoelectrics*. 1–12.
- Goldsmid, H. J. (2010). Introduction to thermoelectricity. *Springer*.
- Hasan, M. N., Muthalif, A. G. A., Saleh, T., Zhang, Z. B. and Ali, M. S. M. (2024). Monolithic carbon nanotube film thermoelectric generator. *IEEE Transactions on Electron Devices*. 71(2), 1179–1184.
- Hsu, K. F., Loo, S., Guo, F., Chen, W., Dyck, J. S., Uher, C., Hogan, T., Polychroniadis, E. and Kanatzidis, M. G. (2004). Cubic  $AgPb_m SbTe^{2+}_m$ : bulk thermoelectric materials with high figure of merit. *Science*. 303(5659), 818–821.
- Ito, K., Zhang, L., Adachi, K. and Yamaguchi, M. (2003). Low thermal conductivity and related thermoelectric properties of  $Zn_4Sb_3$  and  $CoSb_3$  thin films. *MRS Online Proceedings Library (OPL)*. 793.

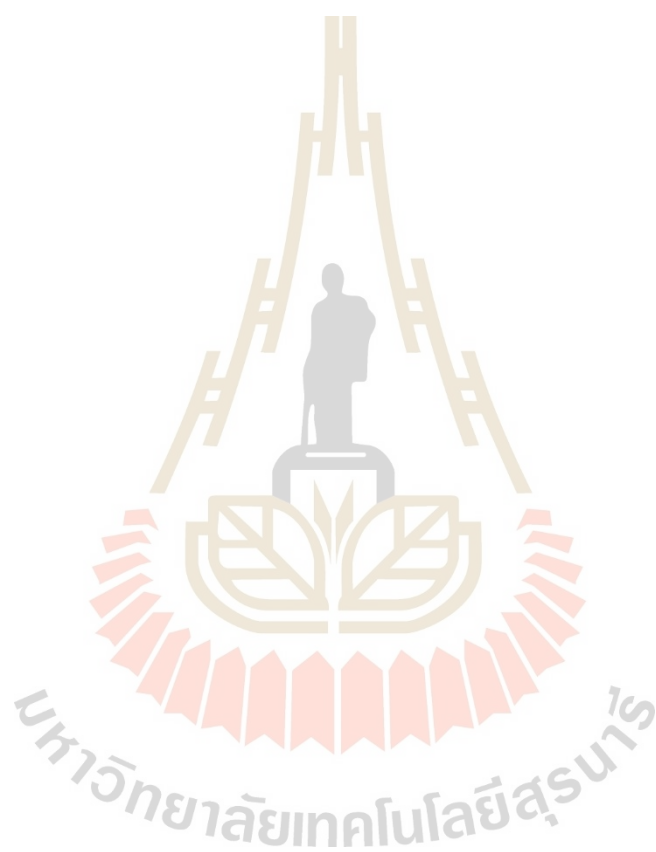
- Jantrasee, S., Moontragoon, P. and Pinitsoontorn, S. (2016). Thermoelectric properties of Al-doped ZnO: experiment and simulation. *Journal of Semiconductors*. 37(9), 092002.
- Jood, P., Mehta, R. J., Zhang, Y., Peleckis, G., Wang, X., Siegel, R. W., Borca-Tasciuc, T., Dou, S. X. and Ramanath, G. (2011). Al-doped zinc oxide nanocomposites with enhanced thermoelectric properties. *Nano letters*. 11(10), 4337–4342.
- Kumar, A., Singh, A. and Suhane, A. (2022). Mechanically alloyed high entropy alloys: existing challenges and opportunities. *Journal of Materials Research and Technology*. 17, 2431–2456.
- Kunioka, H., Obara, H., Yamamoto, A. and Iida, T. (2018). Observation of interface between thermoelectric material  $Zn_4Sb_3$  and electrodes by resistance scanning and Seebeck coefficient mapping techniques. *Materials Transactions*. 59(7), 1035–1040.
- Lai, H., Singh, S., Peng, Y., Hirata, K., Ryu, M., Ang, A. K. R., Miao, L. and Takeuchi, T. (2022). Enhanced performance of monolithic chalcogenide thermoelectric modules for energy harvesting via co-optimization of experiment and simulation. *ACS Applied Materials & Interfaces*. 14(34), 38642–38650.
- Lan, J.-L., Liu, Y., Lin, Y.-H., Nan, C.-W., Cai, Q. and Yang, X. (2015). Enhanced thermoelectric performance of  $In_2O_3$ -based ceramics via nanostructuring and point defect engineering. *Scientific Reports*. 5(1), 7783.
- Lee, P.-Y. and Lin, P.-H. (2018). Evolution of thermoelectric properties of  $Zn_4Sb_3$  prepared by mechanical alloying and different consolidation routes. *Energies*. 11(5), 1200.
- Levin, E., Bud'ko, S. and Schmidt-Rohr, K. (2012). Enhancement of thermopower of TAGS-85 high-performance thermoelectric material by doping with the rare earth Dy. *Advanced Functional Materials*. 22(13), 2766–2774.
- Liang, J., Wang, T., Qiu, P., Yang, S., Ming, C., Chen, H., Song, Q., Zhao, K., Wei, T.-R. and Ren, D. (2019). Flexible thermoelectrics: from silver chalcogenides to full-inorganic devices. *Energy & Environmental Science*. 12(10), 2983–2990.
- Lin, J., Li, X., Qiao, G., Wang, Z., Carrete, J. s., Ren, Y., Ma, L., Fei, Y., Yang, B. and Lei, L. (2014). Unexpected high-temperature stability of  $\beta$ - $Zn_4Sb_3$  opens the door to enhanced thermoelectric performance. *Journal of the American Chemical Society*. 136(4), 1497–1504.
- Mansouri, H., Sajjadi, S. A., Babakhani, A. and Saberi, Y. (2021). Microstructure and thermoelectric performance evaluation of p-type  $(Bi, Sb)_2Te_3$  materials

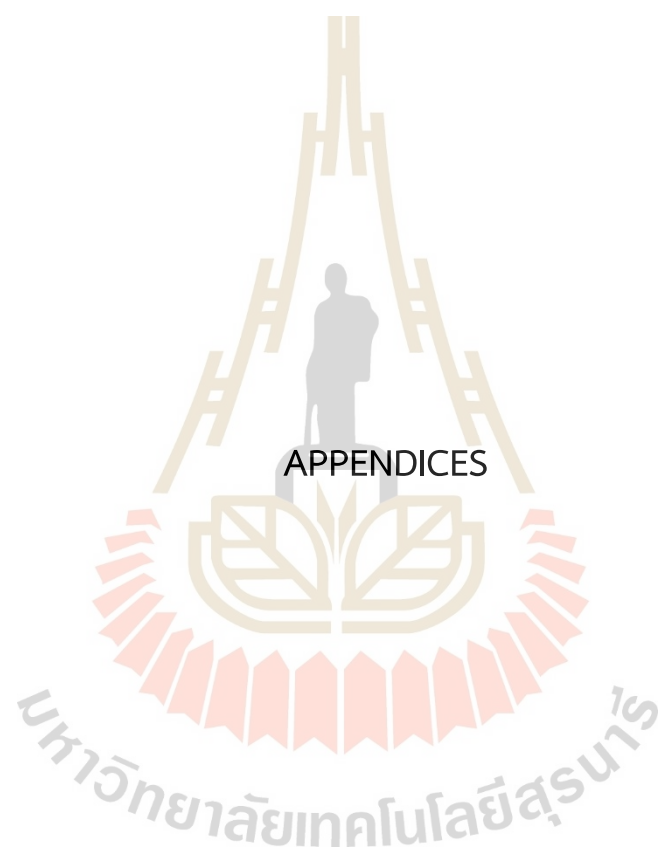
- synthesized using mechanical alloying and spark plasma sintering process. *Journal of Materials Science: Materials in Electronics*. 32(8), 9858–9871.
- Mayer, H., Mikhail, I. and Schubert, K. (1978). Über einige Phasen der Mischungen ZnSbN und CdSbN. *Journal of the Less Common Metals*. 59(1), 43–52.
- Mi, W., Qiu, P., Zhang, T., Lv, Y., Shi, X. and Chen, L. (2014). Thermoelectric transport of Se-rich Ag<sub>2</sub>Se in normal phases and phase transitions. *Applied physics letters*. 104(13).
- Minea, V. (2007) Using geothermal energy and industrial waste heat for power generation : in 2007 IEEE Canada electrical power conference. *IEEE*. 543–549.
- Mirela, V., Narcis, D. and Grozescu, I. (2015). Thermal behavior regarding the thermoelectric Zn<sub>4</sub>Sb<sub>3</sub> obtained by melting and quenching method. *Nonconventional Technologies Review/Revista de Tehnologii Neconventionale*. 19(4).
- Mönkemeyer, K. (1905). Über zink-antimonlegierungen. *Zeitschrift für anorganische Chemie*. 43(1), 182–196.
- Morrison, K. and Dejene, F. K. (2020). Thermal Imaging of the Thomson effect. *Physics*. (13), 137.
- Moustafa, S., Daoush, W., Ibrahim, A. and Neubaur, E. (2011). Hot forging and hot pressing of AlSi powder compared to conventional powder metallurgy route. *Materials Sciences and Applications*. 2(08), 1127.
- Mozharivskiy, Y., Janssen, Y., Haringa, J. L., Kracher, A., Tsokol, A. O. and Miller, G. J. (2006). Zn<sub>13</sub>Sb<sub>10</sub>: a structural and Landau theoretical analysis of its phase transitions. *Chemistry of Materials*. 18(3), 822–831.
- Nylén, J., Andersson, M., Lidin, S. and Häussermann, U. (2004). The structure of  $\alpha$ -Zn<sub>4</sub>Sb<sub>3</sub>: ordering of the phonon-glass thermoelectric material  $\beta$ -Zn<sub>4</sub>Sb<sub>3</sub>. *Journal of the American Chemical Society*. 126(50), 16306–16307.
- Perez-Taborda, J. A., Caballero-Calero, O., Vera-Londono, L., Briones, F. and Martin-Gonzalez, M. (2018). High thermoelectric zT in n-type silver selenide films at room temperature. *Advanced Energy Materials*. 8(8), 1702024.
- Poudeu, P. F., D'Angelo, J., Downey, A. D., Short, J. L., Hogan, T. P. and Kanatzidis, M. G. (2006). High thermoelectric figure of merit and nanostructuring in bulk p-type Na<sub>1-x</sub>PbmSb<sub>y</sub>Te<sub>m</sub><sup>+</sup>. *Angewandte Chemie International Edition*. 45(23), 3835–3839.
- Qiu, A., Zhang, L. and Wu, J. (2010). Crystal structure, electronic structure, and thermoelectric properties of  $\beta$ -Zn<sub>4</sub>Sb<sub>3</sub> from first principles. *Physical Review B*. 81(3), 035203.

- Ravel, B. and Newville, M. (2005). Athena, artemis, hephaestus: data analysis for X-ray absorption spectroscopy using IFEFFIT. *Journal of synchrotron radiation*. 12(4), 537–541.
- Rowe, D. M. (2018). Thermoelectrics handbook: macro to nano. *CRC Press*.
- Rull-Bravo, M., Moure, A., Fernández, J. and Martín-González, M. (2015). Skutterudites as thermoelectric materials: revisited. *RSC Advances*. 5(52), 41653–41667.
- Saini, A., Kumar, R. and Kumar, R. (2021). Introduction and brief history of thermoelectric materials : in thermoelectricity and advanced. *Thermoelectric Materials Elsevier*. 1–19.
- Seebeck, T. J. (1895). Magnetische polarisation der metalle und erze durch temperatur-differenz. *W. Engelmann*.
- Shi, X., Yang, J., Salvador, J. R., Chi, M., Cho, J. Y., Wang, H., Bai, S., Yang, J., Zhang, W. and Chen, L. (2011). Multiple-filled skutterudites: high thermoelectric figure of merit through separately optimizing electrical and thermal transports. *Journal of the American Chemical Society*. 133(20), 7837–7846.
- Shim, H. C., Woo, C.-S. and Han, S. (2015). Thermal cycling behavior of zinc antimonide thin films for high temperature thermoelectric power generation applications. *ACS Applied Materials & Interfaces*. 7(32), 17866–17873.
- Singh, S., Hirata, K., Byeon, D., Matsunaga, T., Muthusamy, O., Ghodke, S., Adachi, M., Yamamoto, Y., Matsunami, M. and Takeuchi, T. (2020). Investigation of thermoelectric properties of  $\text{Ag}_2\text{S}_x\text{Se}_{1-x}$  ( $x = 0.0, 0.2$  and  $0.4$ ). *Journal of Electronic Materials*. 49(5), 2846–2854.
- Snyder, G. J., Christensen, M., Nishibori, E., Caillat, T. and Iversen, B. B. (2004). Disordered zinc in  $\text{Zn}_4\text{Sb}_3$  with phonon-glass and electron-crystal thermoelectric properties. *Nature Materials*. 3(7), 458–463.
- Sodhiya, A., Kumar, R., Singh, A. K. and Soni, S. (2021). Effect of  $\text{Ba}^{2+}$  doping on the structure and transport properties of  $\text{Li}_{6.28}\text{Al}_{0.24}\text{La}_3\text{Zr}_2\text{O}_{12}$  solid electrolyte. *Applied Physics A*. 127(8), 584.
- Spitzer, D. (1970). Lattice thermal conductivity of semiconductors: a chemical bond approach. *Journal of Physics and Chemistry of Solids*. 31(1), 19–40.

- Sui, J., Li, J., He, J., Pei, Y.-L., Berardan, D., Wu, H., Dragoe, N., Cai, W. and Zhao, L.-D. (2013). Texturation boosts the thermoelectric performance of BiCuSeO oxyselenides. *Energy & Environmental Science*. 6(10), 2916–2920.
- Tapiero, M., Tarabichi, S., Gies, J., Noguet, C., Zielinger, J., Joucla, M., Loison, J., Robino, M. and Herion, J. (1985). Preparation and characterization of Zn<sub>4</sub>Sb<sub>3</sub>. *Solar Energy Materials*. 12(4), 257–274.
- Tee, S. Y., Ponsford, D., Lay, C. L., Wang, X., Wang, X., Neo, D. C. J., Wu, T., Thitsartarn, W., Yeo, J. C. C. and Guan, G. (2022). Thermoelectric silver-based chalcogenides. *Advanced Science*. 9(36), 2204624.
- Ueno, K., Yamamoto, A., Noguchi, T., Li, C., Inoue, T., Sodeoka, S. and Obara, H. (2006). Effect of impurity oxygen concentration on the thermoelectric properties of hot-pressed Zn<sub>4</sub>Sb<sub>3</sub>. *Journal of Alloys and Compounds*. 417(1–2), 259–263.
- Ugai, Y. A., Averbakh, E. and Lavrov, V. (1963). Some electrical properties of the intermetallic compound beta-Zn<sub>4</sub>Sb<sub>3</sub>. *Soviet Physics–Solid State*. 4(11), 2393–2395.
- Ur, S.-C., Nash, P. and Kim, I.-H. (2003). Mechanical alloying and thermoelectric properties of Zn<sub>4</sub>Sb<sub>3</sub>. *Journal of materials science*. 38(17), 3553–3558.
- Wang, L., Yan, G., Dong, G., Qiao, S., Fu, G. and Wang, S. (2016). Enhanced light-induced transverse thermoelectric effect in c-axis inclined BiCuSeO thin films via Pb doping. *Optical Materials Express*. 6(8), 2537–2544.
- Zhang, J.-M., Ming, W., Huang, Z., Liu, G.-B., Kou, X., Fan, Y., Wang, K. L. and Yao, Y. (2013). Stability, electronic, and magnetic properties of the magnetically doped topological insulators Bi<sub>2</sub>Se<sub>3</sub>, Bi<sub>2</sub>Te<sub>3</sub>, and Sb<sub>2</sub>Te<sub>3</sub>. *Physical Review B*. 88(23), 235131.
- Zhang, L., Hong, X., Chen, Z., Xiong, D. and Bai, J. (2020). Effects of In<sub>2</sub>O<sub>3</sub> nanoparticles addition on microstructures and thermoelectric properties of Ca<sub>3</sub>Co<sub>4</sub>O<sub>9</sub> compounds. *Ceramics International*. 46(11), 17763–17766.
- Zhang, T., Zhou, K., Li, X., Chen, Z., Su, X. and Tang, X. (2016). Reversible structural transition in spark plasma-sintered thermoelectric Zn<sub>4</sub>Sb<sub>3</sub>. *Journal of materials science*. 51.
- Zlatić, V. and Monnier, R. (2014). Modern theory of thermoelectricity. *OUP Oxford*.

Zou, T., Xie, W., Feng, J., Qin, X. and Weidenkaff, A. (2015). Recent developments in  $\beta$ - $\text{Zn}_4\text{Sb}_3$  based thermoelectric compounds. *Journal of Nanomaterials*.





## APPENDIX A

### PUBLICATION AND PRESENTATION

#### List of presentation

Jampreecha, T., Sawangprom, A., Chanlek, N., Pinitsoontorn, S., Meevasana, W. and Maensiri, S. (2023). Fabrication and Performance of Monolithic  $\beta$ -Zn<sub>4</sub>Sb<sub>3</sub>/ZnO Thermoelectric Generator Module. **Materials Research Meeting/IUMRS-International Conference in Asia (MRM2023/IUMRS-ICA2023)**, Kyoto, Japan.

Jampreecha, T., Sawangprom, A., Chanlek, N., Pinitsoontorn, S., Meevasana, W. and Maensiri, S. (2024). Synthesis and characterizations of  $\beta$ -Zn<sub>4</sub>Sb<sub>3</sub> powders by mechanical alloying method and calcination under Ar atmosphere flowing. **The 22<sup>nd</sup> International Symposium on Eco-materials Processing and Design (ISEPD 2024)**, Nakhon Ratchasima, Thailand.



APPENDIX B  
FIGURE AND TABLE

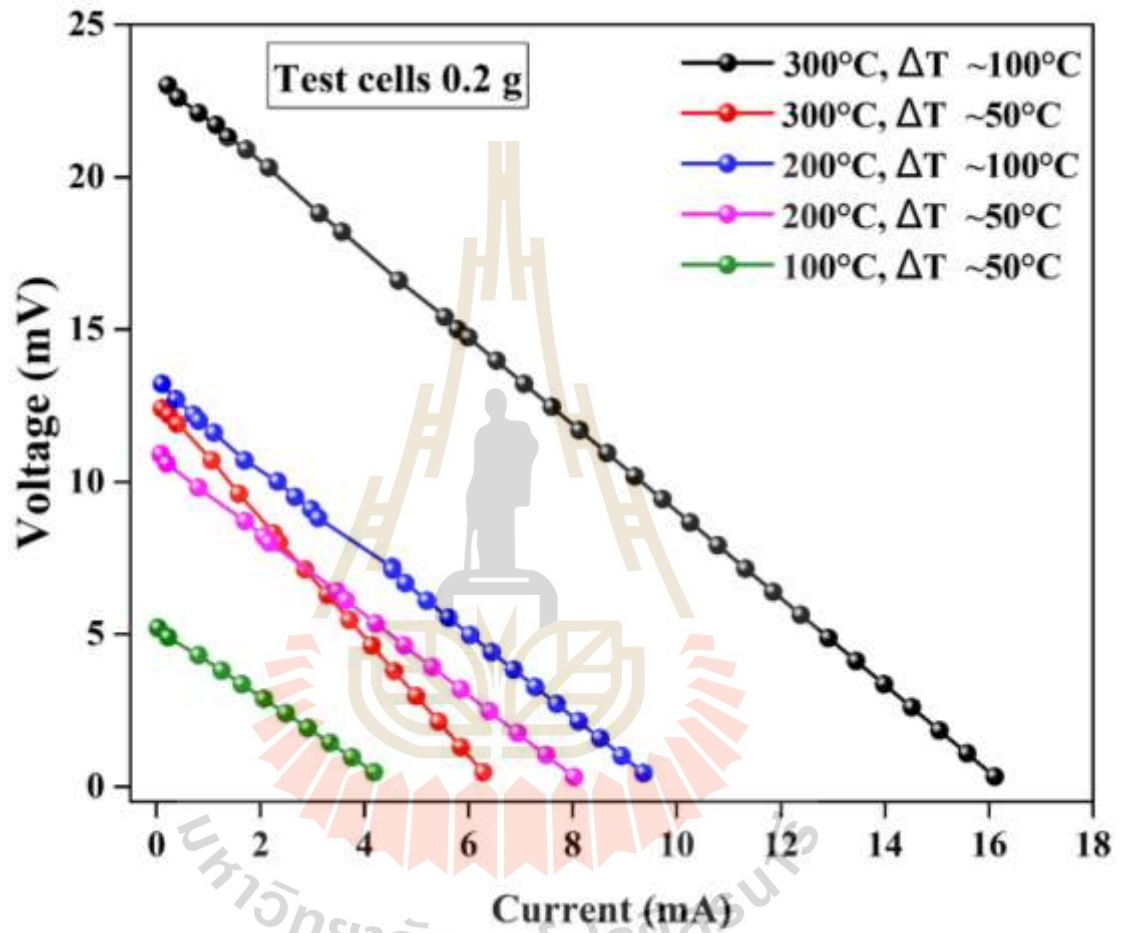


Figure 68 IV-curve of the test cells of monolithic  $\beta\text{-Zn}_4\text{Sb}_3/\text{ZnO}$  TEGs under condition of weight 0.2 g versus different operating  $T_h$  and  $\Delta T$ .

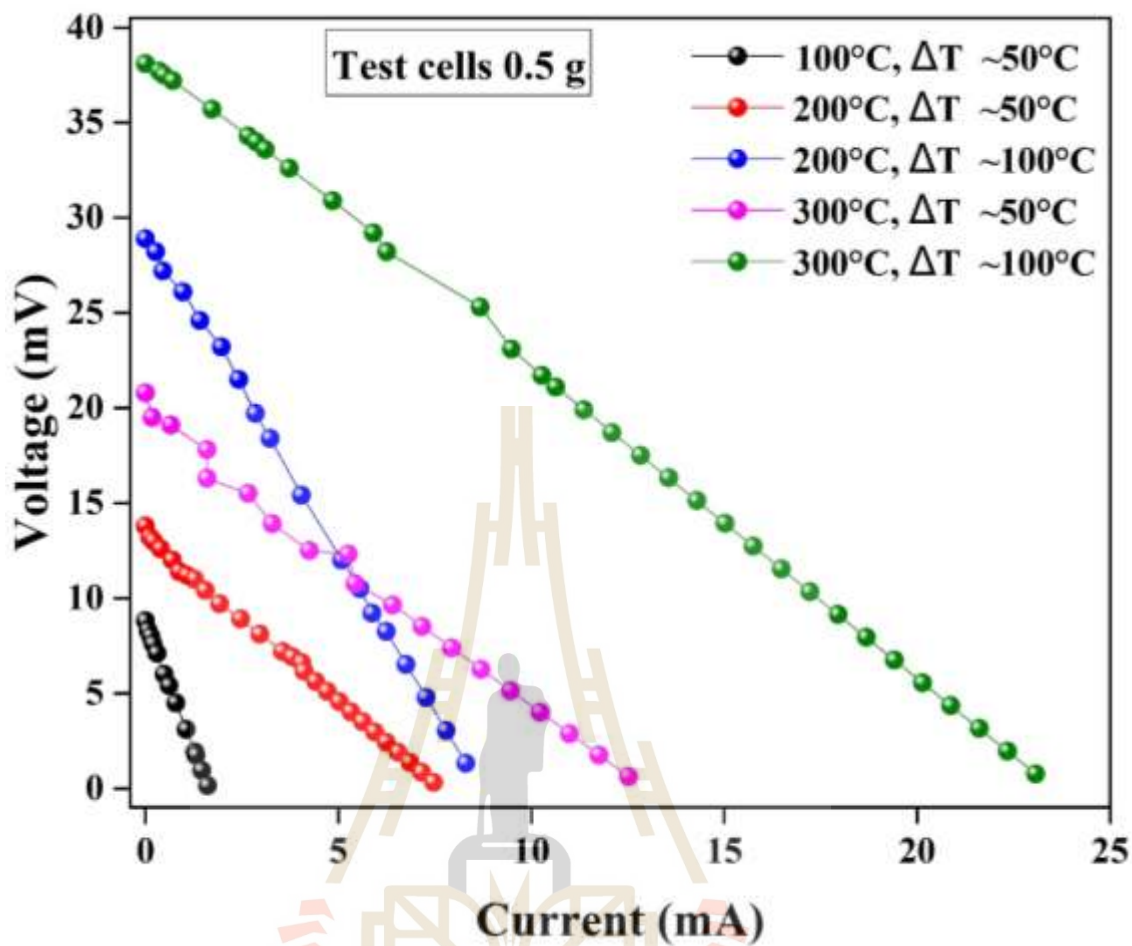


Figure 69 IV-curve of the test cells of monolithic  $\beta\text{-Zn}_4\text{Sb}_3/\text{ZnO}$  TEGs under condition of weight 0.5 g versus different operating  $T_h$  and  $\Delta T$ .

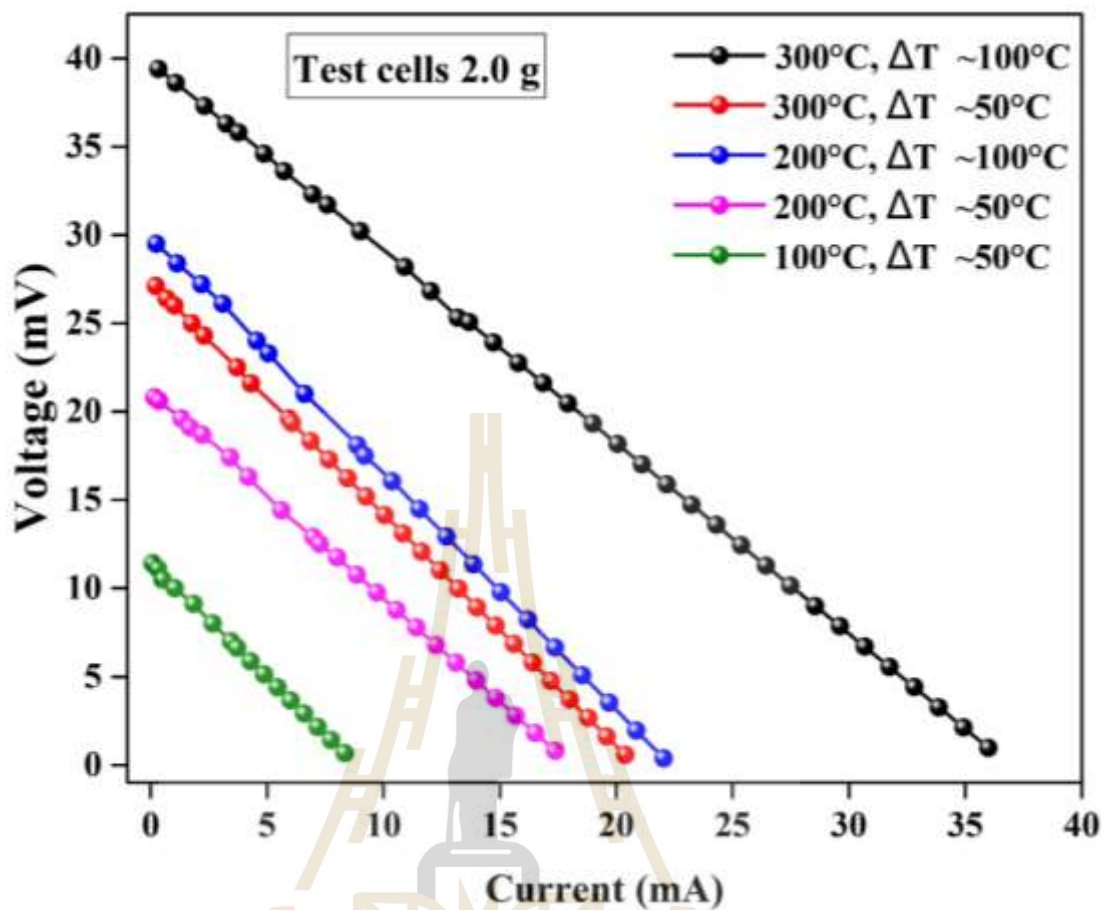


Figure 70 IV-curve of the test cells of monolithic  $\beta\text{-Zn}_4\text{Sb}_3/\text{ZnO}$  TEGs under condition of weight 2.0 g versus different operating  $T_h$  and  $\Delta T$ .

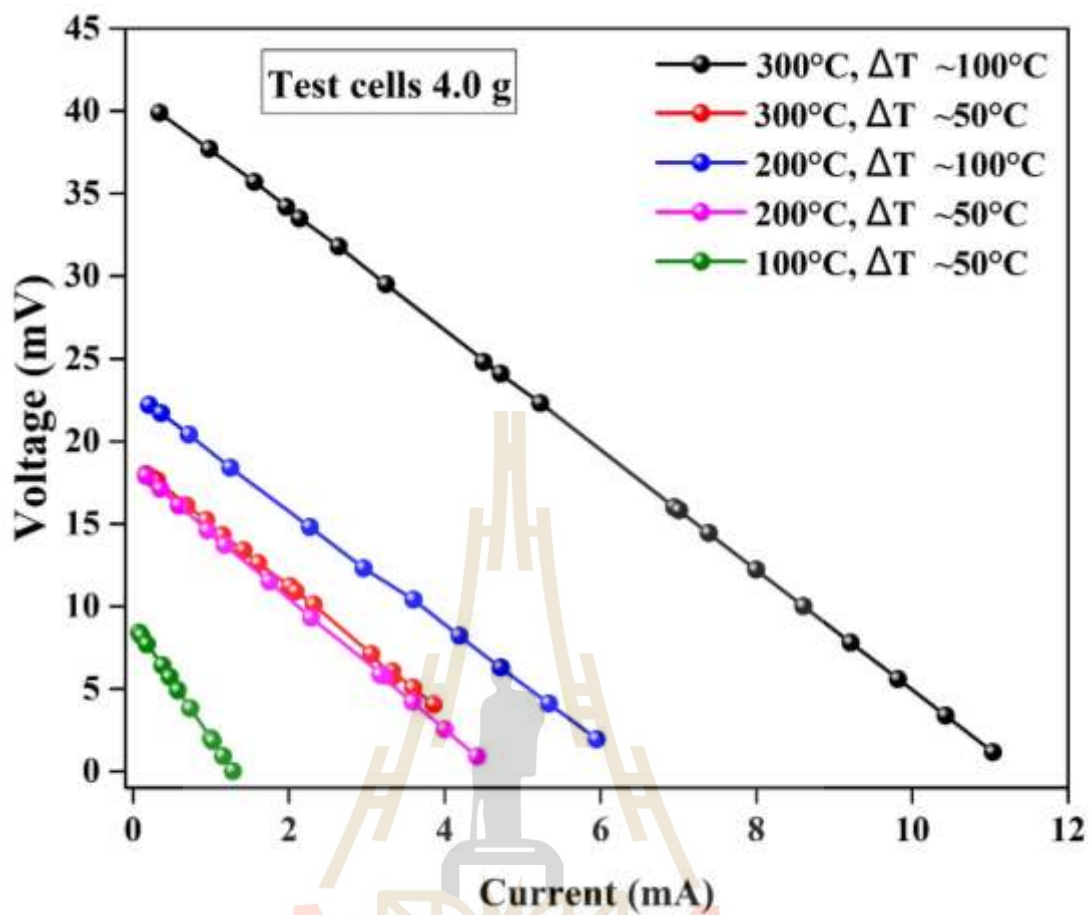


Figure 71 IV-curve of the test cells of monolithic  $\beta\text{-Zn}_4\text{Sb}_3/\text{ZnO}$  TEGs under condition of weight 4.0 g versus different operating  $T_h$  and  $\Delta T$ .

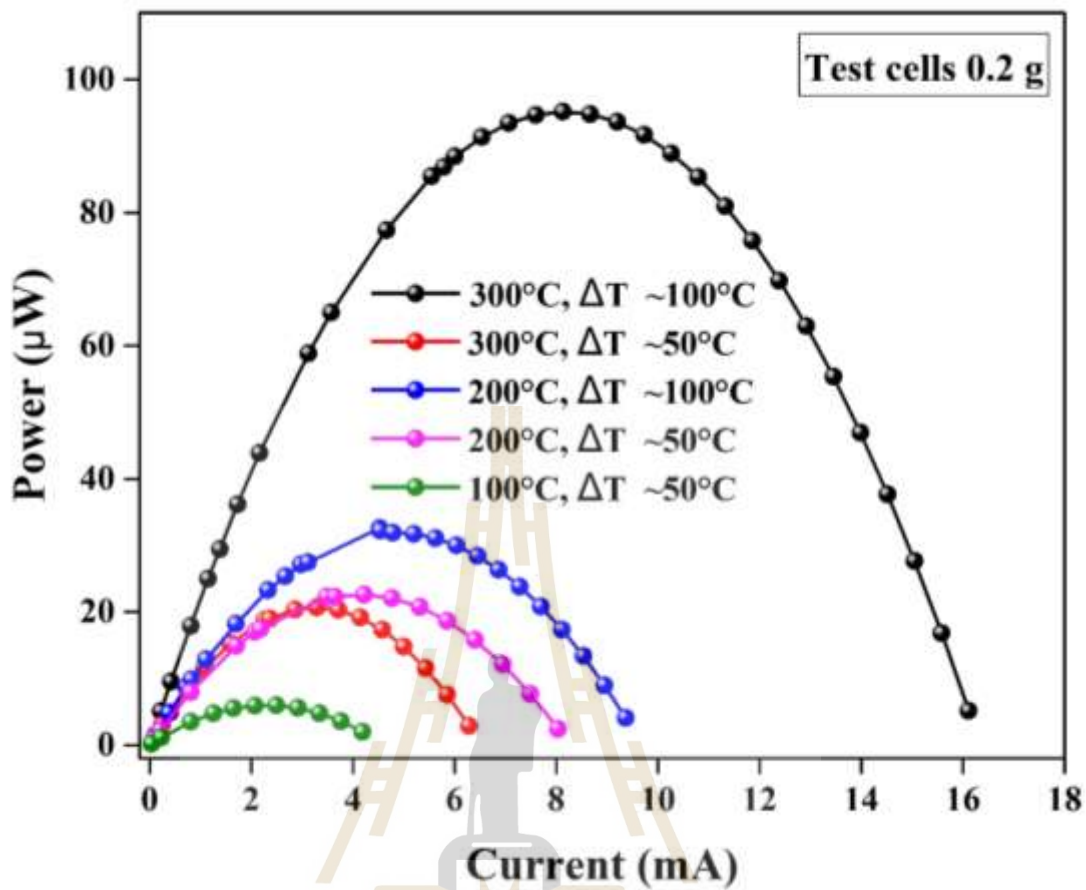


Figure 72 Electrical power output curves of the test cells of monolithic  $\beta\text{-Zn}_4\text{Sb}_3/\text{ZnO}$  TEG module under condition of weight 0.2 g versus different operating  $T_h$  and  $\Delta T$ .

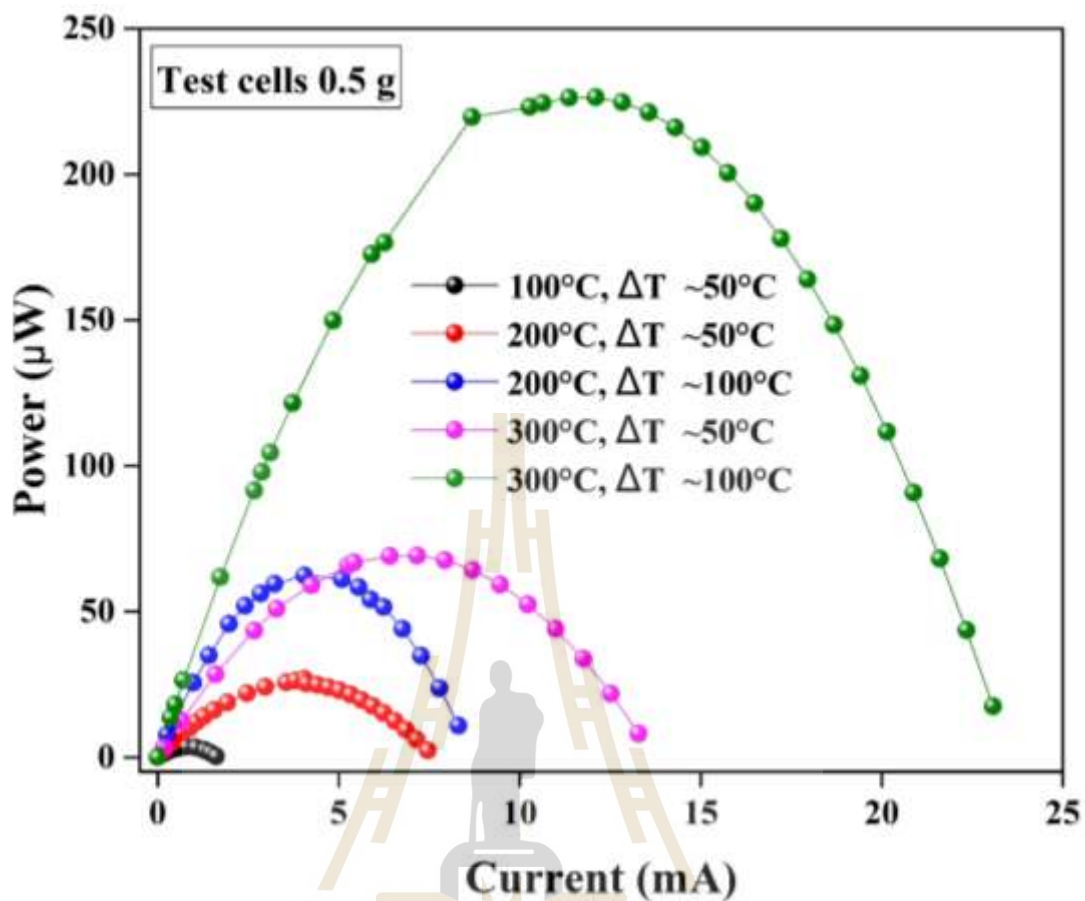


Figure 73 Electrical power output curves of the test cells of monolithic  $\beta\text{-Zn}_4\text{Sb}_3/\text{ZnO}$  TEG module under condition of weight 0.5 g versus different operating  $T_h$  and  $\Delta T$ .

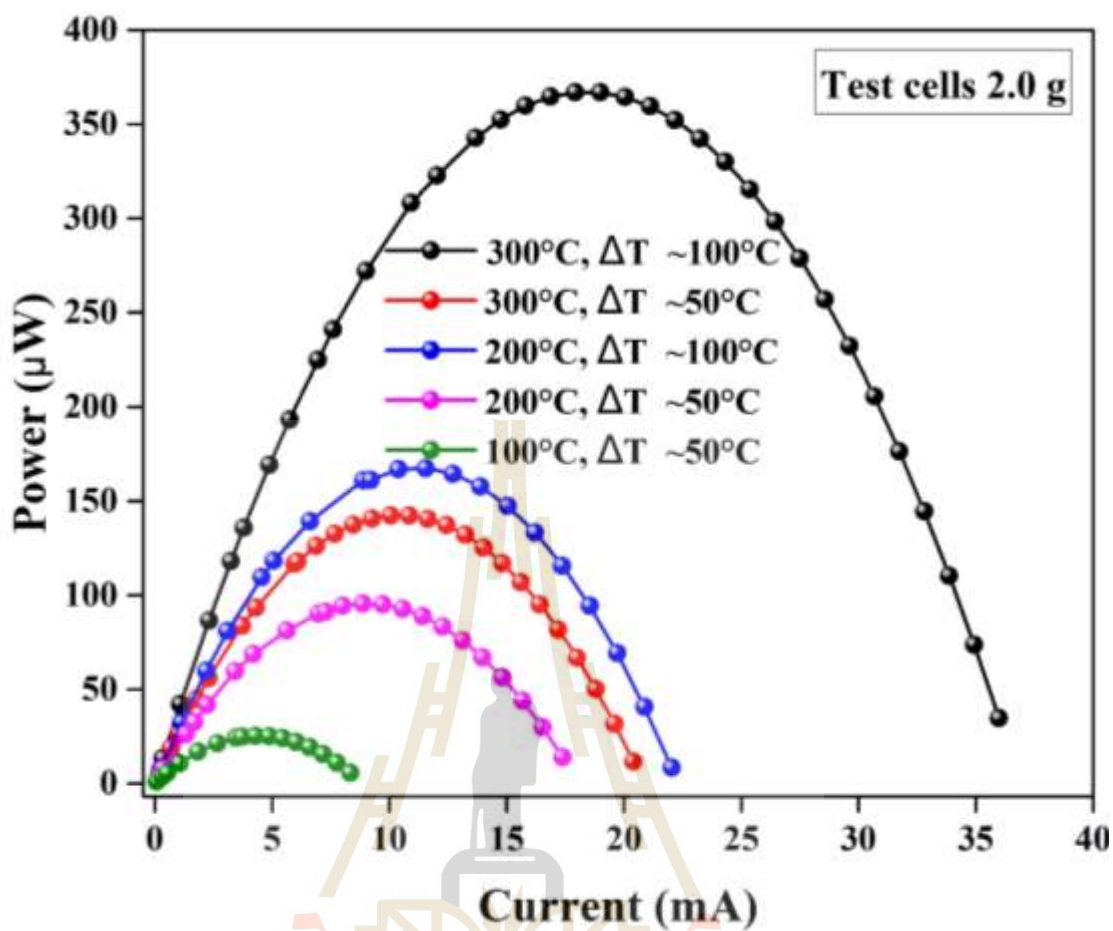


Figure 74 Electrical power output curves of the test cells of monolithic  $\beta\text{-Zn}_4\text{Sb}_3/\text{ZnO}$  TEG module under condition of weight 2.0 g versus different operating  $T_h$  and  $\Delta T$ .

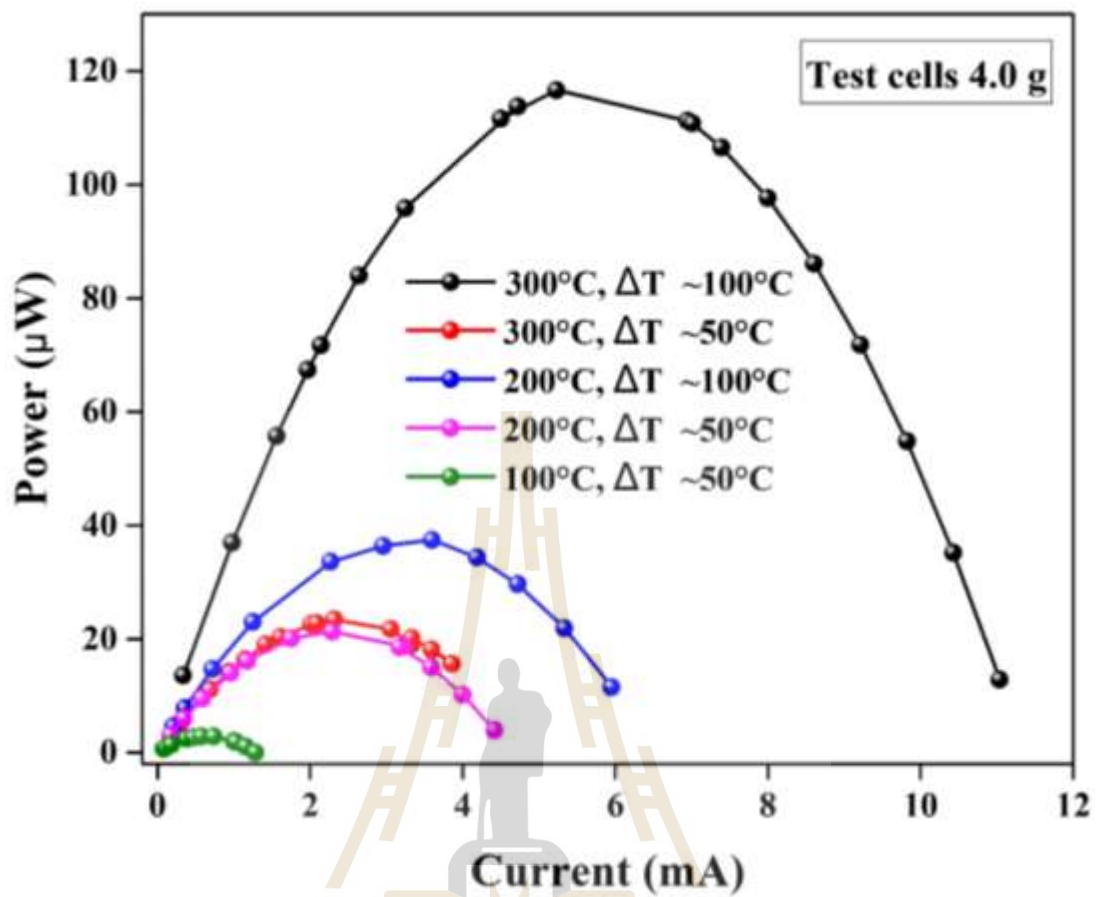


Figure 75 Electrical power output curves of the test cells of monolithic  $\beta\text{-Zn}_4\text{Sb}_3/\text{ZnO}$  TEG module under condition of weight 4.0 g versus different operating  $T_h$  and  $\Delta T$ .

**Table 11** Comparison of maximum electrical power output of test cell of monolithic  $\beta$ -Zn<sub>4</sub>Sb<sub>3</sub>/ZnO TEG module under condition of weight 0.2 g for different conditions of  $T_h$  and  $\Delta T$ .

Hot-side Temperature	Gradient temperature ( $\Delta T$ )	Maximum $P_{out}$
100 °C	50 °C	6 $\mu W$
200 °C	50 °C	22 $\mu W$
200 °C	100 °C	31 $\mu W$
300 °C	50 °C	20 $\mu W$
300 °C	100 °C	95 $\mu W$

**Table 12** Comparison of maximum electrical power output of test cell of monolithic  $\beta$ -Zn<sub>4</sub>Sb<sub>3</sub>/ZnO TEG module under condition of weight 0.5 g for different conditions of  $T_h$  and  $\Delta T$ .

Hot-side Temperature	Gradient temperature ( $\Delta T$ )	Maximum $P_{out}$
100 °C	50 °C	5 $\mu W$
200 °C	50 °C	28 $\mu W$
200 °C	100 °C	63 $\mu W$
300 °C	50 °C	69 $\mu W$
300 °C	100 °C	227 $\mu W$

**Table 13** Comparison of maximum electrical power output of test cell of monolithic  $\beta$ -Zn<sub>4</sub>Sb<sub>3</sub>/ZnO TEG module under condition of weight 2.0 g for different conditions of  $T_h$  and  $\Delta T$ .

Hot-side Temperature	Gradient temperature ( $\Delta T$ )	Maximum $P_{out}$
100 °C	50 °C	25 $\mu$ W
200 °C	50 °C	97 $\mu$ W
200 °C	100 °C	166 $\mu$ W
300 °C	50 °C	142 $\mu$ W
300 °C	100 °C	366 $\mu$ W

**Table 14** Comparison of maximum electrical power output of test cell of monolithic  $\beta$ -Zn<sub>4</sub>Sb<sub>3</sub>/ZnO TEG module under condition of weight 4.0 g for different conditions of  $T_h$  and  $\Delta T$ .

Hot-side Temperature	Gradient temperature ( $\Delta T$ )	Maximum $P_{out}$
100 °C	50 °C	3 $\mu$ W
200 °C	50 °C	21 $\mu$ W
200 °C	100 °C	37 $\mu$ W
300 °C	50 °C	23 $\mu$ W
300 °C	100 °C	115 $\mu$ W

## CURRICULUM VITAE

**Name** Mr. Tachgiss Jampreecha  
**Date of Birth** July 27, 1992  
**Place of Birth** Alunaumarin road, Siri Rat, Bangkok Noi,  
Bangkok, 10700, Thailand

### Education

2011–2014 Khon Kaen University, Khon Kaen, Thailand. B.Sc. In Physics  
2015–2018 Suranaree University of Technology, Nakhon Ratchasima, Thailand.  
M.Sc. In Applied Physics  
2019–2024 Suranaree University of Technology, Nakhon Ratchasima, Thailand.  
Ph.D. In Physics

